

# Lawrence Berkeley National Laboratory

## Recent Work

### Title

PICOSECOND SPECTROSCOPY OF CHEMICAL REACTIONS IN LIQUIDS

### Permalink

<https://escholarship.org/uc/item/8zw4813t>

### Author

Harris, A.L.

### Publication Date

1985-08-01

c.2



# Lawrence Berkeley Laboratory

UNIVERSITY OF CALIFORNIA

RECEIVED  
LAWRENCE  
BERKELEY LABORATORY

OCT 9 1985

LIBRARY AND  
DOCUMENTS SECTION

## Materials & Molecular Research Division

PICOSECOND SPECTROSCOPY OF CHEMICAL REACTIONS  
IN LIQUIDS

A.L. Harris  
(Ph.D. Thesis)

August 1985

**TWO-WEEK LOAN COPY**

*This is a Library Circulating Copy  
which may be borrowed for two weeks.*



Prepared for the U.S. Department of Energy under Contract DE-AC03-76SF00098

LBL-20195

c.2

## **DISCLAIMER**

This document was prepared as an account of work sponsored by the United States Government. While this document is believed to contain correct information, neither the United States Government nor any agency thereof, nor the Regents of the University of California, nor any of their employees, makes any warranty, express or implied, or assumes any legal responsibility for the accuracy, completeness, or usefulness of any information, apparatus, product, or process disclosed, or represents that its use would not infringe privately owned rights. Reference herein to any specific commercial product, process, or service by its trade name, trademark, manufacturer, or otherwise, does not necessarily constitute or imply its endorsement, recommendation, or favoring by the United States Government or any agency thereof, or the Regents of the University of California. The views and opinions of authors expressed herein do not necessarily state or reflect those of the United States Government or any agency thereof or the Regents of the University of California.

LBL-20195

PICOSECOND SPECTROSCOPY OF CHEMICAL REACTIONS  
IN LIQUIDS

Alexander Lowe Harris  
Ph.D. Thesis

Lawrence Berkeley Laboratory  
University of California  
Berkeley, California 94720

August 1985

# Picosecond Spectroscopy of Chemical Reactions in Liquids

By

Alexander Lowe Harris

## Abstract

To develop a detailed picture of a model bimolecular liquid reaction, picosecond transient absorption measurements from 1000-295 nm were used to monitor the dynamics of the geminate iodine recombination reaction in a variety of inert solvents. Most of the atoms which undergo geminate recombination do so in  $\leq 15$  ps, in agreement with the predictions of existing molecular dynamics simulations. The subsequent vibrational and electronic energy relaxation of the recombined molecule is relatively slow and accounts for most of the transient absorption dynamics. The relaxing X-state vibrational population distribution is extracted using calculated spectra of the excited vibrational levels. Vibrational relaxation times are  $\sim 15$  ps to the middle of the ground state well and  $\sim 150$  ps to  $v=0$ . Energy transfer to solvent translational and rotational degrees of freedom appears to be more important than near-resonant transfer to solvent vibrational modes. B-state predissociation times of 10-15 ps and A'-state lifetimes of 65-2700 ps are found in various solvents. Available models do not account for the solvent dependence of the A'-state lifetime.

To extend the wavelength range usable in transient spectroscopy, tunable short light pulses in the vibrational infrared were generated by frequency-shifting tunable visible pulses using stimulated electronic Raman scattering on the cesium 6s-5d Raman transition. Narrow-band

nanosecond pulses of up to 120  $\mu\text{J}$  were generated from 3450 to 900  $\text{cm}^{-1}$  (2.9 to 11.1  $\mu\text{m}$ ), and broadband nanosecond pulses up to 75  $\mu\text{J}$  were generated from 3390 to 1800  $\text{cm}^{-1}$  (2.9 to 5.5  $\mu\text{m}$ ). Picosecond infrared pulses of up to 11  $\mu\text{J}$  were generated from 3040-1950  $\text{cm}^{-1}$  (3.3-5.1  $\mu\text{m}$ ).

The theory, design and performance of the amplified picosecond dye laser used in the investigations are described. The laser system produces bandwidth-limited 1-ps pulses at a repetition rate of 10 pps with energies of 1-2 mJ tunable from 565-610 nm. Short and long term energy stability of  $\pm 10\%$  is obtained in a beam with a near-Gaussian spatial profile.

Charles B. Harris  
3 September, 1985

TABLE OF CONTENTS

1. <u>Introduction</u> .....	1
References.....	7
2. <u>Picosecond Dynamics of the Iodine Photodissociation and Recombination Reaction and Comparison to Theories for Chemical Reactions in Solution</u> .....	8
I. Introduction.....	8
II. Experimental.....	15
III. Results.....	22
A. Long Time Decays: A'-state Trapping.....	23
B. Intermediate Time Absorptions: X-State Vibrational Dynamics.....	48
C. Early Time Absorptions: B-State Predissociation Dynamics.....	53
D. Separation of Absorption Components.....	55
E. Summary of the Reaction Model.....	64
IV. Comparison to Previous Results.....	66
V. Comparison with Theoretical Models.....	69
A. Recombination Dynamics.....	70
B. Vibrational Relaxation: Classical Analysis and Relaxation Mechanism....	73
C. Vibrational Relaxation: Quantum Spectral Analysis.....	81
D. Lifetime of the A' State.....	92
E. Predissociation.....	98
VI. Summary and Conclusions.....	99
Appendices.....	101
References.....	106

4.	<u>Generation of Tunable Short Pulses in the Vibrational Infrared by Stimulated Electronic Raman Scattering from the Cesium 6s-5d Transition</u> .....	111
	I. Introduction.....	111
	II. Stimulated Electronic Raman Scattering in Cesium.....	114
	A. Stimulated Electronic Raman Scattering.....	114
	B. Cesium 6s-5d Raman Transition.....	115
	C. Reduction of the Cesium Dimer Density.....	121
	III. Generation of Widely Tunable Nanosecond Infrared Pulses.....	133
	A. Narrowband Infrared Generation.....	133
	B. Broadband Infrared Nanosecond Pulses.....	139
	C. Summary.....	140
	IV. Generation of Tunable Picosecond Infrared Pulses.....	145
	V. Summary.....	152
	References.....	153
4.	<u>Theory and Performance of a High Gain Picosecond Dye-Laser Amplifier</u> .....	156
	I. Introduction.....	156
	II. Theory of a High Gain Picosecond Amplifier.....	160
	A. High Gain Amplifier - Multiple Stages.....	160
	B. First Amplifier Stage - High Gain.....	161
	C. Second Amplifier Stage - Energy Stability.....	169
	D. Final Amplifier Stage - Energy Storage.....	169
	E. Optical Isolation of Amplifier Stages.....	178
	F. Summary of Amplifier Theory.....	179
	III. Picosecond Dye Amplifier Performance.....	180
	A. Output Energy and Tuning Curves.....	180
	B. Pulse Width and Spectrum.....	186

IV. Conclusion.....	190
Appendix.....	191
References.....	193
ACKNOWLEDGEMENTS.....	194
THESIS APPENDIX.....	196

## Chapter 1. Introduction

Direct, picosecond observations of the dynamics of simple model reactions provide a promising tool for developing a more quantitative picture of the role of the solvent in determining reaction rates and pathways in liquid phase chemistry. Substantial progress has been made when such studies can isolate elementary reaction processes for comparison with reaction models. For instance, the predictions of the classical Kramer's theory of one-dimensional reactive barrier crossing<sup>1</sup> have been quantitatively tested and generalized in a recent series of picosecond studies of photo-induced unimolecular isomerizations.<sup>2-4</sup> In many cases, however, the complexity of the resulting transient spectroscopy obtained at available visible and UV wavelengths has hindered attempts to make quantitative comparisons with theoretical models.

The goal of the work presented in this thesis is to provide clearly defined experimental tests of the predictions of models for liquid phase reaction dynamics on short time scales. First, work described in Chapter 2 monitored the dynamics of a simple model bimolecular liquid reaction in sufficient detail to develop a quantitative picture of an entire reaction sequence, using high time resolution transient spectroscopy. The measurements allow careful comparisons to be made with theoretical models of short-time reactive particle motions and molecular energy transfer in a liquid reaction. Second, Chapter 3 describes the development of new sources of tunable short light pulses in the vibrational infrared spectral region. Transient infrared spectroscopy promises to provide previously unavailable structural

information on transient molecular species and on the dynamics of molecular bond transformations during chemical reactions. The developments reported here make progress in overcoming the lack of useful short pulse sources in this spectral region. Both of these research efforts have depended upon a stable source of tunable high power visible laser light pulses which is described in Chapter 4.

#### A. Dynamics of a Simple Two Atom Reaction

The experiments described in Chapter 2 examine the dynamics of photodissociation of the iodine molecule and the subsequent recombination of the reactive iodine atoms.<sup>5-7</sup> The recombination of an atom with its original partner, termed geminate recombination, is a simple model of a diffusion-controlled barrierless bimolecular reaction. The initial recombination rate is determined by short time, short distance motion of separately diffusing reactive atoms. Subsequent energy relaxation of the recombined molecule presents a simple system for the study of vibrational energy transfer from a highly energetic molecule to its surrounding solvent, and for the study of solvent-induced electronic curve crossing dynamics. In addition, because of the structural simplicity of the reaction and the detailed spectroscopy available for the iodine molecule, the accessible potential energy surfaces upon which reaction can occur are known. For these reasons, the reaction has been widely examined both experimentally and theoretically. Despite much study, however, the time scales of even the most basic steps in the geminate atom recombination reaction have remained in controversy.

The transient picosecond spectroscopic measurements described in Chapter 2 substantially improve the experimental basis for the assignment of the iodine recombination reaction dynamics. This assignment is then used to examine assumptions and theories which have been applied to the atom recombination reaction in simple solvents. The results demonstrate clearly that the geminate recombination process is very rapid ( $<15$  ps) in a number of simple solvents. This contrasts with a time of  $\sim 100$  ps for diffusion across distances as small as  $5\text{\AA}$ ,<sup>8</sup> and suggests that a substantial fraction of the atoms are trapped, or "caged" before they separate by as much as one molecular diameter. The results indicate that the details of molecular interactions at short times must be included in an accurate description of atom recombination, and that popular macroscopic diffusion models are not appropriate.

The experimental data also demonstrate that, following recombination, the energy relaxation of the recombined molecule is slow, and accounts for most of the observed transient absorption dynamics. The vibrational energy relaxation dynamics on the ground potential surface are quantitatively derived from the data using realistic calculated spectra of excited vibrational levels. The derived dynamics provide a rare measurement of vibrational energy transfer in a liquid over a wide molecular energy range. The results demonstrate that the role of near-resonant energy transfer from the iodine molecule to solvent vibrational modes is probably less important than hypothesized in several models. It is suggested that vibration-to-translation and vibration-to-rotation energy transfer may play an important role in deactivating molecules with vibrational frequencies as low as that of the iodine molecule. The electronic relaxation of the iodine molecule

shows a dramatic solvent dependence which cannot yet be accounted for and which provides challenges for additional theoretical work.

The detailed, quantitative picture of the geminate iodine recombination reaction thus provides an excellent test system for theoretical models of several fundamental reaction steps, including short-time particle motions in liquids, vibrational energy coupling between a reactive solute and its solvent, and solvent-induced electronic curve crossing processes. The work also lays a foundation for further studies of simple photo-induced reactions in structureless solvents such as rare gas fluids, and in reactions of more complicated polyatomic molecules.

#### B. Generation of Short Infrared Light Pulses

The examination of fast transient behavior in chemical reactions has relied almost exclusively upon visible and near-UV probes of reaction dynamics. This has limited studies to molecules with appropriate absorptions, and has limited the available structural information which would be most useful in examining the rearrangement, breaking, or formation of chemical bonds as a reaction proceeds. Chapter 3 reports the development of new sources of short, tunable infrared light pulses in efforts to extend the range of wavelengths which can be used to examine solution reactions and other fast condensed phase dynamics.

Because of the lack of tunable pulsed laser sources in the vibrational infrared region, the generation of light pulses in this region has been based upon frequency-shifting tunable visible laser

pulses. The work described in Chapter 3 examined a simple, single step frequency shift by stimulated electronic Raman scattering in cesium vapor.<sup>9-11</sup> Very widely tunable narrowband and broadband nanosecond pulses were generated across much of the vibrational infrared by shifting light pulses from a reliable rhodamine dye laser. Picosecond pulses were also generated across a narrower tuning range, and the nature of losses which will have to be eliminated to extend the picosecond tuning range were examined. The stimulated electronic Raman scattering technique provides a promising approach for the development of practical transient infrared spectroscopy.

#### C. High Power Picosecond Dye Laser

Chapter 4 describes the theory, design and performance of the amplified, synchronously-pumped picosecond dye laser which provided the high power, tunable picosecond pulses used in the above studies. The design was optimized to provide high energy pulses with good pulse-to-pulse and long term stability. The beam quality of the laser output, upon which the reproducibility of sensitive experiments depended, was optimized by careful use of a high quality pump laser beam to pump the amplifier system. The design has proven to be a practical source of short visible light pulses for a range of studies of fast dynamics in condensed phase systems.

Much of the work presented in this thesis has been published in collaboration with others, including Mark Berg, J. Keenan Brown, and Charles B. Harris.<sup>5-7,9-11</sup> In addition, there is overlap in the subjects covered by this thesis and the Ph.D. thesis prepared by Mark

Berg,<sup>12</sup> particularly in the discussions of iodine reaction dynamics. An effort has been made to include here aspects of calculations or design which are important in reproducing the quoted results, but which do not appear elsewhere. Cases where more detailed measurements are available in Mark Berg's thesis are noted in the text.

## REFERENCES

1. H. A. Kramers, *Physica* 7, 284 (1940).
2. S. P. Velsko, D. H. Waldeck, and G. R. Fleming, *J. Chem. Phys.* 78, 249 (1983).
3. S. H. Courtney and G. R. Fleming, *Chem. Phys. Lett.* 103, 443 (1983).
4. S. H. Courtney, G. R. Fleming, L. R. Khundkar, and A. H. Zewail, *J. Chem. Phys.* 80, 4559 (1984).
5. M. Berg, A. L. Harris, and C. B. Harris, in Ultrafast Phenomena IV, edited by D. H. Auston and K. B. Eisenthal, *Springer Series in Chemical Physics*, Vol. 38 (Springer-Verlag, New York, 1984), p. 300.
6. M. Berg, A. L. Harris, and C. B. Harris, *Phys. Rev. Lett.* 54, 951 (1985).
7. A. L. Harris, M. Berg, and C. B. Harris, *J. Chem. Phys.* (to be published, 1985).
8. see, e. g., D. J. Nesbitt and J. T. Hynes, *J. Chem. Phys.* 77, 2130 (1982).
9. A. L. Harris, J. K. Brown, M. Berg, and C. B. Harris, *Opt. Lett.* 9, 47 (1984).
10. M. Berg, A. L. Harris, J. K. Brown, and C. B. Harris, *Opt. Lett.* 9, 50 (1984).
11. M. Berg, A. L. Harris, J. K. Brown, and C. B. Harris, in Ultrafast Phenomena IV, edited by D. H. Auston and K. B. Eisenthal, *Springer Series in Chemical Physics*, Vol. 38 (Springer-Verlag, New York, 1984), p.52.
12. M. Berg, Ph.D. Thesis, The University of California at Berkeley, Berkeley, Ca., 1985.

Chapter 2. Picosecond Dynamics of the Iodine Photodissociation and Recombination Reaction and Comparison to Theories for Chemical Reactions in Solution.

I. INTRODUCTION

The iodine photodissociation/recombination reaction has served as a primary model system for the study of liquid-phase chemical reactions, both because of its theoretical simplicity and its experimental accessibility. Particular interest has focused on the role of the solvent in determining the speed and efficiency with which the two dissociated atoms recombine with their original partner to form a stable molecule. This process has been termed geminate recombination to distinguish it from slower diffusional recombination of those atoms which escape their original partner. The geminate recombination process and the subsequent energy relaxation of the recombined molecule form a simple model of bimolecular reaction in liquids, and can be used to test the accuracy of liquid reaction theory at short times and short distances.

Despite a long history of study,<sup>1</sup> disagreement about the timescales and importance of the most basic steps in this reaction has arisen due to conflicts in interpretation<sup>2,3</sup> and in experimental results.<sup>4-10</sup> Recently, Harris, Berg, Harris and Brown<sup>11-13</sup> have presented picosecond absorption data on iodine photodissociation which showed that geminate recombination occurs an order of magnitude faster than proposed by some<sup>2,4</sup> and clarified the roles of solvent-induced vibrational

relaxation, predissociation and electronic relaxation. This chapter describes the picosecond absorption experiments, and analyzes the dynamics of recombination and energy relaxation in a series of alkane and chlorinated methane solvents. The abundant spectroscopic information available on the iodine molecule provides a firm basis upon which to assign the various reaction steps. Several theoretical approaches to understanding the microscopic motions of reactive atoms and the energy relaxation of the recombined molecule are evaluated through comparisons with the experimentally derived dynamics.

The first extensive studies of the iodine photodissociation reaction were carried out by Noyes and coworkers, who studied the quantum yield of unrecombined atoms with a scavenger technique and interpreted the results with simple diffusion models.<sup>14-19</sup> More recently, laser techniques have been used to study both the yield of unrecombined atoms and the rate of non-geminate recombination over a wide range of densities.<sup>20-23</sup> These studies do not, however, provide direct information about the dynamics of geminate recombination.

The first time-resolved measurements of geminate iodine recombination were made by Chuang, Hoffman and Eisenthal.<sup>2</sup> The iodine was primarily excited to the bound B state (Fig. 1) by a pulse of 532 nm light, and the subsequent reaction was monitored by measuring the absorption at the same wavelength. The B state was found to undergo rapid ( $\leq 20$  ps) solvent-induced predissociation. The predissociation may occur to any of several dissociative states, but it has recently been argued that the  $a(1_g)$  state is probably responsible for most collision-induced predissociation (Fig. 1).<sup>24</sup> Following predissociation, the molecular absorption was found to partially return in 140 ps in  $\text{CCl}_4$  and

70 ps in hexadecane.<sup>25</sup> These absorption recoveries were interpreted as a direct measurement of the recombination of iodine atoms with their original partner. Similar measurements in a series of n-alkane solutions<sup>26,27</sup> and in liquid xenon<sup>28</sup> have been interpreted in the same way.

Nesbitt and Hynes subsequently suggested that the recovery of the green absorption might be due to slow vibrational relaxation rather than to geminate recombination.<sup>3</sup> They pointed out that the Franck-Condon factors for absorption at 532 nm from the iodine molecule's X state are strong only for the lowest vibrational levels. If vibrational relaxation of the recombined iodine molecule were slow, the absorption recovery at 532 nm would also be slow, even if the recombination process itself were fast. Calculations by Nesbitt and Hynes and others have shown that relaxation times of 100 ps to 1 ns are plausible.<sup>3,29-31</sup> Molecular dynamics simulations have explicitly predicted that absorption should first appear in the near infrared, when the molecule is highly vibrationally excited, and that it should shift smoothly to shorter wavelengths as the molecule vibrationally relaxes (Fig. 1).<sup>9,10,31</sup>

Two nearly simultaneous experimental efforts to confirm the predicted red absorptions have obtained conflicting results. Bado et al. observed transient absorptions from 595-840 nm in alkane and haloalkane solvents which shifted to shorter wavelengths in an ~100 ps period.<sup>7-10</sup> They concluded that the absorptions were due to vibrationally relaxing molecules and that geminate recombination is faster than vibrational relaxation. Kelley et al. also observed transient absorptions from 590 to 750 nm in alkane and chloroalkane solvents, but found no spectral shift with time.<sup>4,5</sup> They assigned the

red absorption to recombined molecules trapped in the A or A' states (Fig. 1). Based on the lack of a spectral shift, they concluded that vibrational relaxation is fast and that geminate recombination requires ~100 ps as originally proposed.

The present data taken in a number of inert solvents extend from 295 nm to 1000 nm with higher time resolution and signal-to-noise ratio than previously available. These data resolve two components in the red absorption, one of which will be assigned to vibrationally relaxing X-state molecules and one to molecules trapped in the A' state. Newly observed absorptions in the UV provide direct information on the vibrational relaxation and predissociation rate of the initially populated B state. Although the absorption decays in different classes of solvent initially appear quite different, it will be shown that they can all be explained in terms of a single model.

This model for the origin of various absorption components clarifies the physics of the various reaction steps and for the first time provides a firm experimental basis for a theoretical understanding of the reaction dynamics. First, the reaction model implies that geminate recombination is predominantly completed in <15 ps in all of these solvents, and that slow vibrational and electronic energy relaxation account for the subsequent slow (100 ps - 3 ns) transient recovery. Molecular dynamics simulations are shown to be consistent with the existence of a rapid recombination process, while hydrodynamic models have little predictive value. Secondly, the evolution of the vibrationally relaxing X-state population is extracted from the absorption data with the use of calculated spectra from vibrationally excited molecules. The suggested role of vibration-to-vibration energy

transfer to the solvent is not supported by the data in chlorinated methane solvents, although this mechanism may play a role in the alkane solvents. Finally, solvent variations in the iodine molecule's electronic-state lifetimes are not accounted for by present theories.

The later sections of this chapter summarize the reaction model and make quantitative comparisons with theories designed to account for the dynamics of the individual reactions steps. Those sections are intended to be self-contained so that readers less interested in experimental and spectroscopic details may read further beginning at section III E. The organization of the chapter is as follows: Section II discusses the experimental methods, and Section III assigns the components of the absorption data. Section IV compares the present results with the sometimes contradictory earlier work. Finally, section V examines the ability of available reaction models to account for the dynamics of the reaction steps as observed in this work. Because of the extensive use of figures in this chapter, they have been grouped at the ends of sections or of subsections in order to facilitate their use.

FIG. 1. Electronic potential surfaces of  $I_2$  important to the discussion. Five states which correlate with ground state atoms as well as numerous higher states are not shown (Ref. 44). The B state vibrational level initially populated by 590 nm light is labeled. Vertical transitions illustrate the shift in absorption wavelength with vibrational level in both the X and B states.

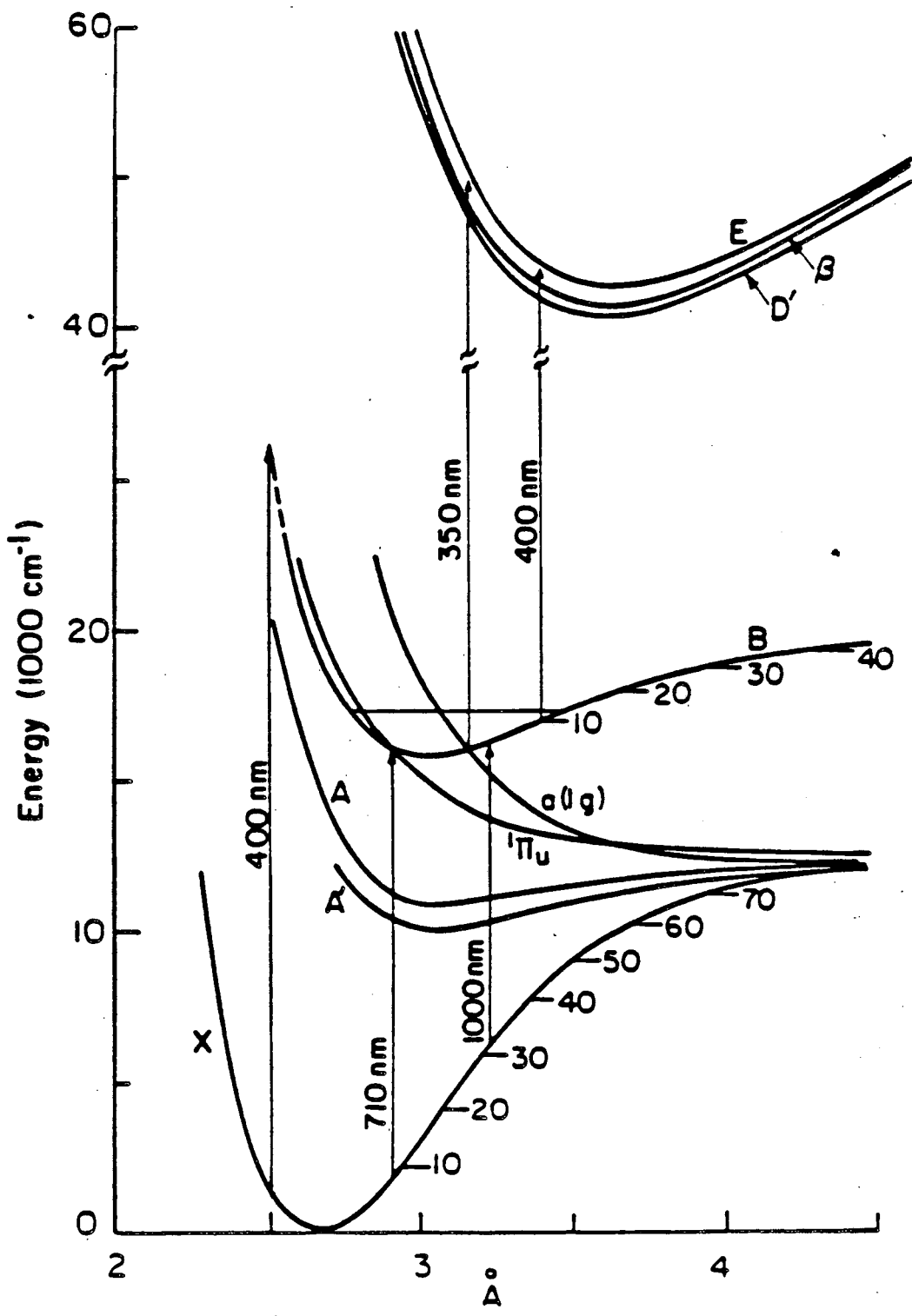


Figure 1

## II. EXPERIMENTAL

The iodine reaction was initiated with light at 590 nm, a wavelength which gives 87% excitation to the predissociative B state and 7% and 6%, respectively to the directly dissociative  $^1\Pi_u$  and A states (Fig. 1).<sup>32</sup> At 590 nm, molecules are primarily excited from the  $v=1,2$  levels of the X state to the  $v=12-14$  levels of the B state (Fig. 1).<sup>33</sup> Light pulses at 590 nm were generated by a synchronously-pumped dye laser and were amplified at 10 Hz in a three-stage dye amplifier pumped by a Q-switched Nd:YAG laser.<sup>34</sup> The amplified pulse of 0.8 mJ was approximately one picosecond long and had shot-to-shot energy fluctuations of  $\pm 10\%$  rms. Further details of the design and performance of the picosecond laser system may be found in Chapter 5.

The transient absorption apparatus used from 350-1000 nm is diagrammed in Fig. 2. The amplified pulse was first split by a beamsplitter; 50% formed the excitation pulse and 50% was used to generate a probe continuum. The excitation pulse passed through a computer controlled delay line and through filters which blocked interfering emission at long wavelengths from the last amplification cell. The excitation polarization was controlled with a half-wave plate.

A white light continuum, extending from 310 to  $>1000$  nm, was generated by focusing the probe beam with a 6 cm focal length lens into a 5 cm cell of water. The continuum was recollimated and a bandpass filter ( $\Delta\lambda \sim 10$  nm) selected a single probe wavelength. This light was spatially filtered to improve its spatial quality and focusing properties. Two uncoated silica flats each reflected 10% of this beam

to form the reference and sample probe beams. The second flat also served to collinearly recombine the excitation and probe beams. A 20 cm focal length lens focused both beams into the sample which was placed 16 cm behind the lens. The two beams formed nearly identical 800  $\mu\text{m}$  spots (50% transmission diameter) in the sample.

For absorption measurements at 295 nm a different arrangement was used (not shown). The entire laser pulse was reduced by a telescope to a collimated 2 mm beam and passed through a 1 mm KDP doubling crystal. The beam was then re-expanded and the  $\sim 10\%$  which had been converted to 295 nm was separated by a dichroic filter. The visible beam passed through a variable delay line. After a small portion of the UV was split off as a reference beam, the UV probe and visible excitation pulse were collinearly recombined on a second dichroic and focused through the sample with the same geometry described above.

With either arrangement, the excitation pulse was blocked after the sample with a combination of dielectric interference and absorbing glass filters. Both the reference and the sample probe beams were measured by identical 1 cm diameter photodiodes (EG&G DT-110). The current pulses from the photodiodes were digitized in 10-bit current-integrating gated A/D converters, which were interfaced to a minicomputer. The reference and sample signals were ratioed to correct for shot-to-shot variations in the probe intensity and then averaged. A 1-ps time resolution in this experiment is indicated by both autocorrelation measurements of the initial laser pulse and by the fastest risetimes observed in the experiment.

The absorption changes were often small because the excitation density could not be further increased without generating a small amount

of continuum in the sample, which interfered with measurements at the probe wavelengths. Thus, special care was needed in these experiments to reduce noise. Experiments were performed with one probe wavelength at a time, because the dynamic range of multichannel detectors restricts the signal-to-noise attainable. Because of spectral fluctuations of the probe continuum within the pass band of the wavelength selecting filter, any optical element with a slope in its absorption had to be duplicated in both the sample and reference beams. In particular, identical samples and filters were placed in both beams. With proper precautions, the ratio of sample to reference intensities could be measured in a single shot with a fractional error (s.d./mean) of as low as  $2 \times 10^{-3}$ . Typical decay curves containing 200-300 delay points were scanned 4-5 times averaging 10-25 laser shots at each delay. The scans were then averaged to give a total of 50-100 laser shots per delay point, which reduced the noise to a few parts in  $10^4$ . Thus even with transmission changes of only 1%, signal-to-noise ratios of 30-100 could be achieved in 1-2 hrs of data collection.

Data was taken for iodine solutions in  $\text{CCl}_4$ ,  $\text{CHCl}_3$ ,  $\text{CH}_2\text{Cl}_2$ , hexane, nonane, hexadecane, and cyclohexane. Alkane and chloroalkane solvents were chosen because of their low propensity for complex formation with iodine molecules or atoms, and the absence of contact charge-transfer absorption from molecules in the spectral region examined.<sup>35-40</sup> All solvents were Burdick and Jackson chromatography grade. Less pure spectral grade solvents showed additional ultraviolet absorption features attributed to iodine-impurity interactions.<sup>35,41</sup> The iodine crystals (Mallinckrodt analytical reagent grade, >99.8%  $\text{I}_2$ ) were used as received. Iodine concentrations were set to give an absorbance of

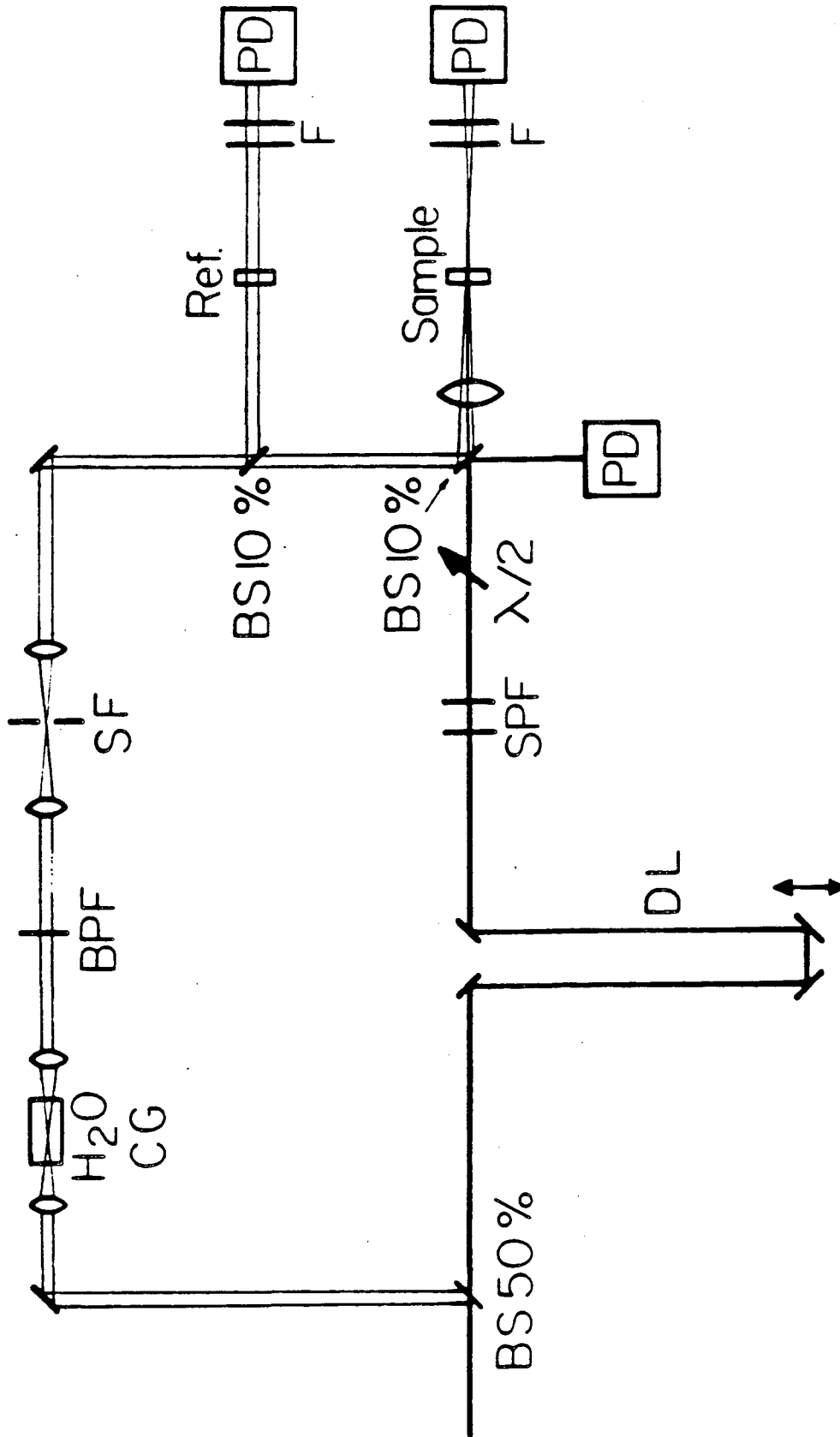
$0.40 \pm 0.01$  at 590 nm in the 5 mm sample cell ( $\sim 5$  mM). Reducing the concentration by a factor of five caused no change in the decay curves in hexane and  $\text{CCl}_4$  at either 635 nm or 295 nm. However, raising the concentration by a factor of five did cause some changes at 295 nm. These artifacts could have been caused by excited state quenching<sup>6</sup> or by the presence of dimers.<sup>42</sup> At the concentrations used, the excitation density is low enough that the non-geminate recombination time can be calculated to be  $> 1 \mu\text{s}$ ,<sup>43</sup> which can be entirely neglected on the time scale of these experiments.

The excitation intensity was relatively reproducible from day to day; the maximum absorption change on identical curves run on different days was reproducible to about  $\pm 30\%$ . Thus, absorbance changes at different wavelengths and in different solvents may be roughly compared. Exceptions are the data at 295 nm which are estimated to be uncertain by a factor of two relative to the continuum probe data because of the different experimental setup. Several curves were also taken with 3x and 5x lower excitation intensity to insure that no intensity dependent effects were present.

Transient absorption curves were taken at 1000 nm, 860 nm, 710 nm, 635 nm, 500 nm, 350 nm, and 295 nm in most solvents. In addition, absorption measurements were made at 370 nm, 400 nm, and 760 nm in  $\text{CCl}_4$  and at 400 nm in hexane. Attempts were made to collect data at 430 nm, but the absorption changes were too small for meaningful results to be obtained. Both perpendicular and parallel polarization measurements were made for most wavelength/solvent combinations. No polarization effects were seen. At some wavelengths, a nonlinear interaction, which occurred when pump and probe pulses were temporally overlapped, caused

an artifact near zero time when both polarizations were parallel. The artifact was greatly reduced by using perpendicular polarizations.

FIG. 2. Picosecond absorption experiment (1000-350 nm). Heavy line - excitation pulse path, double line - probe pulse path. BS - beamsplitter, DL - delay line, SPF - short pass filters,  $\lambda/2$  - half-wave plate, CG - continuum generation cell, BPF - bandpass filters, SF - spatial filter, PD - photodiode, F - filters, REF - reference sample, SAMPLE - primary sample.



XBL 64 11-6120

Figure 2

### III. RESULTS

In this section, the results are discussed beginning with the slowest transient absorption components and ending with the fastest. The slow, intermediate, and fast transient components in each solvent will be assigned to the recombined molecule's A'-state, X-state, and B-state dynamics, respectively. In order to allow quantitative investigation of the faster X-state and B-state dynamics, the slower A'-state component will be subtracted from the data. Finally, a reaction model is summarized, and an upper bound on the geminate recombination time is inferred.

The transient absorption curves in the chlorinated methanes, the straight alkanes, and cyclohexane initially appear distinct, based on their overall kinetic behavior. In the chlorinated alkanes (Figs. 3-5), the absorption decays extend beyond 900 ps and clearly have two components, while in the alkanes (Figs. 6-8) the absorption decays are complete within 200 ps and two components are not as clearly separated at the red wavelengths. Cyclohexane differs from the straight alkanes in that it has unusual double peaked absorption curves which are not seen in the other solvents (Fig. 8). As will be seen, however, all these differences can be explained in terms of a change in the relative time scales of the decay processes.

#### A. Long Time Decays: A'-State Trapping

The first transient absorption feature to consider is a slowly decaying component which appears at red (635-1000 nm) and UV (400-295 nm) wavelengths. In the chlorinated methane solvents, this component is slow enough (>500 ps decay time) to be well-resolved from other, faster decaying components (see e.g., Fig. 3). The decay time of this component is the same in both the red and UV and is wavelength independent within each region. This indicates that the slowly decaying absorption component is due to a single state or to a closely coupled set of states. In the alkane solvents, a slow UV decay component is again well-resolved from an early time transient (see e.g., Fig 6), and it has a spectrum similar to the slow UV component in the chlorinated methane solvents. This absorption is assigned to the same state seen in the chlorinated methanes, even though its decay time is much faster (~65 ps decay time). A corresponding component with the same decay time found in the UV also appears in the alkane red absorptions, although this component is not as well separated from the early components as it is in the chlorinated methane solutions. The data thus indicate that following photodissociation in all of these solvents, a state is populated which absorbs at both red and UV wavelengths.

Kelley et al. have previously observed the long decay component in the red, although they could not resolve it from the other absorption components in the alkane solutions.<sup>4,5</sup> They assigned the absorption to iodine molecules trapped in either the A or A' state (Fig. 1). These are the only two excited states which correlate with two ground state atoms and which are bound by significantly more than  $kT$  ( $1640 \text{ cm}^{-1} A$

state,  $2500\text{ cm}^{-1}$  A' state).<sup>44-46</sup> This assignment is supported by the identification of trapping to both the A and A' states following photodissociation of iodine in matrices.<sup>47</sup> Since the same state appears to be responsible for both the red and UV absorptions, the UV absorptions can also be assigned to the A or A' state.

To more clearly illustrate the points just discussed, representative data is shown in Figs. 3-8. Figure 3 shows the long A/A'-state decay component in  $\text{CCl}_4$  solution at red wavelengths, as well as an early time (<200 ps) transient, which is discussed in the next section. The red absorption behavior is similar in other chlorinated methane solvents as Fig. 4 shows for 635 nm absorption. Figure 5b illustrates the slow UV absorption component in  $\text{CCl}_4$  solution. As previously noted, this component has the same decay time as the long component in the red absorption. In the chlorinated methanes, the most accurate A/A'-state lifetimes were obtained at 635 and 710 nm (Table I). It was assumed that the absorptions decay exponentially to zero as found by Kelley et al.<sup>4</sup> Within both the UV and red regions, the A/A'-state absorption is strongest at short wavelengths and weaker at long wavelengths. An experimental A/A'-state absorption spectrum in  $\text{CCl}_4$  was determined by fitting exponential curves to the long time decays and extrapolating to zero time (see Fig. 11).<sup>48</sup>

The UV absorption of the A/A' state in hexane appears as the longer decay component at 295 nm and 350 nm in Fig. 6a. A small component at 400 nm is discussed in Sec. IIIB. Similar absorptions were observed in the other alkane solvents. The corresponding red absorption component in hexane is illustrated in Fig. 7. The red absorption data show two decay components, the longer of which matches the A/A'-state decay time

found in the UV (solid curves at 710 and 860 nm). Since the early red absorption recovers more slowly at shorter wavelengths (Figs. 3,7, and 8), the 65 ps A/A'-state decay is not resolved at 635 nm. Because of the difficulty of separating the red absorption components in the alkanes, the 350 nm absorptions give the best A/A'-state lifetimes in those solvents (Table I). As in the chlorinated methane solvents, the A/A'-state absorption is weaker at longer wavelengths within both the red and UV regions. The overall similarity of the behavior at different wavelengths identifies the longer absorption component in both the alkanes and chlorinated methanes as arising from the same source despite the disparity in the lifetimes.

In addition to the transient UV absorption components, a long, non-decaying UV absorption occurs in alkane solvents (Fig. 6b and Table II). This absorption offset probably results from solvent-contact charge-transfer transitions of free iodine atoms which have escaped recombination.<sup>39</sup> The charge-transfer absorption spectrum is known and is strongly solvent dependent. The UV free atom offset should not be substantial in chlorinated methane solvents except at 295 nm.<sup>39</sup> In fact, long time offsets must be assumed at 295 nm in the chlorinated methane solvents to match the A/A'-state lifetime found at other wavelengths (Table II).

At wavelengths near the peak of the molecular ground state absorption (450-570 nm), there is a net absorption decrease (bleach) following photodissociation, due to the loss of ground state molecules. In chlorinated methane solvents, Kelley et al. showed that the absorption recovery has a component with the same lifetime as the A/A' state.<sup>4</sup> This occurs because the A/A' state decays back to the X

state causing a return of the ground state molecular absorption. In addition, a partial bleach remains at long times, because a fraction of the atoms do not geminately recombine. In the chlorinated methane solutions, the recovery extends beyond the delay range used in this experiment (Fig. 9), so that independent measurements of both the decay time and the long time bleach are not possible. However, the data is consistent with the A/A'-state lifetimes determined at other wavelengths, if a moderate long time offset is assumed (Table II). The bleach component due to trapping in the A/A' state is a large fraction of the total bleach implying that 50% or more of the recombined molecules are initially trapped in this excited electronic state. In the alkane solutions, the shorter time recovery component which obscures the A/A'-state 635 nm absorption also obscures the bleach recovery from A/A'-state decay (Fig. 10). However, the data in these solvents is consistent with part of the recovery being due to A/A'-state decay. The long time bleach due to escaped atoms is easily measured in the alkanes and is included in Table II.

The question of whether the A state, A' state, or both is being monitored can now be addressed. If the rate of exchange between the A and A' states is fast in the liquid, nearly all the population would reside in the lower A' state. On the other hand, if the exchange between A and A' states is slow and their decay rates back to the X state are not identical, a multi-exponential X-state recovery would be expected. Since the UV absorption, red absorption, and green bleach all show the same single exponential behavior, it appears that only one excited trap state is important.

The identity of this state is indicated by an ultraviolet

absorption in gas-phase iodine which has recently been assigned to the  $D' \leftarrow A'$  transition (Fig. 1).<sup>49</sup> The liquid phase  $D' \leftarrow A'$  spectrum can be approximated by assuming that it has the same gas-to-liquid shift and broadening as the  $D' \leftarrow X$  transition (Fig. 11).<sup>50</sup> In the UV, the agreement between the predicted and experimental spectra (Fig. 11) shows that the long time absorption can be reasonably assigned to the  $D' \leftarrow A'$  transition. The red absorption must also originate from the  $A'$  state, since only one trap state is important. Several final states with the proper energy and symmetry for red absorptions from the  $A'$  state exist, but it is not possible to decide which is the most important.<sup>44</sup> Abul-Haj and Kelley also conclude that the red absorptions are due to the  $A'$  state using somewhat different arguments.<sup>6</sup> Although this assignment is not definitive, only the  $A'$  state will be referred to in the following sections.

FIG. 3. Transient long wavelength absorptions of  $I_2$  in  $CCl_4$ . Note vertical scale changes in this and subsequent figures (4 ps/pt).

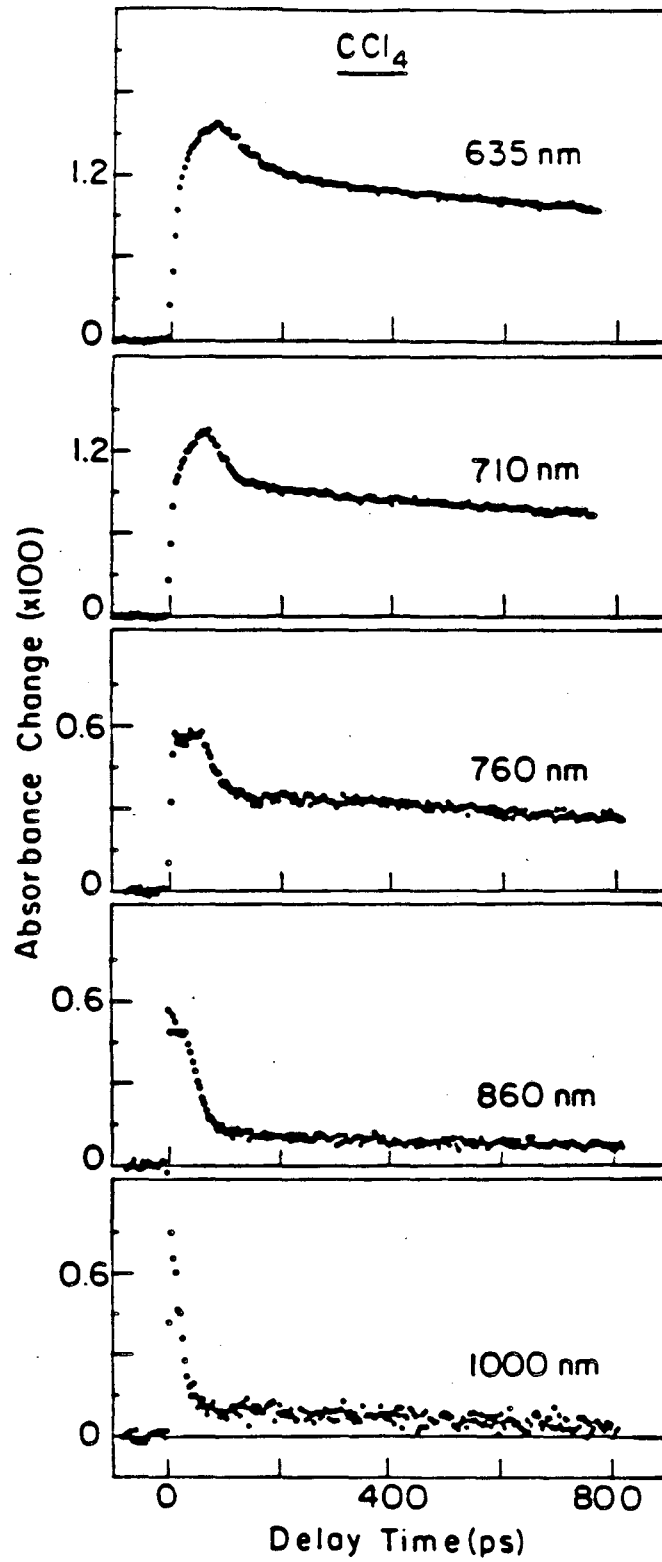


Figure 3

FIG. 4. Transient absorption at 635 nm of  $I_2$  in chlorinated methanes. Lines represent the A'-state absorption component (4 ps/pt).

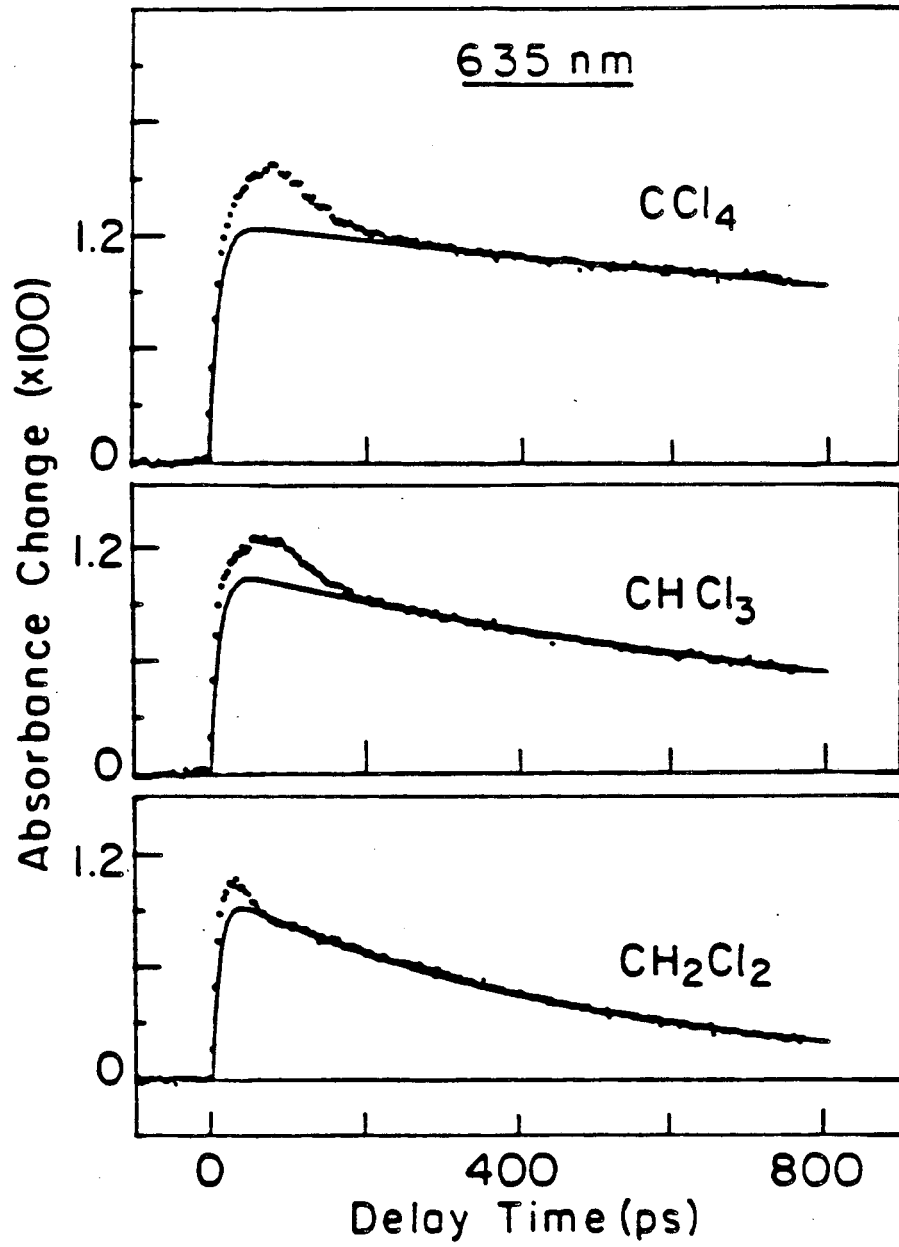
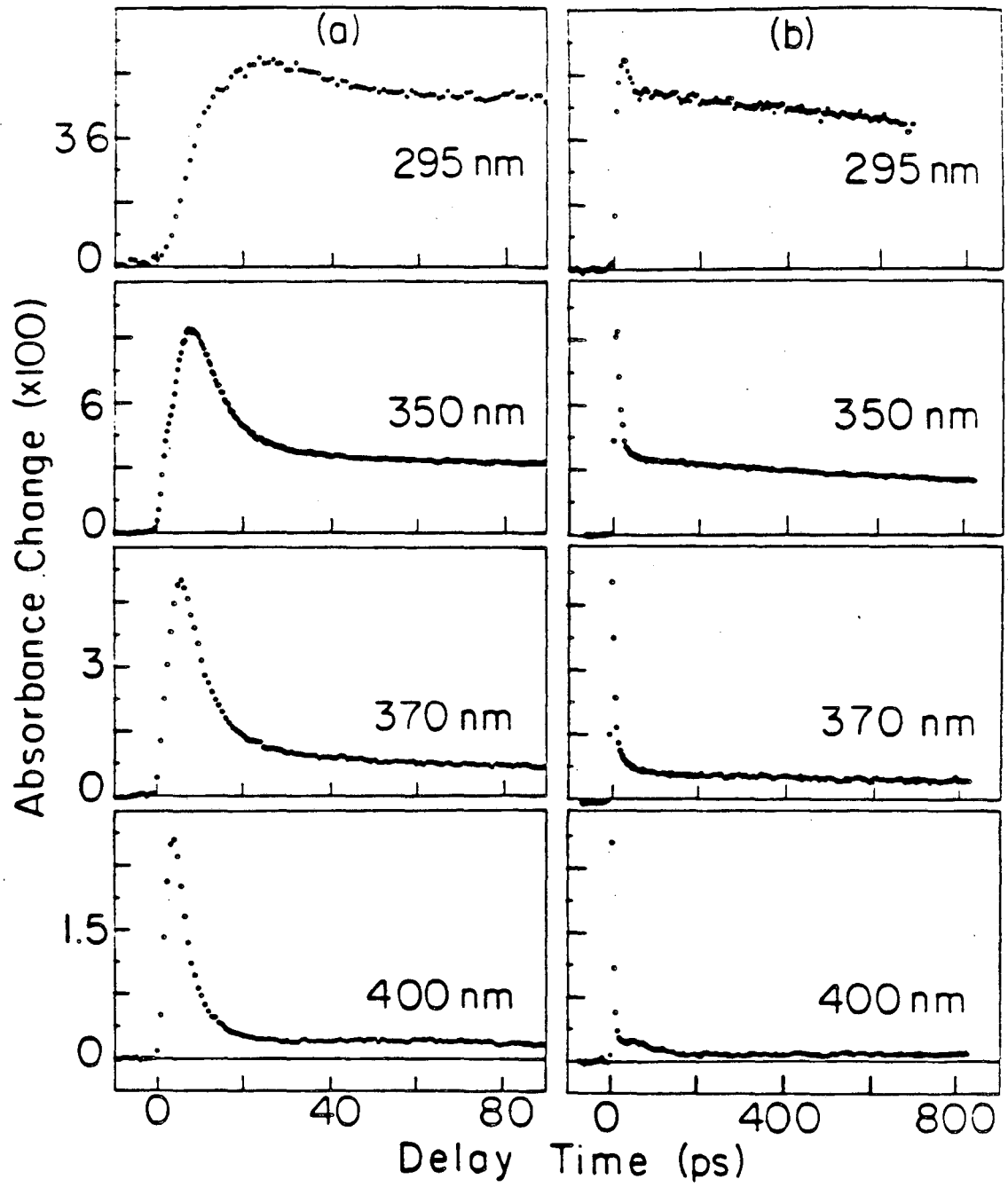


Figure 4

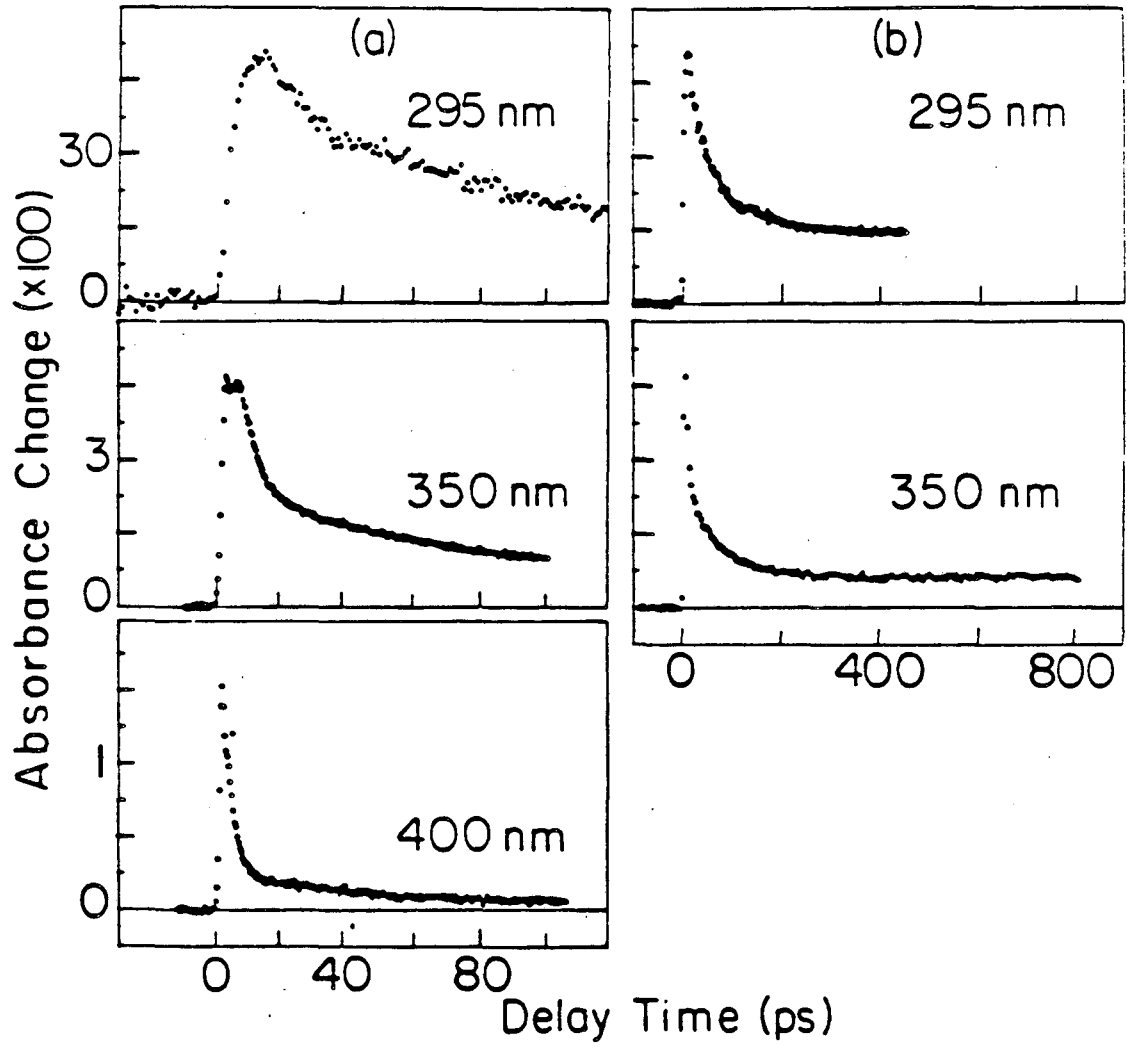
FIG. 5. Transient UV absorptions of  $I_2$  in  $CCl_4$ , on two time scales. The early component is assigned to B-state absorption and the long component to A'-state absorption. The small intermediate time component at 400 nm is expanded in Fig. 12. a) 295 nm - 1.1 ps/pt, 350 nm - 0.4 ps/pt, 370 and 400 nm - 0.8 ps/pt. b) 4 ps/pt, except 295 nm is 5.3 ps/pt.



XBL 857-6493

Figure 5

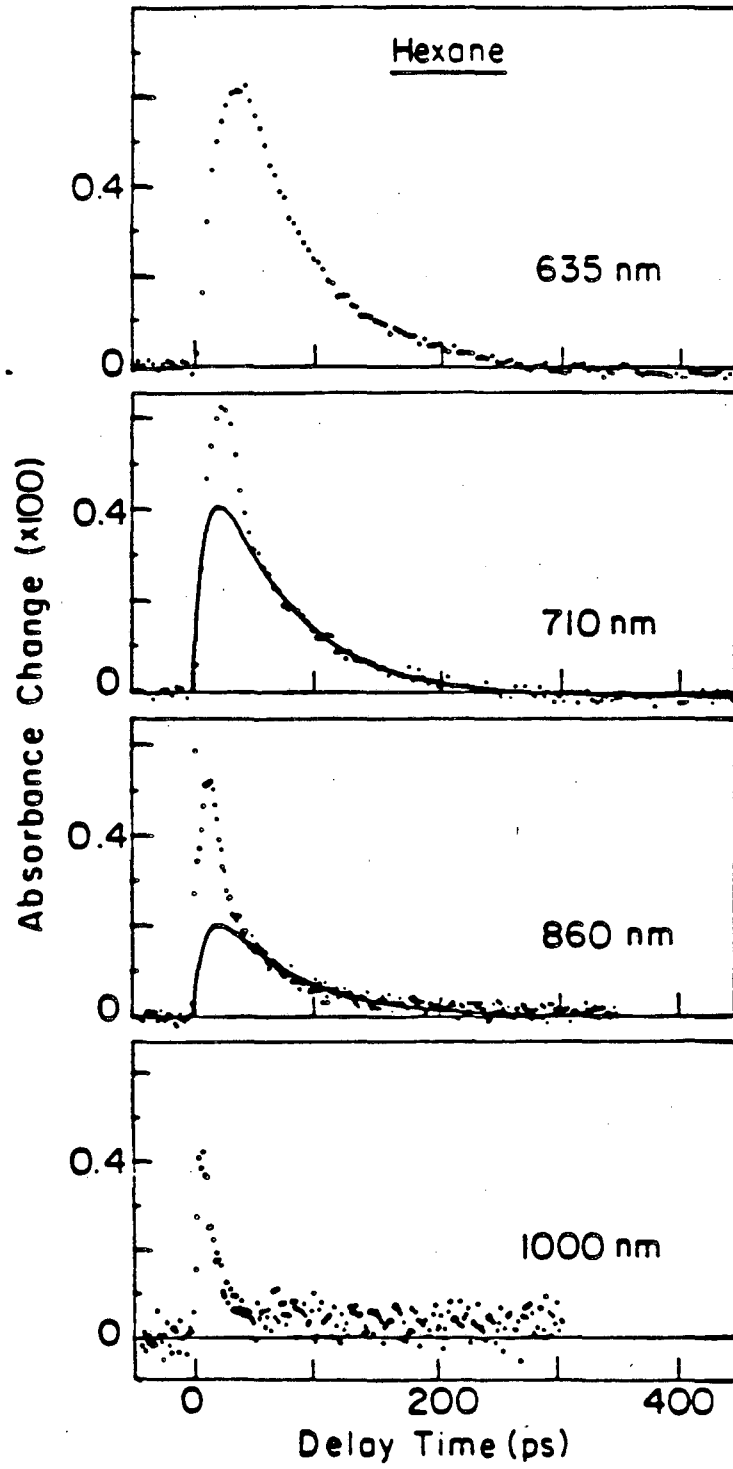
FIG. 6. Transient UV absorptions of  $I_2$  in hexane, on two time scales. The early component is assigned to B-state absorption and the 65 ps component to A'-state absorption. The long time offsets at 295 and 350 nm are assigned to escaped atoms. a) 295 nm - 2.1 ps/pt, 350 and 400 nm - 0.4 ps/pt. b) 295 nm - 2.1 ps/pt, 350 nm - 4 ps/pt.



XBL 857-6494

Figure 6

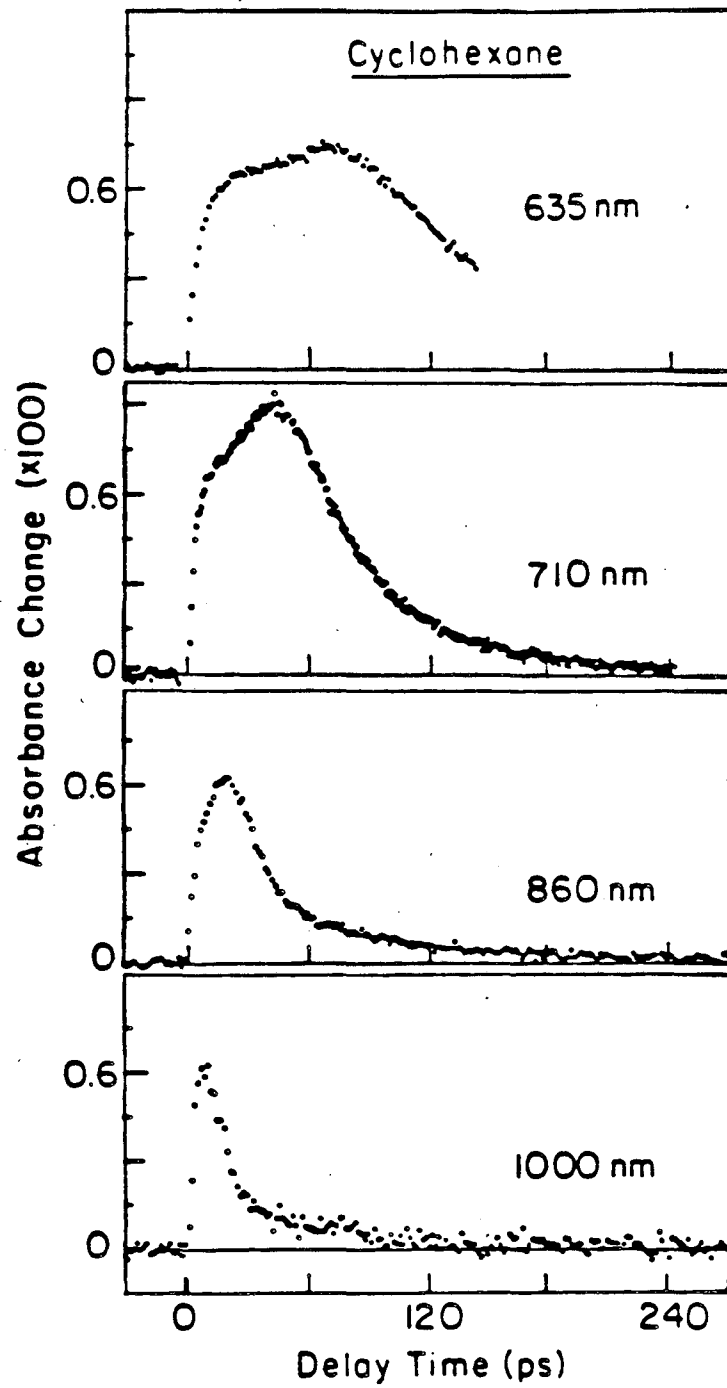
FIG. 7. Transient long wavelength absorptions of  $I_2$  in hexane. Lines represent the A'-state absorption component, with decay times fixed by UV A'-state absorption (635 and 710 nm - 4 ps/pt, 860 and 1000 nm - 1.6 ps/pt).



XBL 857-6487

Figure 7

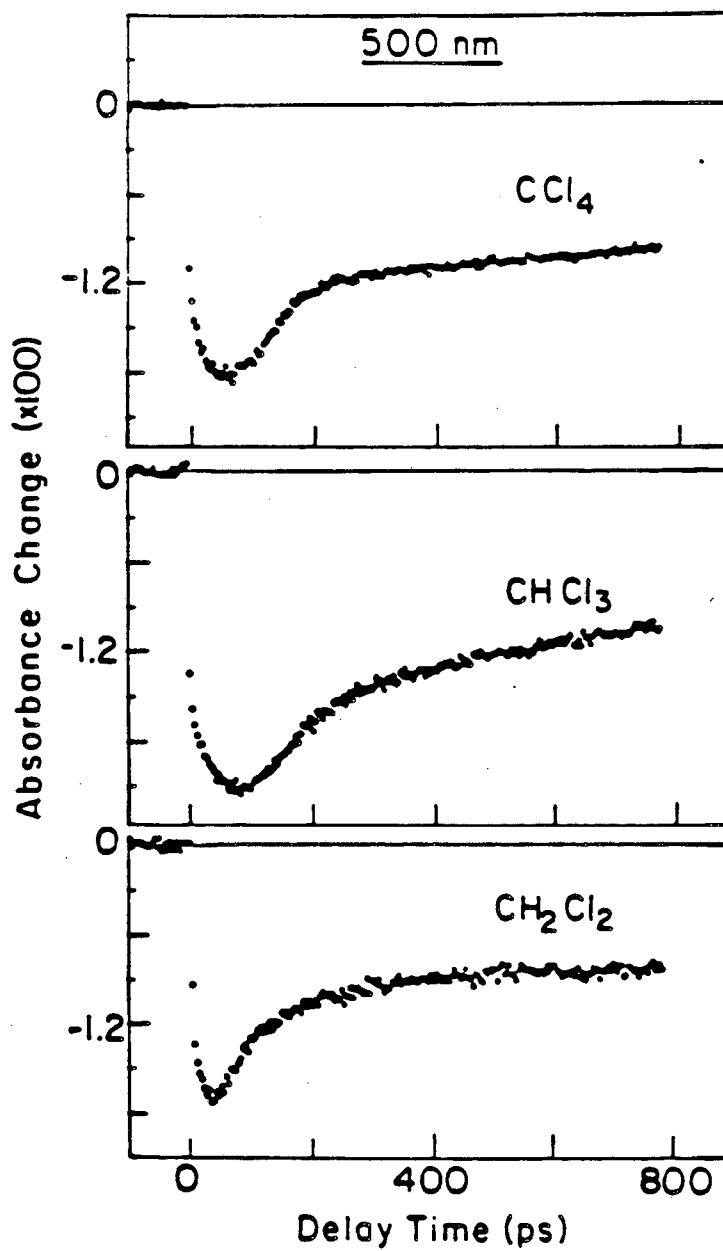
FIG. 8. Transient long wavelength absorptions of  $I_2$  in cyclohexane  
(1.6 ps/pt, except 710 nm is 0.8 ps/pt).



XBL857-6484

Figure 8

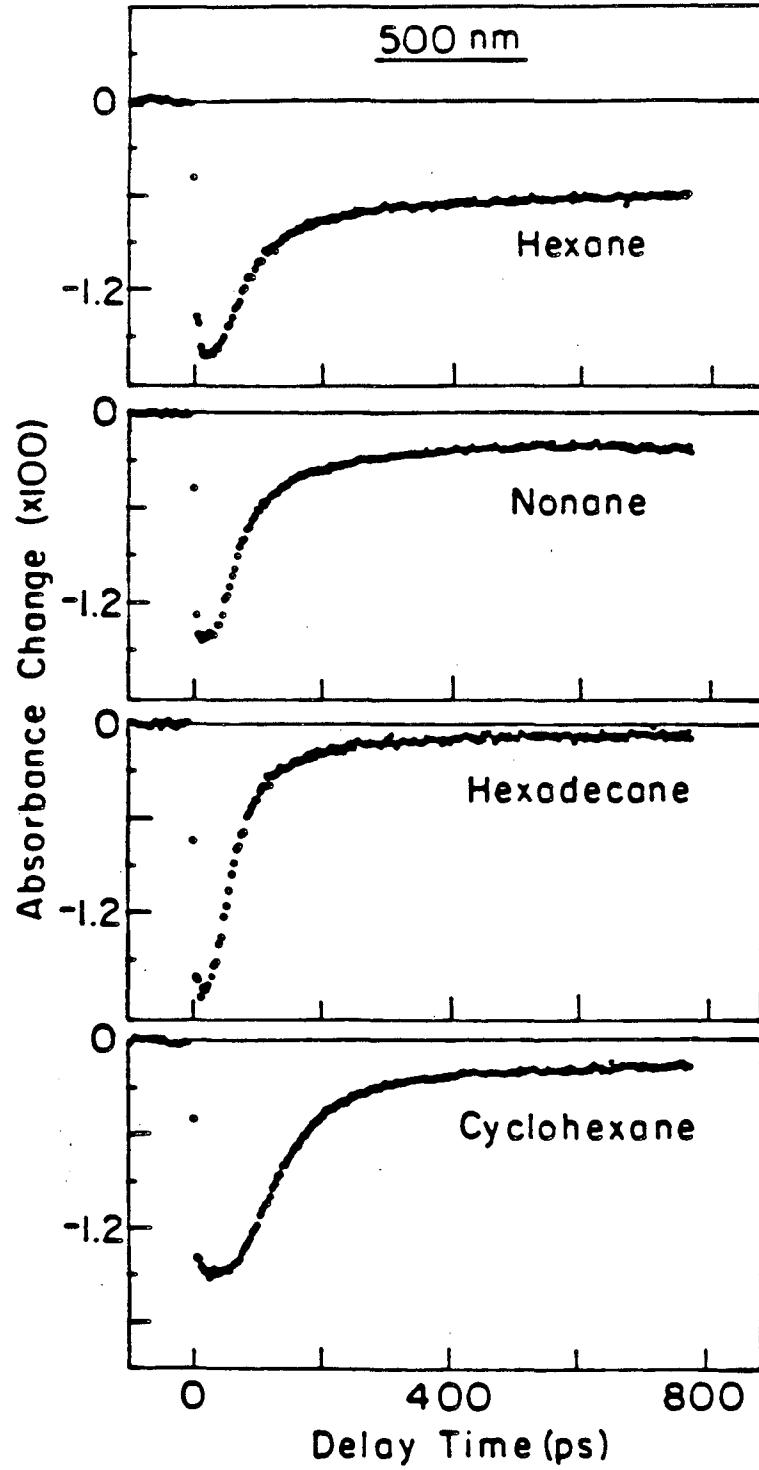
FIG. 9. Transient bleach at 500 nm of  $I_2$  in chlorinated methanes  
(4 ps/pt).



XBL 857-6486

Figure 9

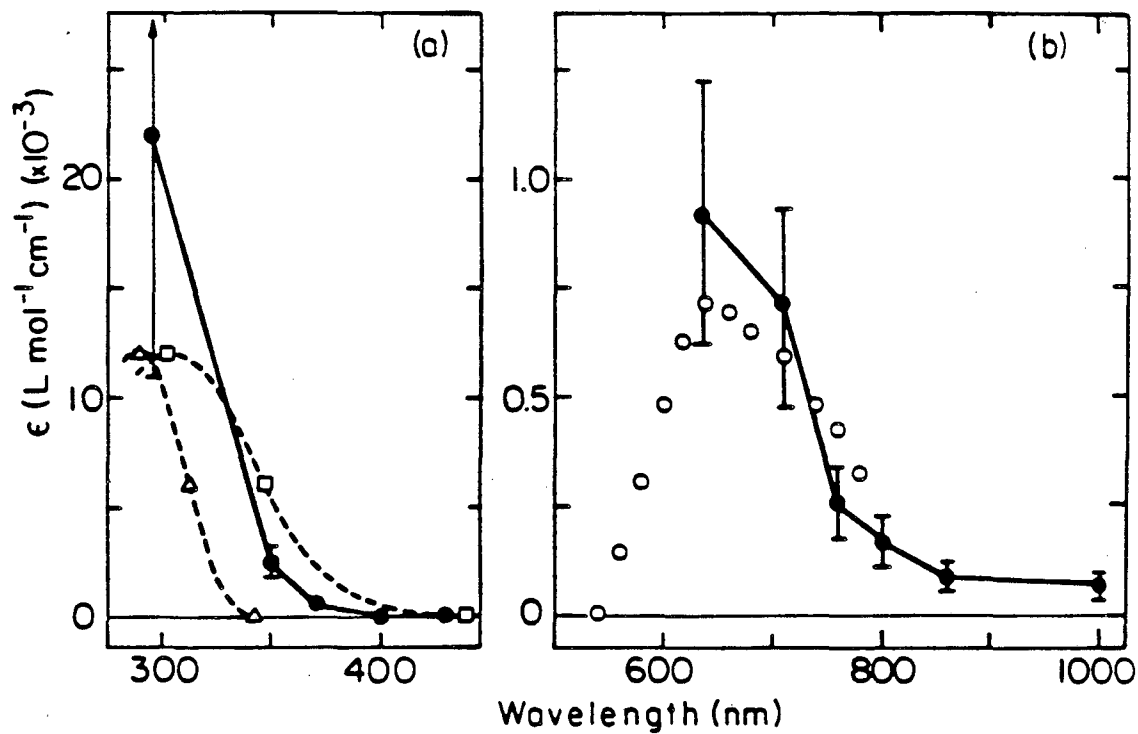
FIG. 10. Transient bleach at 500 nm of I<sub>2</sub> in alkanes (4 ps/pt).



XBL 857-6485

Figure 10

FIG. 11. Absorption spectrum of the iodine A' state measured in  $\text{CCl}_4$ :  
a) UV spectrum, b) Vis/IR spectrum. ● -this work, ○ -values  
obtained from Fig. 3 of Ref. 4,  $\Delta$  -approximate gas phase D'+A'  
absorption spectrum (Ref. 49),  $\square$  -estimated D'+A' liquid phase  
spectrum.



XBL 857-6479

Figure 11

TABLE I. A'-State Lifetimes

<u>Solvent</u>	<u>Decay Time (ps)</u>	
	<u>This work<sup>c</sup></u>	<u>Ref. 4</u>
CCl <sub>4</sub>	2700±400 <sup>a</sup>	2700
CHCl <sub>3</sub>	1120±100 <sup>a</sup>	980
CH <sub>2</sub> Cl <sub>2</sub>	510± 30 <sup>a</sup>	500
Hexane	66± 8 <sup>b</sup>	~100
Nonane	64± 4 <sup>b</sup>	---
Hexadecane	59± 6 <sup>b</sup>	~90
Cyclohexane	71± 9 <sup>b</sup>	---

a) Times based on absorption decays at 710 and 635 nm.

b) Times based on absorption decay at 350 nm.

c) Error limits are values which double the  $\chi^2$  value in the data fit.

TABLE II. Long Time Absorption Offset Magnitude

<u>Solvent</u>	<u>Fraction of Peak Height</u>		
	<u>Wavelength (nm)</u>		
	<u>500 nm<sup>a</sup></u>	<u>350 nm<sup>b</sup></u>	<u>295 nm<sup>b</sup></u>
CCl <sub>4</sub> <sup>c</sup>	(0.0)	(0.0)	(0.27)
CHCl <sub>3</sub> <sup>c</sup>	(0.12)	(0.0)	(0.12)
CH <sub>2</sub> Cl <sub>2</sub>	0.40	0.0	0.30
Hexane	0.38	0.14	0.29
Nonane	0.16	0.08	----
Hexadecane	0.05	0.03	----
Cyclohexane	0.12	0.07	0.10

- a) Bleach offset (negative absorbance change).
- b) Positive absorbance change
- c) Offsets approximate due to slow A'-state decay.

## B. Intermediate Time Recovery: X-State Vibrational Dynamics

In addition to the A'-state absorption, all the absorption curves show other features occurring at earlier times. At the red wavelengths (635-1000 nm), there is a component which both rises and decays quickly at long wavelengths, but which becomes slower at shorter wavelengths (Figs. 3 and 4). In the alkanes, this component is resolved at longer wavelengths, but at 635 nm its recovery is slow enough that it is difficult to distinguish from the A'-state absorption (Figs. 7, 8). The wavelength dependence of the rise and decay times implies a time dependent absorption spectrum which is initially peaked at long wavelengths, but shifts to shorter wavelengths with time.

Just such a shifting absorption spectrum has been predicted to result from vibrationally excited molecules in the X state.<sup>3,9,10,31</sup> By a classical Franck-Condon argument, the maximum absorption strength occurs for a wavelength corresponding to a vertical transition between classical turning points. Since the X-state absorption is dominated by the B $\rightarrow$ X transition, the wavelength of maximum absorption for a given vibrational level can be related to the difference between the X and B potential curves (Figs. 1, 16). Thus when atoms first recombine in the X state and are highly vibrationally excited, their absorption will lie at wavelengths  $>1 \mu\text{m}$ . As they relax, the absorption maximum moves to shorter and shorter wavelengths, until it matches the normal ground state absorption when the molecules are completely relaxed. Since this is exactly the behavior experimentally observed, the early time component of the red absorptions can be assigned to molecules which

initially recombine on the X state, but which are still vibrationally excited.

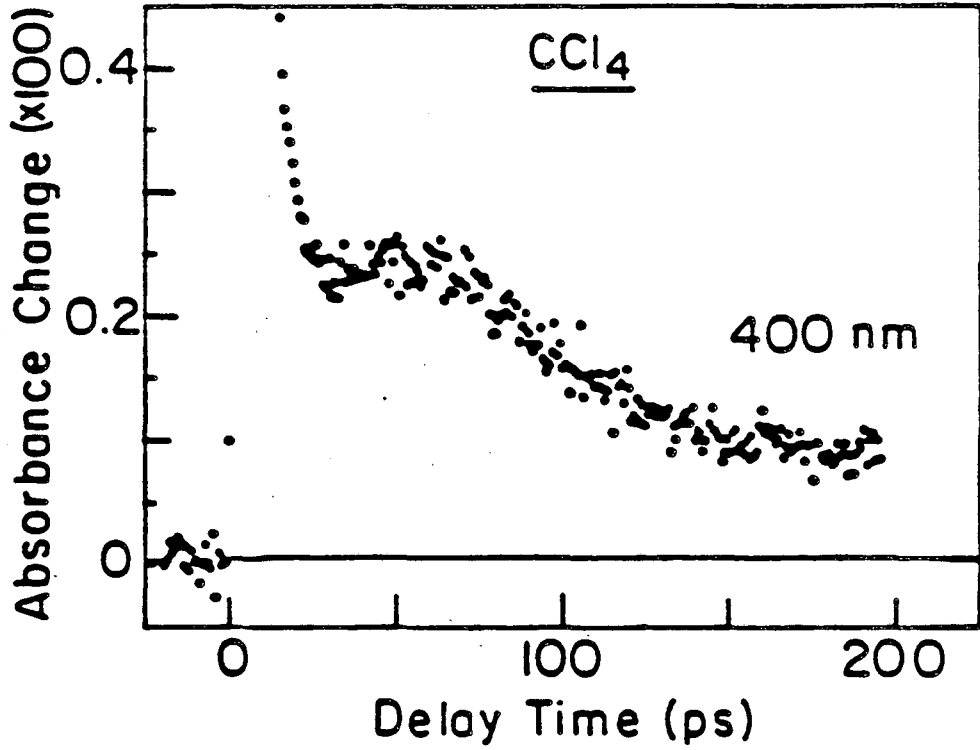
These arguments also imply that there should be a branch of the absorption spectrum of the vibrationally excited molecules on the short wavelength side of the ground state absorption spectrum.<sup>31</sup> This absorption arises from the vertical transitions starting on the inner turning point (Fig. 1) and will be weak since the molecule classically spends less time at this turning point. A weak absorption component with the correct timescale is seen at 400 nm in CCl<sub>4</sub> and hexane solutions (see e.g., Fig. 12). At the other UV wavelengths, absorption from excited vibrational levels is masked by other, stronger absorptions. Based on the classical Franck-Condon model and a knowledge of the potential curves, an absorption at 400 nm arises primarily from vibrational levels between the levels responsible for 635 and 710 nm absorption and would be expected to show a time behavior intermediate between the behavior at these two wavelengths. This is, in fact, the case.

The effects of vibrational relaxation are also seen in the recovery of absorption at 500 nm. The curves for the chlorinated methane solutions (Fig. 9) show a short time component which recovers just after the vibrational component of the 635 nm absorption decays (Fig. 4). In previous work, this component has been interpreted as a direct measure of the cage recombination time.<sup>2,4,26-28</sup> However, the smooth progression of times for vibrational relaxation measured in the red to the time measured in the green indicates that this component actually represents the final stage of vibrational relaxation of those molecules which originally recombined on the X state. In the alkane solvents

(Fig. 10), the A'-state electronic relaxation and the last stages of X-state vibrational relaxation occur on such similar timescales that separate recovery components are not distinguishable.

It is now possible to understand the origin of the unusual double peaked absorption curves seen in cyclohexane (Fig. 8). At the longest wavelengths, the curves are similar to those in linear alkanes, with a slow component which has a decay time matching the A'-state lifetime deduced from the UV data. However, the vibrational component is slower than in the linear alkanes. At 710 and 635 nm, the vibrational relaxation component in cyclohexane is slow enough that it recovers more slowly than the A'-state lifetime. This leads to double peaked absorption curves in which the first peak results from the A'-state absorption and the second peak from absorption due to lower vibrational levels of the X state.

FIG. 12. Transient absorption at 400 nm of  $I_2$  in  $CCl_4$ , on an expanded vertical scale (0.8 ps/pt). See also Fig. 5.



XBL 857-6488

Figure 12

### C. Early Time Absorptions: B-State Predissociation Dynamics

The remaining features of the decay curves occur within the first 20 ps. First, although a large fraction of the bleach occurs with the pulsewidth-limited risetime, the maximum bleach does not occur until 20-50 ps later (Figs. 9, 10). It has been previously hypothesized that the bleach maximum is delayed because the initially populated B state has some absorption near 500nm.<sup>2</sup> This residual absorption would not disappear until the B state predissociates. The present data show that the bleach rise occurs in two stages, as required by this hypothesis.

During the same time period, there is a very strong absorption from 400-350 nm (Figs. 5a, 6a). The absorption rises quickly at all wavelengths, but the risetime is pulsewidth-limited only at 400 nm. In  $\text{CCl}_4$ , the absorptions at 400, 370 and 350 nm have progressively longer rise and decay times; hexane shows a similar shift between 350 and 400 nm. At 350 nm, the other solvents have a delay in maximum absorption and a short decay component similar to that seen in  $\text{CCl}_4$  and in hexane. Based on the pulse-limited rise at 400 nm, this absorption can be assigned to the first state populated, the B state. The decay time is then consistent with the predissociation timescale deduced from the 500 nm bleach recovery. The final state for the UV absorption would be either the  $\beta$  or the E states<sup>51,52</sup> (Fig. 1), both of which are at the correct energy and have the correct symmetry for an allowed transition from the B state.

The wavelength dependence of the UV absorption kinetics are explained by vibrational relaxation within the B state. Using the same Franck-Condon arguments used to explain the effects of X-state

vibrational relaxation, it can be seen that the absorption will be shifted to longer wavelengths in higher B-state vibrational levels (Fig. 1). Thus, the initially populated vibrational levels ( $v=12-14$ ) will absorb strongly at 400 nm, and the absorption will decline both from predissociation and from relaxation to lower vibrational states. The absorption at 350 nm is strongest for low lying vibrational states, however, so the absorption does not reach a maximum until there has been some vibrational relaxation. The curves at 295 nm also show a small early component (Fig. 5, 6). Although in general it is similar to the early absorption seen from 350-400 nm, it appears to be somewhat too long (20-35 ps) to arise from the B state. At present the origin of this absorption is still uncertain.

In chlorinated solvents, the red absorptions (635-1000 nm) also show an early time (<20 ps) component. This component is clearest in the high resolution data in Fig. 15. This component becomes stronger at longer wavelengths, so it is undetectable at 635 nm, clearly resolvable at 760 nm, and dominant at 1000 nm. At 1000 nm, this component is so strong and the vibrational relaxation component so fast, that a faint, but reproducible, shoulder on the  $\text{CCl}_4$  data is the only clue that two components exist. It is difficult to obtain precise information on this absorption, because it is so strongly mixed with the rise of the vibrational and A'-state components. However, its rapid rise and decay suggest that it arises from the B state.

#### D. Separation of Absorption Components

The slowly recovering absorption from A'-state molecules and escaped atoms complicate quantitative analysis of the faster X- and B-state dynamics. For this reason, the slower contributions were subtracted from the data. The A'-state decay times and absorption magnitudes, as well as the offsets from escaped atoms are fixed by the long time portions of the data (Tables I and II). An exception occurs with alkane solvents at 500 nm, and in some cases at 635 nm, where the A'-state and X-state contributions are not well resolved. In these cases, subtractions were not performed.

The primary complication to the subtraction was the assignment of a risetime to the A'-state absorption. For simplicity, the rise was assumed to be exponential, although it probably has a more complicated functional form. The fast, smooth rising edge at 635 nm suggests an A'-state rise time which is definitely slower than 8 ps, but which is not much slower than 15 ps (Fig. 13). In addition, rise times as long as 20 or 25 ps are too slow to meet the beginning of the single exponential portion of the A'-state absorptions at 350 nm (Figs. 13 and 14). In particular, the absence of a dip in the 350 nm absorptions as the A' state rises indicates that this rise time cannot be much slower than the decay time of the B-state absorption at 350 nm (10-15 ps). Using these considerations, an A'-state rise time of 10-12 ps was found for all solvents.

Once the risetime,  $t_r$ , decay time,  $t_d$ , A'-state absorption

magnitude, A, and long time offset, C, have been determined, the function:

$$A \exp(-t/\tau_d) - (A + C) \exp(-t/\tau_r) + C \quad (1)$$

which represents the A'-state and unrecombined atom contribution to the absorption was subtracted from the data. The curves in Figs. 4 and 7, as well as curves b and a in Figs. 13 and 14 respectively, are representative of the A'-state component which was subtracted. Although the results of the subtraction are somewhat sensitive in the first 10-15 ps to the assumptions made, they seem to be a reasonable, first-order separation of the decay components. Further details of this subtraction are found in Appendix A.

Typical subtraction results at red wavelengths are shown in Fig. 15 for CCl<sub>4</sub> solutions. The overall wavelength dependence of the vibrational absorption is clear, as well as the early time peak which may be due to absorption from the B state. Similar results (not shown) isolate the B-state component of the UV absorption. To quantify the X-state vibrational and B-state predissociation dynamics, the delay from zero time to the maximum and to the point where the absorption has decayed to 1/e of its maximum have been tabulated (Table III). This method of characterization is not unique and caution must be exercised in comparing to other authors.<sup>23</sup>

FIG. 13. Early portion of the transient absorption at 350 and 635 nm of  $I_2$  in  $CCl_4$  (see also Figs. 3 and 5). Fits to the A'-state contribution to the absorption are shown with a) 8 ps, b) 12 ps, and c) 25 ps exponential rise times. The decay time is 2700 ps in all cases (350 nm - 0.4 ps/pt, 635 nm - 1.6 ps/pt).

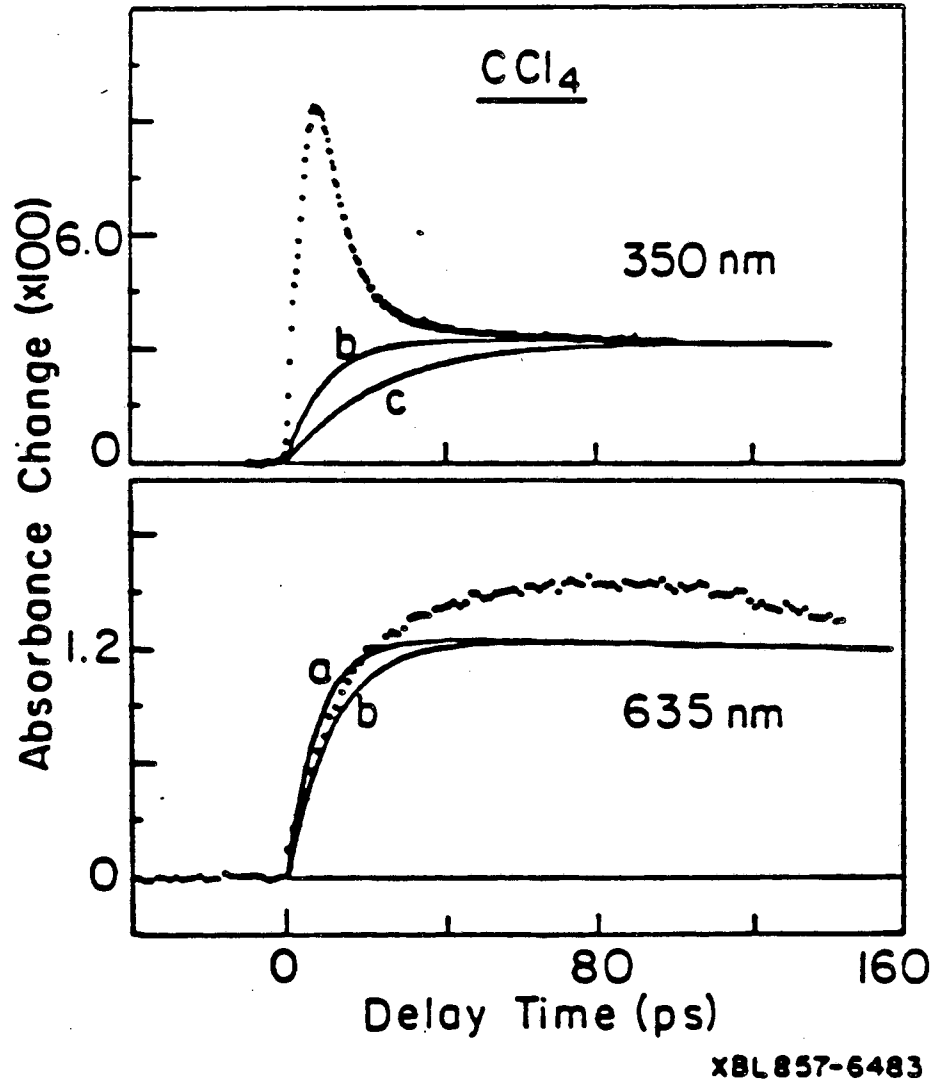
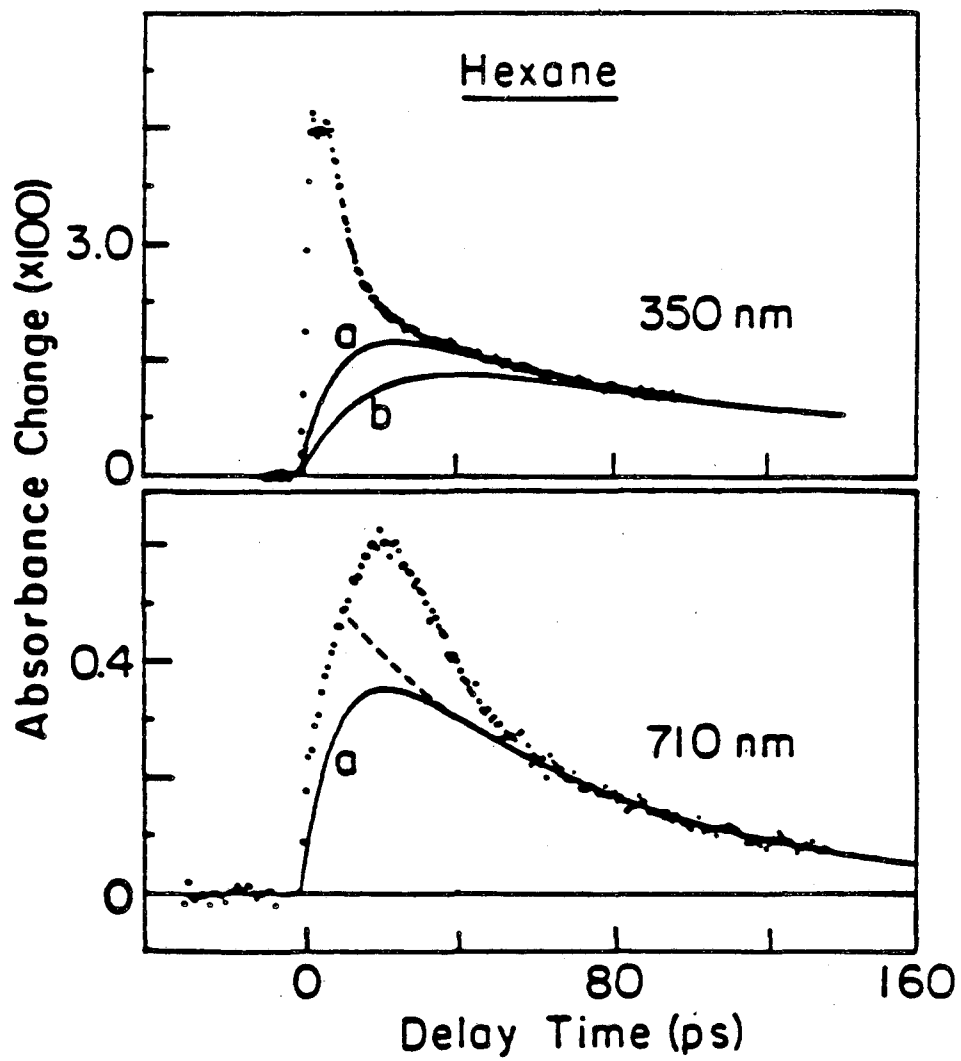


Figure 13

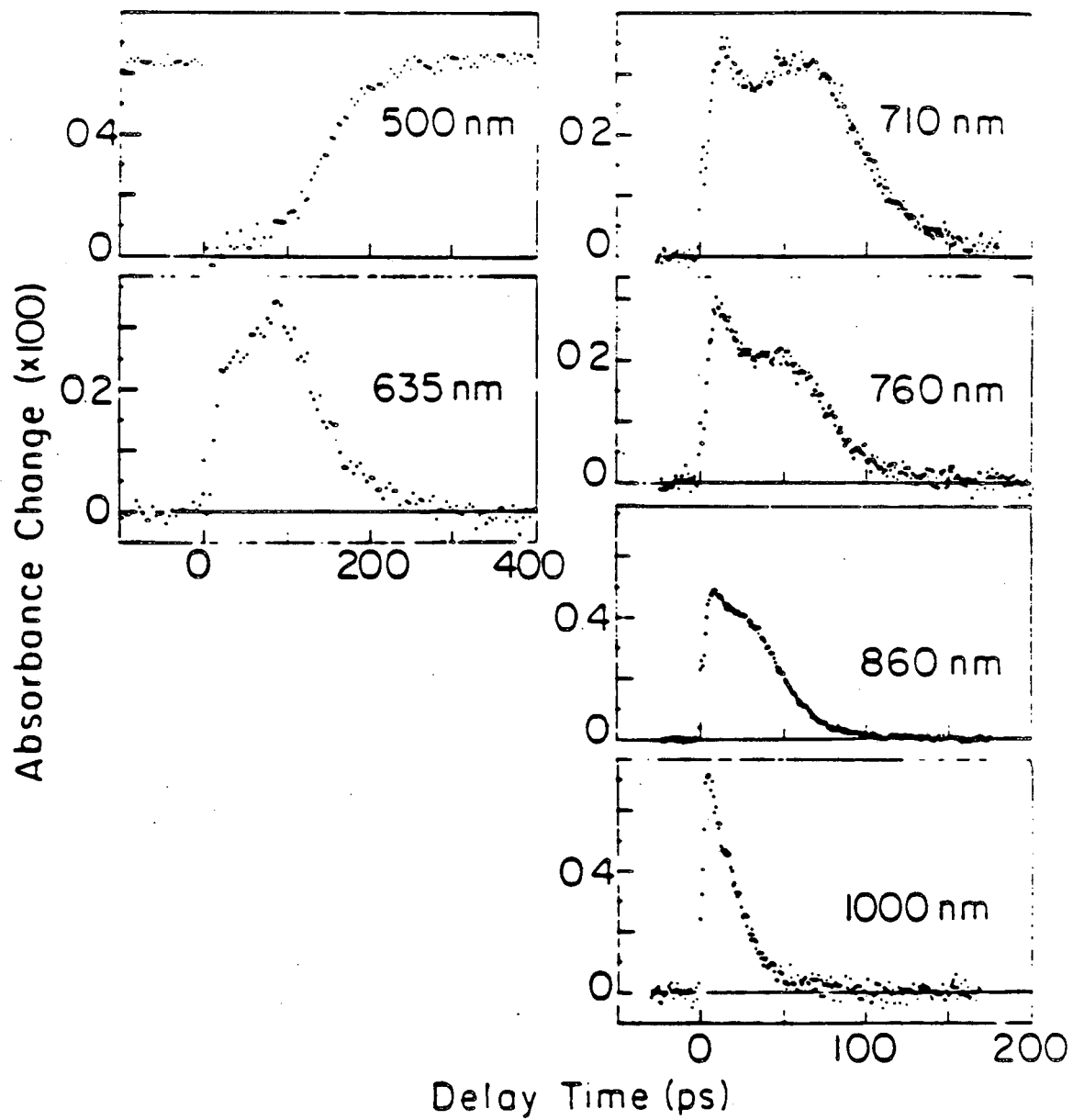
FIG. 14. Early portion of the transient absorption at 350 and 710 nm of  $I_2$  in hexane. Fits to the A'-state contribution to the absorption are shown with a) 10 ps, b) 20 ps exponential rise times. The decay time is 66 ps in both cases. Dotted line shows extension of the 66 ps decay without the effects of the rising edge (350 nm - 0.4 ps/pt, 710 nm - 0.8 ps/pt).



XBL857-6482

Figure 14

FIG. 15. Long wavelength transient absorptions in  $\text{CCl}_4$  after subtraction of the A'-state absorption (500 and 635 nm - 4 ps/pt, other wavelengths - 0.8 ps/pt).



L8L 857-6495

Figure 15

Table III: Absorption Transients with A'-state Contribution Subtracted

i. Delay to 1/e of maximum (ps)

ii. Delay to maximum (ps)

Solvent		Wavelength (nm)									
		X-state dynamics						B-state dynamics			
		1000 <sup>c</sup>	860 <sup>c</sup>	760	710	635	500 <sup>a</sup>	400	370	350	295
CCl <sub>4</sub>	i.	26	54	82	110	149	174	7	14	17	35
	ii.	16 <sup>b</sup>	28	49	62	86	---	2.4	5.6	6.4	10
CHCl <sub>3</sub>	i.	16	39	---	90	148	196	---	---	15	27
	ii.	4	12	---	48	80	---	---	---	6	15
CH <sub>2</sub> Cl <sub>2</sub>	i.	10	22	---	34	52	88	---	---	14	20
	ii.	4	8	---	14	16	---	---	---	5.2	10
Hexane	i.	15	24	---	42	(108) <sup>d</sup>	(116) <sup>d</sup>	5	---	14	21
	ii.	6	12	---	26	(37) <sup>d</sup>	---	1.2	---	2-5	6
Nonane	i.	13	23	---	38	66	(100) <sup>d</sup>	---	---	13	---
	ii.	5	11	---	22	38	---	---	---	4.8	---
Hexadecane	i.	13	23	---	40	58	(84) <sup>d</sup>	---	---	13	---
	ii.	5	10	---	23	34	---	---	---	5.6	---
Cyclohexane	i.	22	38	---	89	(160) <sup>d</sup>	(208) <sup>d</sup>	---	---	14	43
	ii.	7	18	---	46	(67) <sup>d</sup>	---	---	---	4.8	---

a) Transients have a negative absorption change (bleach).

b) Time taken from a shoulder on an early transient.

c) Maximum times may be affected by an unresolved early transient.

d) A'-state component is not resolved. Numbers in parentheses are taken from unsubtracted data.

### E. Summary of the Reaction Model

A model which accounts for the absorption data can now be summarized. Initially, iodine molecules are placed in vibrationally excited levels of the B state (Fig. 1). There is an immediate drop in the absorption at 500 nm, since the B state has a smaller absorption cross section than the ground state at this wavelength (Figs. 9, 10). At the same time there is the immediate appearance of a new absorption band in the UV arising from the B state (Figs. 5, 6). As the B state predissociates and vibrationally relaxes during the next 10-15 ps, the absorption at 500 nm decreases even further, while the B-state UV absorption shifts to longer wavelengths and decays. Once the molecules have dissociated, the solvent dynamics forces them on to one of three routes: they may escape through the solvent to remain unrecombined, they may recombine on an excited state potential and become trapped in the A or A' states, or they may recombine on the X state. Those which have recombined on the X state vibrationally relax. Relaxation proceeds quickly through the upper part of the well, but more slowly near the bottom of the well, so that complete relaxation requires ~100 ps. As the relaxation proceeds, the X-state absorption spectrum shifts from the near IR toward the normal ground state absorption spectrum which peaks at ~520 nm. As the vibrational relaxation is completed, a portion of the ground state absorption at 500 nm recovers in ~100 ps (Figs. 9, 10). A'-state molecules can then be seen by their absorptions in both the red and UV portions of the spectrum (Figs. 3-8). In a time which varies from 60-3000 ps, these states decay back to the X state, causing the decay of A'-state absorptions and a return of the ground state

absorption at 500 nm. Those atoms which escape their original partner recombine on a microsecond time scale, and contribute to the long time ultraviolet absorption and to the long time absorption bleach at 500 nm.

Now that all the absorption features have been considered, it can be seen that the cage recombination of the dissociated atoms must proceed rapidly. As discussed in the last section, if there were a long delay between the predissociation of the B state and recombination, there would be a dip in the UV absorption between the time that the B-state molecules had disappeared and the A'-state molecules had reformed (Figs. 13, 14). In addition, the rapid rise on the absorption curves at 635 and 710 nm implies a rapid filling of the A'-state. Although there may be some contribution to the red rise from an early transient, it seems unlikely that the A'-state rises much slower than the red absorptions and that the additional transient adds on to give such a smooth curve (see Fig. 13). Finally, if molecules were reforming at the top of the X state over a long time period, it would not be possible to see a rapid decay of the population in the higher vibrational states as is observed at 1000 nm (Fig. 15; also 3, 7, 8). Based on all these arguments, a limit of  $<15$  ps can be placed on the time in which the majority of cage recombination occurs. This is nearly an order of magnitude faster than the time suggested by earlier experimental interpretations<sup>2,4,26-28</sup> and by some diffusional theories.<sup>2,53,54</sup>

## IV. COMPARISON TO PREVIOUS RESULTS

Previous observations of the bleach recovery and the red absorptions have disagreed with each other on both the experimental results and their interpretation.<sup>2,4-10,26-28</sup> The results presented here for the A'-state lifetime in chlorinated methanes are in good agreement with the results of Kelley et al.<sup>4</sup> Their initial results did not detect the vibrational component in the red absorptions, probably due to lower time resolution and signal-to-noise. More recently however, our reports of a vibrational component<sup>11,12</sup> have been confirmed in that laboratory.<sup>6</sup> In the alkanes, Kelley et al. reported A'-state lifetimes based on red decay curves in which the vibrational component was not resolved and they mentioned difficulties with signal size in these solvents. Thus, the somewhat shorter times reported here are probably more accurate, since they were derived from high signal-to-noise ultraviolet absorptions free from vibrational components.

The results of Bado et al. in the chlorinated methanes<sup>7,8</sup>, however, are quite different than those reported here. Recent experiments by Abul-Haj and Kelley indicate that these discrepancies are not due to the different excitation wavelengths used.<sup>6</sup> The decay times of the red absorptions, although longer than in the alkanes, are not as long as reported here. Several factors in their experimental technique could have caused this discrepancy. First, very concentrated iodine solutions, near saturation, were used, and we have seen distortions of UV absorption curves attributable to high I<sub>2</sub> concentrations. Abul-Haj and Kelley have also observed quenching of the A' state at high concentration attributed to  $I_2^*(A') + I_2 \rightarrow I_4^*$ .<sup>6</sup> In addition, I<sub>2</sub> dimers

and higher complexes form under these conditions.<sup>4,2</sup> Secondly, the long decay components seen in some solvents would not completely relax in the time between pulses (4 ns) in Bado et al.'s experiments. Finally, the formation of  $I_3^*$  has been observed at high sample concentrations within tens of nanoseconds after photodissociation,<sup>5</sup> and may cause artifacts when high pulse repetition rates are used.

In contrast to the data in chlorinated solvents, the more rapid alkane data of Bado et al.<sup>7,8</sup> are not significantly different from those presented here, if consideration is given to their lower time resolution (~30 ps). The present data resolve two components in the red absorption, one due to vibrationally relaxing X-state molecules, and the other due to A'-state molecules, which would be unresolvable in Bado et al.'s experiment. However, the vibrational component gives the overall curve a strongly wavelength dependent character, which accounts for their interpretation that the red absorption is entirely due to vibrationally relaxing X-state molecules. Although the present interpretation supports the conclusions of Bado et al. on the importance of ground state vibrational relaxation, their data must be viewed with some reservation until the possible roles of  $I_3^*$ ,  $I_4^*$ , and  $I_2$ -dimers in those experiments has been determined.

Chuang et al. reported a slight polarization anisotropy during the rise of the 532 nm bleach in hexadecane, which was attributed to rotational reorientation.<sup>2</sup> We have not reproduced this result. A rotational diffusion model predicts a reorientation time of 2.7 ps/cP for iodine.<sup>55</sup> Using zero-frequency solvent viscosities,<sup>56</sup> the reorientation times should range from 0.8 ps in hexane to 8.2 ps in hexadecane. Motion on the fast end of this range would be unresolved

with the present time resolution, but motion on the slow end should be easily seen. However, the relaxation times predicted in high viscosity solvents such as hexadecane may be too long. The rotation may be sensitive to the high frequency viscosity, which can be expected to be lower than the bulk viscosity in long chain solvents. Thus it seems most likely that the reorientation time for the iodine is only 1-2 ps and that the polarization anisotropy cannot be seen with the current time resolution.

In several papers, attempts have been made to extract the quantum yield of non-geminately recombining atoms by comparing the maximum of the bleach in molecular absorption in the green to the long time loss of absorption.<sup>2,4,26</sup> This procedure assumes that no molecular states are absorbing when the bleach maximum is reached. With the present model for the reaction kinetics, this assumption is not necessarily justified, since at the bleach maximum molecules may be in the A or A' states, may not have completely predissociated, or may have vibrationally relaxed sufficiently to start reabsorbing. In addition, the strong solvent variation of the peak bleach strength reported in one paper are in disagreement with the values found here.<sup>26</sup>

## V. COMPARISON WITH THEORETICAL MODELS

The preceding sections have used the transient absorption data to develop a detailed qualitative picture of the photodissociation/recombination reaction. Using this model, quantitative data can be extracted on the elementary reaction steps. These results can be compared to existing theories for liquid-phase reaction dynamics and may help direct future theoretical developments. First, the experimental upper bound on the geminate recombination time is very useful in assessing the large amount of theoretical work on this process. Second, the time dependent absorption data on the vibrationally relaxing X-state population provides quantitative information on vibrational relaxation through a wide range of vibrational levels. On a rough level, solvent comparisons of the absorption data itself give evidence on the likely pathways for relaxation. For a more precise examination of vibrational relaxation, an approximate derivation of the actual population distribution from the absorption data is developed. Both the solvent dependent relaxation rates and the population distribution are compared with quantitative models of vibrational relaxation in this system. Finally, the two electronic relaxation processes, A'-state relaxation and B-state predissociation, are examined and compared with the few available theoretical models for electronic relaxation.

## A. Recombination Dynamics

The aspect of iodine photodissociation which has received the most theoretical attention is the geminate recombination of dissociated atoms. Two methods have been used: hydrodynamic models which use only a few equations to represent the solvent's influence;<sup>2,27,53,54,57-62</sup> and molecular dynamics simulations, which calculate the exact motions of many solvent molecules.<sup>63-65</sup> It is interesting to ask whether the conclusion that recombination occurs in  $\leq 15$  ps is consistent with theoretical results and whether some theoretical approaches are more useful in understanding this result.

Hydrodynamic models have been popular, partly because of their computational ease and also because it is relatively easy to form simple, physical interpretations of the results. However, there are serious questions, both theoretical and practical, about the application of these equations to the dissociation dynamics of small molecules such as iodine. One objection is that the iodine mass is comparable to that of the solvent, while Langevin and related equations require that the solvent be light compared to the iodine.<sup>66</sup> In addition, the hydrodynamic equations only hold when the solute-solvent force correlation time is much shorter than the correlation time of the solute velocity. This condition is violated during the initial high velocity separation of the dissociating atoms. Even the MTGLE method, which attempts to reduce this problem, must introduce ad hoc "cage breakout" assumptions.<sup>60</sup> Thus hydrodynamic models cannot be applied to the early portions of the dissociation process, but are usually applied to the dynamics after the velocities have thermalized. Thus, the major part of

the recombination process may occur before the hydrodynamic models become applicable.

There are also serious practical problems in using hydrodynamic models to predict the time scale of geminate recombination. The results are very sensitive to the initial conditions, which are determined by the complicated early time dynamics. In addition, the other parameters commonly introduced, such as the solute atom diffusion constant and its distance dependence, the reaction diameter and the intrinsic reaction rate constant, are not independently known or are poorly defined. A wide range of recombination times can be obtained with reasonable parameters; estimates of the 50% recombination time have appeared from 1-150 ps.<sup>53,57</sup> Thus, hydrodynamic models do not provide a reliable prediction of the recombination time scale.

Molecular dynamics simulations of the photodissociation process provide a more promising approach to understanding geminate recombination. Although simulations to date have been limited to a small number of solvent molecules and to short simulation times, useful information has been obtained. The most striking conclusion is that geminate recombination should occur rapidly. Bunker and Jacobsen found that approximately 85% of the atoms recombined within 4 ps in their simulations.<sup>63</sup> In Murrell et al.'s work, 80% of all recombinations occurred in <5 ps over the entire range of densities examined.<sup>64</sup> Similarly, Lipkus et al. found that on the X-state potential, 50% of all recombinations were complete in <1 ps for all densities considered.<sup>65</sup> On the A-state potential, they found that the recombination lifetime was ~10 ps. Thus for recombination on both the X state and the A state, partitioning between free atoms and recombined molecules occurred on a

time scale of  $\leq 10$  ps. In support of these simulations, the quantum yields of escaped atoms as a function of density calculated from these simulations agree well with experimental measurements.<sup>64,65</sup>

These results indicate that the major portion of the recombination occurs on a short enough time scale that the use of hydrodynamic models is suspect. In addition, molecular dynamics, in contrast to hydrodynamics, makes a reasonably definitive prediction that recombination should occur in  $\leq 10$  ps. One reservation to these conclusions is that the role of multiple potential surfaces has not been included in the simulations. A recent model has found that the presence of multiple potential surfaces in iodine may slow the recombination rate by a factor of five, because the atoms may frequently recombine on one of the seven unbound potential surfaces.<sup>67</sup> Even considering the possible slowing effects of multiple surfaces however, the  $> 100$  ps recombination times previously reported<sup>4,26,28</sup> were hard to reconcile with the molecular dynamics results, while the time of  $\leq 15$  ps deduced from the current measurements indicates that the molecular dynamics results are quite reasonable.

## B. Vibrational Relaxation: Classical Analysis and Relaxation Mechanism

Vibrational relaxation in liquids is poorly understood, especially between excited vibrational levels. The time dependent absorption spectrum of vibrationally excited iodine molecules is a rare source of information on this problem. In this section, a simple classical model of absorption from excited vibrational levels is used to compare vibrational relaxation in different solvents. The results cast doubt on the theoretical prediction that vibration-to-vibration (V-V) transfer to the solvent dominates relaxation in the lower portion of the X-state well. It is suggested that vibration-to-rotation (V-R) mechanisms should be included or that vibration-to-translation (V-T) transfer has been underestimated. The following section, Sec. C, discusses corrections to the classical model and performs a more precise analysis of vibrational relaxation in  $\text{CCl}_4$  solution.

In a classical Franck-Condon picture, only vertical transitions between turning points are allowed (Fig. 1). Since the B $\rightarrow$ X transition dominates iodine's visible absorption, the difference potential as a function of X-state vibrational energy can be used to associate an X-state vibrational energy with each absorption wavelength (Fig. 16). Using this classical approximation, Fig. 17 shows the vibrational dynamics derived from the absorption component due to vibrationally excited molecules. In all of the solvents studied, the vibrational relaxation time is substantial; 50-200 ps are required to reach the ground vibrational level. Relaxation through the upper half of the potential, however, is fairly rapid with the peak absorption from levels with  $\sim 6000 \text{ cm}^{-1}$  of vibrational energy appearing in 10-15 ps and decaying

to 1/e of their peak value by 20-30 ps after photodissociation. Among the chlorinated solvents, the absorption at 710 nm ( $\nu=9$ ,  $E_{\text{vib}} \sim 1800 \text{ cm}^{-1}$ ) peaks and decays most slowly in  $\text{CCl}_4$ , somewhat faster in  $\text{CHCl}_3$ , and is almost a factor of three faster in  $\text{CH}_2\text{Cl}_2$ . In the alkane solvents, the three linear alkanes show virtually identical relaxation rates, while cyclohexane is substantially slower.

Nesbitt and Hynes have calculated the relaxation rate for iodine in  $\text{CCl}_4$  using a classical trajectory simulation and assuming uncorrelated binary collisions with the solvent.<sup>3</sup> They found that V-T transfer is relatively rapid in the upper part of the potential, but that relaxation to the ground vibrational level takes more than one nanosecond if the solvent has no internal vibrations. Brooks, Balk, and Adelman reach a similar conclusion using an MTGLE model.<sup>29</sup> When near-resonant vibration-to-vibration (V-V) energy transfer to the  $217 \text{ cm}^{-1}$  mode of  $\text{CCl}_4$  was included, Nesbitt and Hynes showed that the relaxation in lower levels proceeded more rapidly, with ground state recovery in  $\sim 100$  ps. Using molecular dynamics simulations, Bado et al. have also predicted a strong dependence of the vibrational relaxation rate on near-resonant energy transfer to the vibrational modes of the solvent.<sup>31</sup>

The present measurements in chlorinated solvents do not behave according to simple V-V energy transfer predictions. The lowest frequency modes in  $\text{CCl}_4$ ,  $\text{CHCl}_3$ , and  $\text{CH}_2\text{Cl}_2$  are  $217 \text{ cm}^{-1}$ ,  $261 \text{ cm}^{-1}$ , and  $282 \text{ cm}^{-1}$  respectively.<sup>68</sup> The iodine molecular vibrational frequency is  $213 \text{ cm}^{-1}$  in the ground vibrational level and decreases to  $170 \text{ cm}^{-1}$  at  $6000 \text{ cm}^{-1}$  above the ground level.<sup>69</sup> Thus the energy gaps for V-V transfer in the lower half of the well are  $4-47 \text{ cm}^{-1}$  in  $\text{CCl}_4$ ,  $48-91 \text{ cm}^{-1}$  in  $\text{CHCl}_3$ , and  $69-112 \text{ cm}^{-1}$  in  $\text{CH}_2\text{Cl}_2$ . These changes between

the solvents are large compared to the  $20\text{-}25\text{ cm}^{-1}$  resonant transfer width.<sup>70</sup> Thus the V-V relaxation times would be expected to increase in the order  $\text{CH}_2\text{Cl}_2 > \text{CHCl}_3 > \text{CCl}_4$ . A calculation of resonant energy transfer rates<sup>70</sup> using the expression which Nesbitt and Hynes applied to  $\text{CCl}_4$ ,<sup>3</sup> confirms that the expected V-V rates should be 3-4 times slower in  $\text{CHCl}_3$  and 8-10 times slower in  $\text{CH}_2\text{Cl}_2$  through the entire lower half of the X-state potential. In contrast with this prediction, the vibrational relaxation time is actually slowest in  $\text{CCl}_4$ , slightly faster in  $\text{CHCl}_3$  and dramatically faster in  $\text{CH}_2\text{Cl}_2$  (Fig. 17). This suggests either that V-V transfer is not important in any of the chlorinated methane solvents or at least that other mechanisms dominate the rates in  $\text{CHCl}_3$  and  $\text{CH}_2\text{Cl}_2$ .

One alternative mechanism is vibration-to-rotation (V-R) transfer. In the gas phase, V-R transfer is greatly enhanced in small hydrogen containing molecules because of their low moment of inertia.<sup>71</sup> In the present case the effective mass, defined as the lowest moment of inertia divided by the longest moment arm squared, is 142, 60, and 8.5 amu in  $\text{CCl}_4$ ,  $\text{CHCl}_3$ , and  $\text{CH}_2\text{Cl}_2$  respectively.<sup>72,73</sup> Since a smaller effective mass should increase the relaxation rate, the trend in the effective masses matches the trend in relaxation rates. This suggests that transfer of vibrational energy to rotation-like motion of the solvent may be important in these systems.

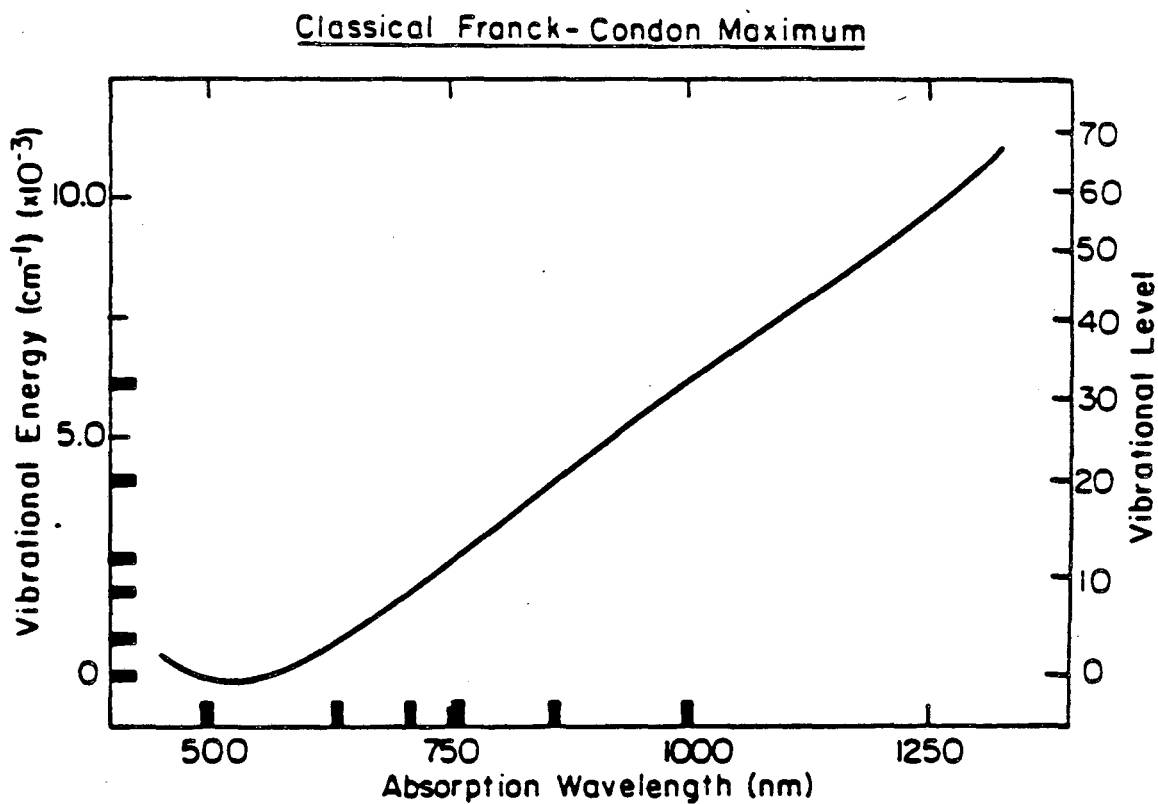
Also, the role of V-T transfer in lower vibrational levels should not be entirely rejected on the basis of theoretical modeling. The ability to predict liquid-phase vibrational relaxation rates, especially between excited vibrational levels, is not well established. In addition, models of V-T transfer are extremely sensitive to the

interaction potentials assumed.<sup>74</sup>

In contrast with the results in chlorinated methane solvents, the vibrational relaxation rate in alkane solvents behaves more nearly as expected for V-V transfer. As Bado et al. have pointed out, the ring structure in cyclohexane substantially reduces the density of low frequency torsional and vibrational modes in comparison with the linear alkanes.<sup>7</sup> With fewer low frequency modes in proximity to the iodine vibrational frequency, the vibrational relaxation in the lower part of the well should be slower in cyclohexane than in normal hexane. This is the observed behavior. In the straight chain alkanes, the relaxation rate does not vary with the length of the alkane chain. This may occur because the number of low frequency modes which can effectively interact with the iodine does not change with chain length, since the number of low frequency modes per unit volume is approximately constant.

The contrasting results for vibrational relaxation rates in these different solvents demonstrate that the role of V-V transfer is not yet understood. Studies in simpler solvents such as Xe and CO<sub>2</sub> should help to clarify the role of V-T and V-R transfer and thereby contribute to an understanding of V-V transfer. The bleach recovery in fluid Xe has been previously observed,<sup>28</sup> but preliminary measurements in this laboratory show different dynamics. More work is necessary to understand vibrational relaxation dynamics in this simple solvent.

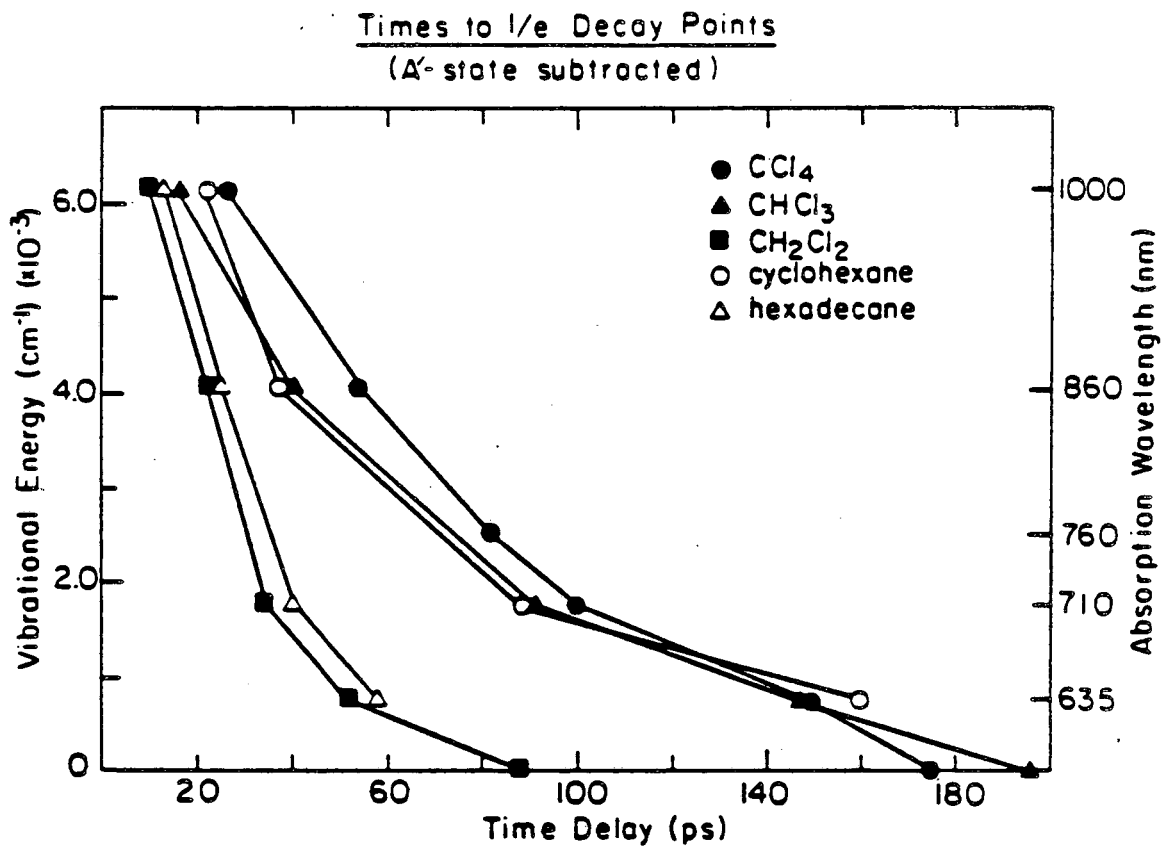
FIG. 16. Vertical difference between the iodine X- and B-state potentials in wavelength vs. X-state vibrational energy. Wavelengths experimentally observed and corresponding vibrational energy levels are marked.



XBL 851-5735

Figure 16

FIG. 17. Time from  $t=0$  to  $1/e$  of the maximum of the absorption due to vibrationally excited X-state molecules. Vibrational energy is associated with absorption wavelength using the difference potential (Fig. 16). ●-CCl<sub>4</sub>, ▲-CHCl<sub>3</sub>, ■-CH<sub>2</sub>Cl<sub>2</sub>, ◐-cyclohexane, △-hexadecane (other n-alkanes are similar).



KBL 89-5737

Figure 17

### C. Vibrational Relaxation: Quantum Spectral Analysis

So far the vibrational absorptions have been discussed assuming that the absorption at a given wavelength can be directly associated with the population at a particular level of vibrational excitation. This assumption is based on a crude, classical Franck-Condon model and oversimplifies the true quantum mechanical spectrum. In order to assess the importance of quantum effects, a calculation of the absorption strength for a given wavelength versus the amount of vibrational energy in the X state was performed. Franck-Condon factors and R-centroids were calculated for the B $\rightarrow$ X,  $^1\Pi_u \rightarrow$ X, and A $\rightarrow$ X transitions. A continuous spectrum was obtained for each X-state vibrational level by assuming that each transition was broadened to a 200 cm<sup>-1</sup> gaussian line in the liquid phase. Broadening of this magnitude is consistent with the absence of vibrational structure in the visible absorption spectrum. The final results are only weakly sensitive to the extent or the form of the broadening function. The strong R-centroid dependence of the B $\rightarrow$ X transition moment was included.<sup>75</sup> Further details on the calculation are given in Appendix B. Figure 18 shows examples of the results.

The quantum mechanical transition strengths have several features in common at all wavelengths. The transition strengths all have a strong peak which lies slightly higher in vibrational energy than the classical prediction, because the main peak of the vibrational wavefunction lies inside the classical turning point. On the high vibrational energy side of this peak there is a long, slowly decaying tail, due to overlap of the oscillatory portions of the wavefunctions. Because of this tail, the absorption at a given wavelength should start

to rise before the population has relaxed as far as the point of classical absorption. By the same reasoning, the absorption bleach will begin to recover before the population reaches the bottom of the potential well. In contrast, the transition strength drops sharply on the low vibrational energy side of the main peak, due to the rapid drop in the wavefunction outside the classically allowed region. This implies that the absorption decay at each wavelength is a reasonably accurate indication of the population which has relaxed below the classical absorption point. Finally, the width of the main peak in the transition strengths broadens as the wavelength of the transition increases.

Incorporating the more accurate quantum transition strengths into the analysis of the vibrational absorptions can be done as follows. The spectrum at each time can be represented as:

$$A(\lambda, t) = \int_0^{\infty} dE S(\lambda, E) P(E, t) \quad (2)$$

where  $A(\lambda, t)$  is the absorption data at a given wavelength,  $\lambda$ , and delay time,  $t$ ;  $P(E, t)$  is the population as a function of vibrational energy,  $E$ ; and  $S(\lambda, E)$  is the transition strength. Exactly inverting this expression to find  $P$  from  $S$  and  $A$  is difficult when  $P$  and  $S$  are arbitrary functions and  $A$  is only sampled at a few values of  $\lambda$ . However, consideration of the actual characteristics of  $P$  and  $S$  allows an approximate inversion of this formula which includes the major corrections from the quantum calculation.

The energy scale is first broken into segments, each of which isolates the transition strength peak for one wavelength. In  $\text{CCl}_4$

enough wavelengths were measured that these regions cover the energy region from 0-8000  $\text{cm}^{-1}$ . Next, at each probe wavelength the function  $S$  is approximated by a function  $S'$  which is constant over each energy region (Fig. 18). If the analysis is restricted to times when all the population has relaxed below 8000  $\text{cm}^{-1}$ ,  $S'$  can be set equal to zero above 8000  $\text{cm}^{-1}$ . Equation 2 now gives

$$(3) \quad A(\lambda, t) \approx \sum_{j=1}^n S'_j(\lambda) \int_{E_{j-1}}^{E_j} dE P(E, t)$$

or

$$A_\lambda(t) \approx \sum_{j=1}^n S'_{\lambda j} P_j(t) \quad (4)$$

where  $S'_{\lambda j}$  is the value of  $S'$  at wavelength  $\lambda$  in energy region  $j$ ,  $E_j$  is the upper edge of energy region  $j$  ( $E_0=0$ ), and:

$$P_j(t) = \int_{E_{j-1}}^{E_j} dE P(E, t)$$

If the energy regions are well chosen,  $S'$  duplicates the important features of  $S$ , and this approximation can be expected to be a good one. If at each time  $A$  is known at  $n$  values of  $\lambda$ , and  $n$  energy regions are selected, the problem reduces to a set of  $n$  equations in  $n$  variables, which can be solved by standard matrix techniques (Eq. 4). Several factors which are important in obtaining a good inversion are discussed in detail in Appendix C.

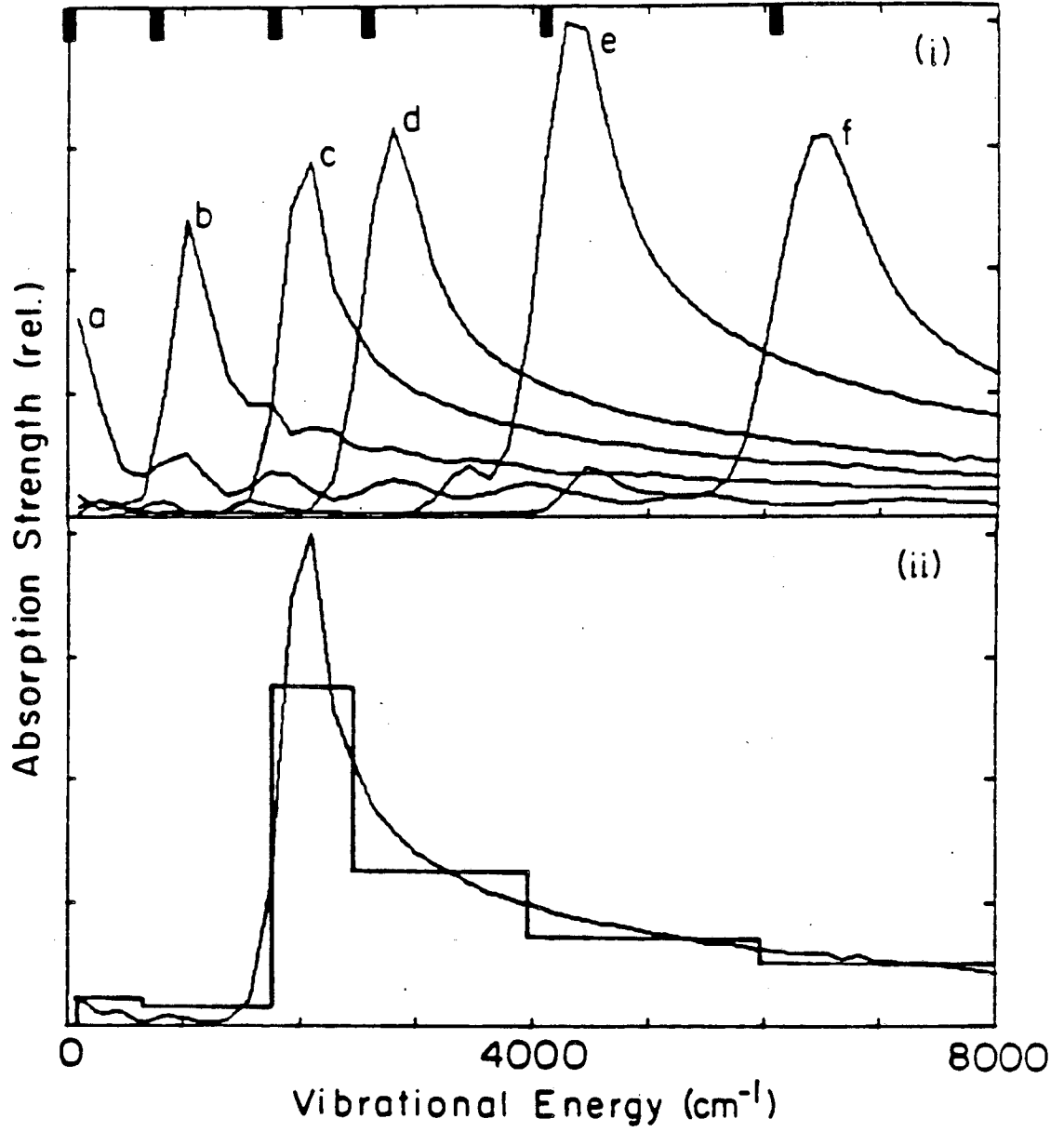
Figure 19 shows the results of applying this procedure to the  $\text{CCl}_4$  data. The average population density for each energy region is plotted at the center of that region. Prior to 50 ps, reliable results cannot be obtained, partly because some of the population has not relaxed below  $8000 \text{ cm}^{-1}$ , and partly because of interference from other early time absorptions. From 50-200 ps, the total population remains constant to within 10% even though there is no explicit constraint on the population from one time point to the next. It is encouraging that this simple inversion produces reasonable results and particularly that it conserves total population. Its success indicates that the assignment of the early absorption features to vibrational relaxation in the X state is quantitatively consistent with the absorption data at all wavelengths.

The population distribution in time resulting from this calculation (Fig. 19) can be directly compared to the results of Nesbitt and Hynes's binary collision simulation (Ref. 3, Fig. 10). The experimental distribution at 50 ps has relaxed further than the calculated distribution. This indicates that relaxation is faster than predicted through the upper part of the well. On the other hand, the experimental distribution still has a significant unrelaxed tail at 150 ps when the model system is completely relaxed. Thus relaxation of the last  $\sim 2000 \text{ cm}^{-1}$  proceeds more slowly than predicted. These discrepancies indicate a weaker dependence of relaxation rate on vibrational level and less of a "bottleneck" effect than that found in Nesbitt and Hynes's model. This bottleneck arose because V-T transfer was predicted to slow below  $\nu \sim 60$ , while V-V transfer was not predicted to become efficient until below  $\nu \sim 40$  (Ref. 3, Fig. 9). The disagreement of the calculated and experimental distributions suggests that the relative roles of V-T and

V-V transfer at various levels of vibrational energy are not yet understood.

In order to assess the importance of different quantum corrections to the transition strengths, the population distribution at 50 ps was also calculated with the classical model and with a model incorporating the quantum mechanical peak shifts and broadening, but without the high energy tail (Fig. 20). Although the classical model correctly gives the general features of the population distribution, a more sophisticated treatment is needed for even semi-quantitatively correct results. In particular, ignoring the high vibrational energy tail in the transition strengths causes an overestimation of the population at lower vibrational levels.

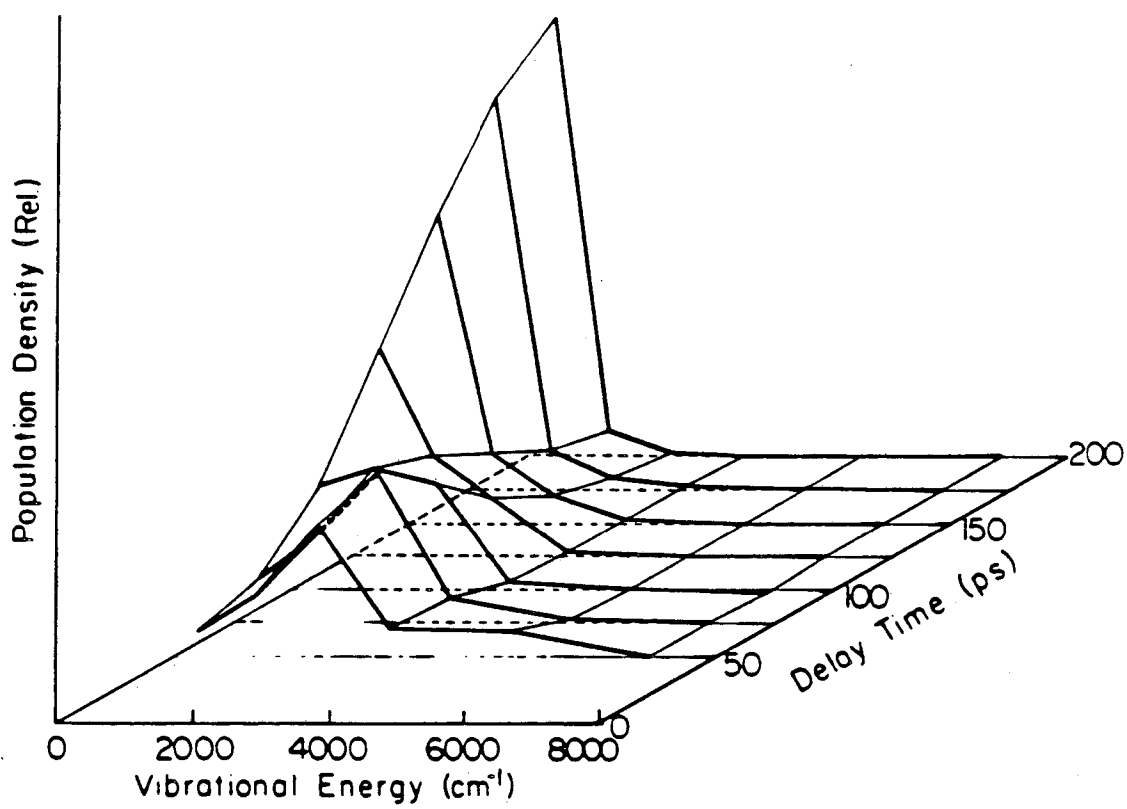
FIG. 18. i. Quantum mechanical calculation of the relative absorption strength from the iodine X-state vs. the amount of vibrational excitation: a) 500 nm, b) 635 nm, c) 710 nm, d) 760 nm, e) 860 nm, f) 1000 nm. Points where absorption is predicted by the classical model (Fig. 16) are marked on top. ii. Absorption strength at 710 nm, S, and its approximation, S'. The same intervals on the vibrational energy axis are used in approximating all the curves in (i).



XBL 857-6492

Figure 18

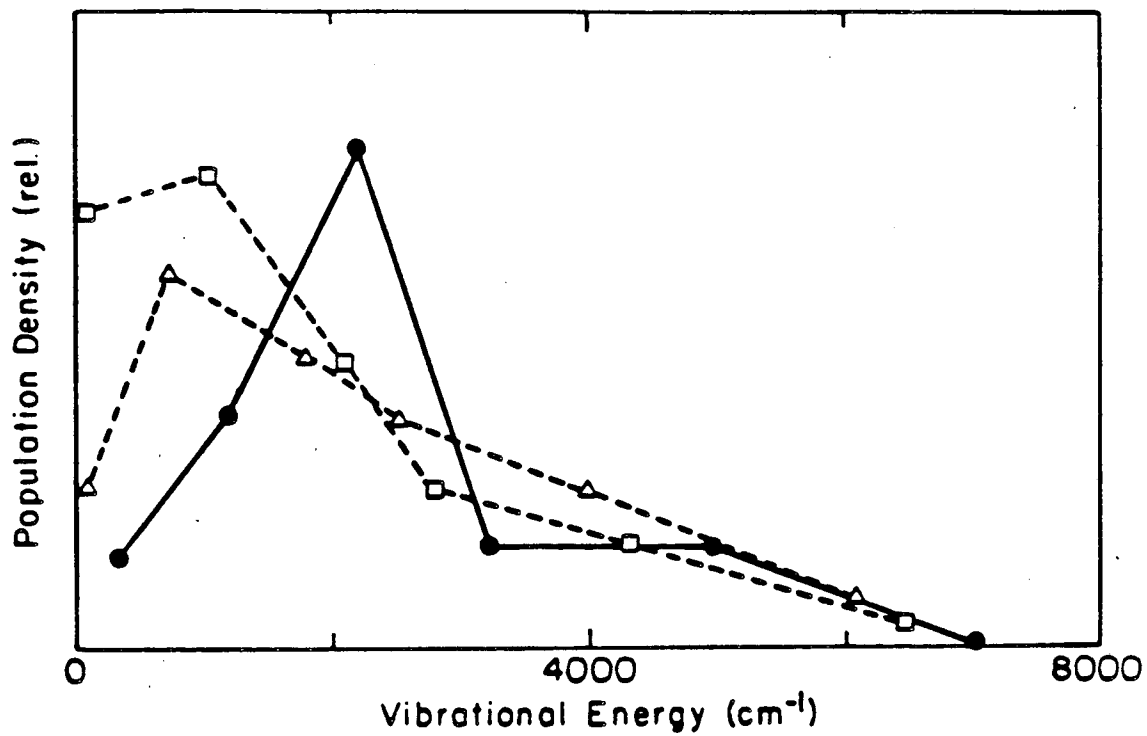
FIG. 19. The distribution of the vibrationally excited population in the iodine X-state at several delay times in  $\text{CCl}_4$  solution. The average population density over each energy interval (Fig. 18) has been plotted at the center of that interval.



XBL 858-3293

Figure 19

FIG. 20. Effect of different corrections to the classical model for absorption strengths on the derived population distribution in the iodine X state at 50 ps in  $\text{CCl}_4$  solution.  $\square$ -classical model,  $\triangle$ -corrected for the change in peak widths and positions, but not including the high energy tail,  $\bullet$ -full quantum mechanical treatment.



XBL 857-6480

Figure 20

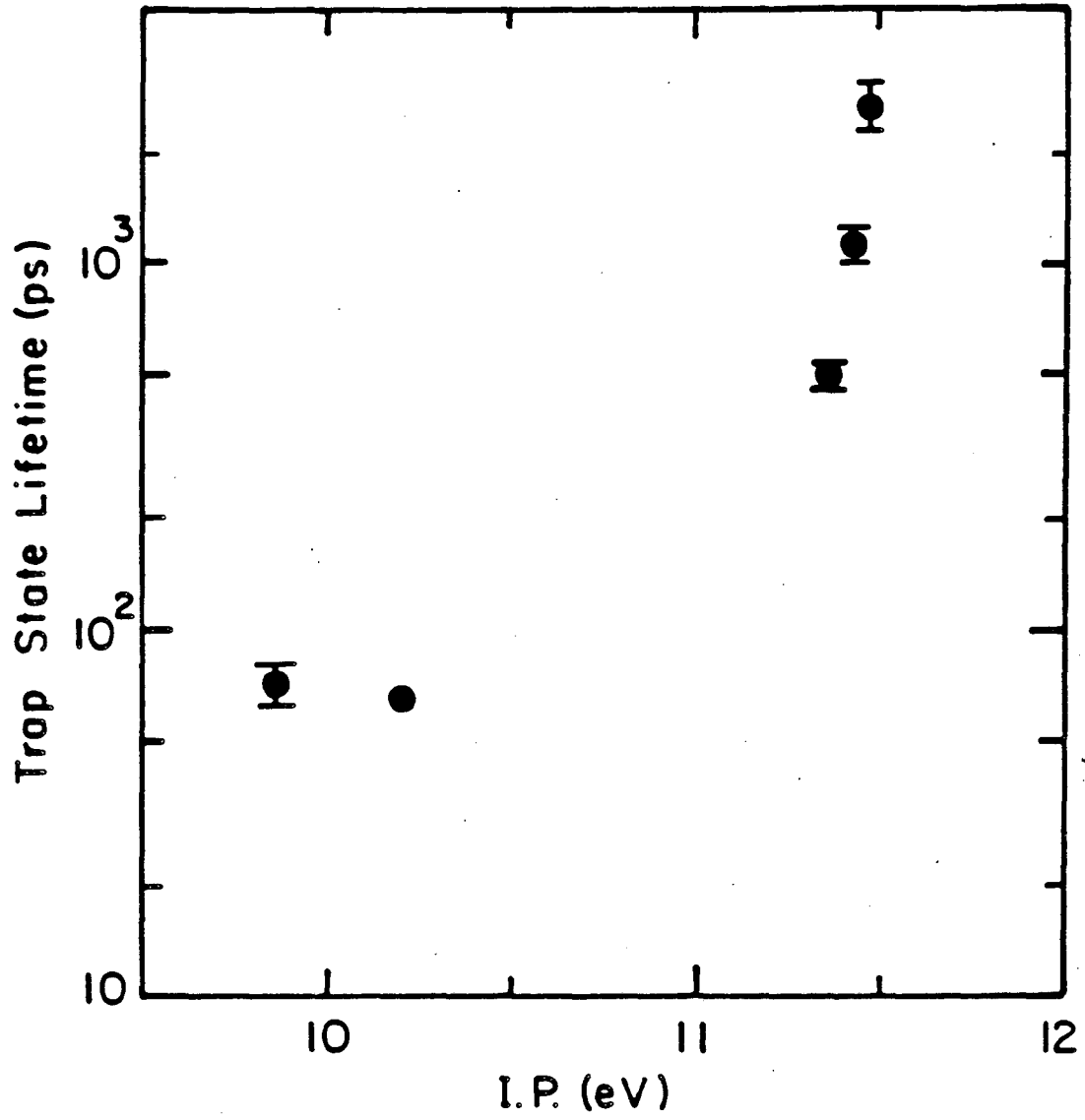
#### D. Lifetime of the A' State

The lifetime of the A' state varies dramatically in the solvents studied, from 500-2700 ps in chlorinated solvents to 65 ps in alkane solvents. In models of the A'-state lifetime, it has been generally assumed that the molecule must be activated high in the well to a region near the curve crossing with the X state in order to relax. Thus, changes in the A'-state lifetime may result from either changes in the height of the crossing point or from changes in activation rate. Kelley et al. proposed that the A'-state well depth varies as a result of changes in the molecular solvation energy as compared to the atomic solvation energy.<sup>4</sup> They further proposed that the solvation energy is largely due to charge-transfer interactions, and that the well depth can be related to the ionization potential of the solvent. As a result the A'-state lifetime should be related to the ionization potential of the solvent, and in fact the A'-state lifetimes are roughly ordered according to the ionization potentials. One difficulty with this proposal is that although charge-transfer transition wavelengths have been related to the solvent ionization potential, this relationship is based on the energy of the upper ion-pair state. The connection between solvent ionization potential and the lower-state solvation energy is not clear.<sup>35</sup> It is even less clear how the difference between molecular and atomic solvation energies is affected by the solvent's ionization potential. As a test of the model it can be assumed that the activation energy (well depth) depends linearly on the solvent ionization potential and that the rate follows an Arrhenius law. With these assumptions, the log of the lifetimes should be linearly related to the solvent

ionization potential. Figure 21 shows that the correlation is poor, so that the solvent ionization potential does not appear to be the most important parameter in determining the A'-state lifetime.

Dawes and Sceats<sup>62</sup> have proposed that the electronic state curve crossing rate and the diffusive motion up the well to the crossing region are solvent dependent. Using a simple model for both the diffusive motion and the curve crossing, they conclude that the rate is transport limited. Thus the lifetime should decrease in lower viscosity solvents. The model predicts A'-state lifetimes which are much longer than the experimental results. If it is assumed that our assignment is incorrect and that the A state is actually being observed, the predicted timescale is more reasonable (Fig. 22). Still, the simulation results do not fit well. An approximate, analytical model predicts the general trend for the chlorinated solvents, but this agreement is hard to interpret, since the analytical model is justified based on its ability to match the simulation results. An even larger problem is the fact that the lifetimes in the alkane solutions are all approximately the same, even though the viscosity changes by a factor of ten. Dawes and Sceats have proposed that the frequency dependence of the viscosity may be important and that the high frequency viscosity would be similar in all the alkanes.<sup>62</sup> In any case it is clear that the zero frequency shear viscosity does not correlate with the A'-state lifetime. At this stage, it appears that none of the essential features which determine the A'-state lifetime are well understood.

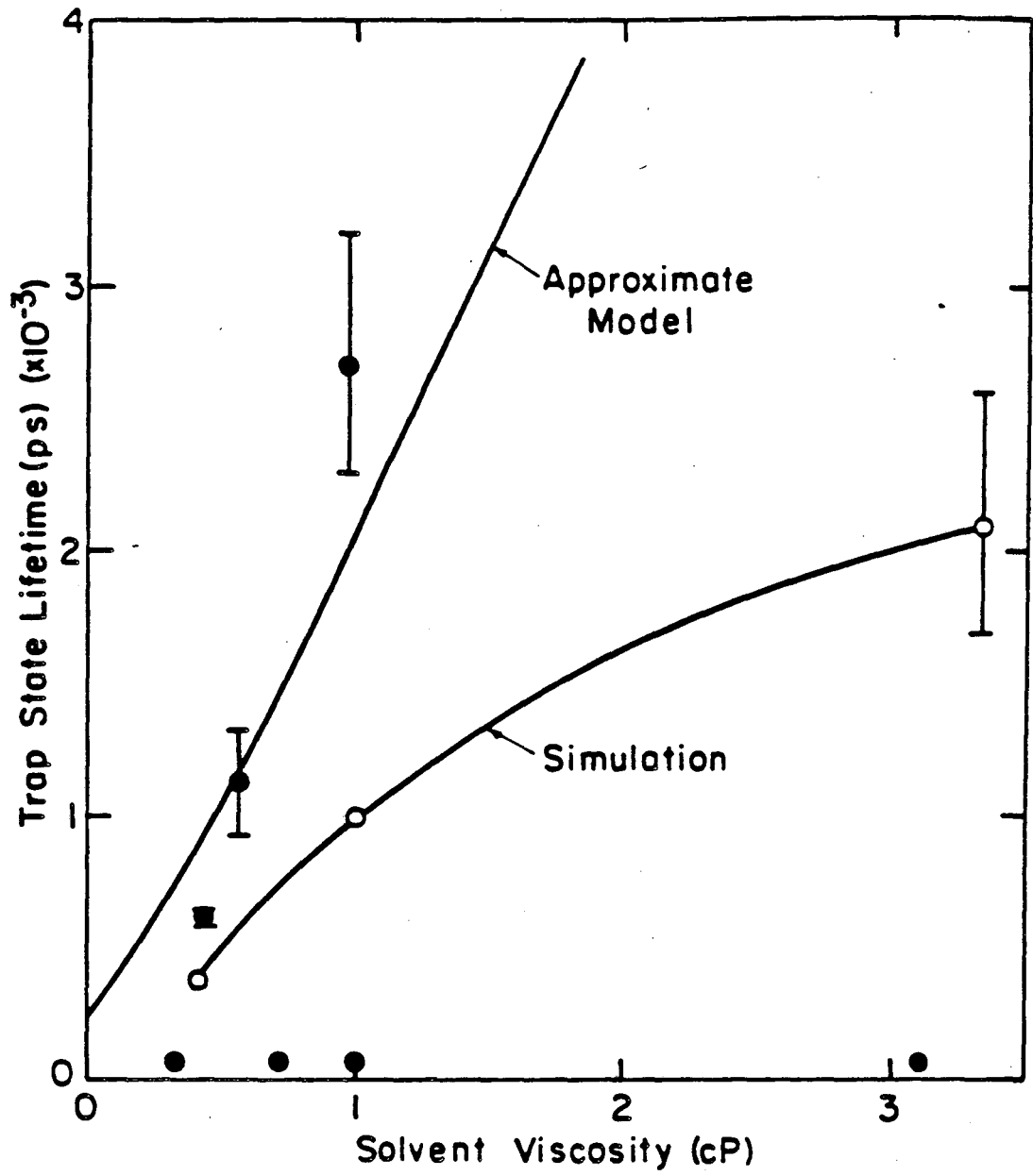
FIG. 21. Measured iodine A'-state lifetime as a function of the ionization potential of the solvent. The nearly identical values of the n-alkanes have been averaged to give a single point.



XBL 857-6491

Figure 21

FIG. 22. Lifetime of the trapped electronic state compared to the viscosity of the solvent. Also plotted are the results of Langevin simulations of the A-state relaxation and of an analytical model based on those simulations (Ref. 62). If the trap state is actually the A'-state, as proposed in the text, the models predict much longer lifetimes. ● - experimental points, ○ - simulation results.



XBL 857-6481

Figure 22

## E. Predissociation

The early component of the UV absorptions (Fig. 5a, 6a) is due to absorption from the excited B state. The absorption decay at any given wavelength is due to both vibrational relaxation and predissociation. The situation is complicated by the fact that the predissociation rate is likely to depend on the vibrational level.<sup>76,77</sup> Thus it is not possible to accurately separate these two contributions to the decay. However, a rough timescale of 10-15 ps for predissociation can be obtained. There are no dramatic changes in different solvents.

There is virtually no theoretical work on liquid-phase predissociation to compare to, but comparisons can be made to gas-phase measurements.<sup>76-78</sup> For the vibrational levels initially excited in this experiment, the probability of predissociation per gas-phase kinetic collision is 0.8-0.2 for Xe, which is similar in size and mass to CCl<sub>4</sub>.<sup>76</sup> By comparison, the liquid-phase lifetime of ~10 ps, corresponding to ~100 "collisions",<sup>3</sup> is surprisingly long. The observed lifetime may be explained by a large drop in the predissociation probability for vibrational levels below v-7.<sup>76</sup> It is clear that further work is necessary to understand this phenomenon.

## VI. SUMMARY AND CONCLUSIONS

A detailed picture of the steps involved in a simple dissociation/recombination reaction has been developed from picosecond absorption studies extending from the near infrared into the UV spectral region. The data present convincing evidence that the geminate recombination of dissociated atoms is fast ( $<15$  ps). This conclusion is consistent with molecular dynamics simulations. In contrast it is argued that hydrodynamic approaches to geminate recombination involve questionable theoretical assumptions and produce few useful predictions. Many theories have predicted a long time tail in the recombination probability. However, the current model is able to explain all the available absorption data assuming that all the recombination is rapid. While a long time tail cannot be rigorously excluded, there is no evidence to suggest that if one exists, it accounts for more than a minor fraction of the total recombination.

Vibrational and electronic relaxation of the recombined molecule have been found to be much slower than the initial recombination. The evolution of the vibrationally excited population distribution has been approximated using realistic, quantum mechanical spectra of vibrationally excited molecules. Neither the population distribution nor comparisons of vibrational relaxation rates in different solvents provide evidence for resonant energy transfer to solvent vibrational modes in chlorinated solvents, in contrast with predictions. On the other hand, resonant vibrational energy transfer may be more important in alkane solvents. In addition the few models available to describe

A'-state electronic relaxation are unable to explain the 40-fold range of lifetimes observed in different solvents. No theories have yet directly addressed the B-state electronic relaxation rate and its relative lack of solvent dependence.

In conclusion, this study has presented a detailed qualitative picture of iodine photodissociation and has made significant steps toward a quantitative understanding of the reaction processes. However, the study of molecular dissociation and recombination in liquids is still a fertile area for further theoretical and experimental work. Large scale molecular dynamics simulations should help to give a better understanding of the solvent's role in geminate recombination. Basic developments are required in the theory of solvent-induced predissociation and electronic curve crossing. The development of these theories will benefit from new temperature and density dependent studies on iodine photodissociation. Experimental work is also needed in simple mono- and di-atomic solvents to understand the relative roles of V-V and V-T vibrational energy transfer. In addition, experiments with excitation to the directly dissociative A state should allow direct observation of the geminate recombination event. It may be hoped that the deeper understanding of the iodine photodissociation reaction which will emerge from further work will provide a basis for a general understanding of liquid-phase chemical dynamics.

## APPENDIX A. SUBTRACTION OF THE A'-STATE ABSORPTION

Since the recombination dynamics is completed rapidly after predissociation (Sec. III E), the B-state decay time, and the A'-state and escaped-atom rise times are very similar. Therefore, the offsets at UV and green wavelengths, both due to atoms which do not recombine, were assumed to form with the same rise time as the A'-state (see Eq. 1). In addition, in order to quantitatively assign the X-state vibrational dynamics based on the green and red transient curves, it was helpful to remove the B-state absorption which occurs at early time at 500 nm. Assuming that the decay time of the B-state absorption at 500 nm is set equal to the A'-state rise time, the B-state absorption was represented by  $B \exp(-t/t_r)$ . This term was subtracted from the 500 nm bleach curves, along with Eq. 1. The magnitude, B, is somewhat arbitrary, but has only a small effect on the subtracted data for times longer than 20 ps, where the vibrational analysis is focussed.

## APPENDIX B. TRANSITION STRENGTH CALCULATIONS

The rotationless potential curves<sup>24,45,69,79</sup> and transition moments<sup>32,75</sup> are well known for the iodine X, B, A, and  $^1\Pi_u$  states. Evidence suggests that the potentials are not strongly perturbed in the liquid.<sup>80</sup> Analytical approximations to these curves were made as follows:

$$V_X(R) = 14600 [ 1 - e^{-1.85(R-2.67)} ]^2$$

$$V_B(R) = 5000 [ 1 - e^{-1.70(R-3.03)} ]^2$$

$$|\mu_e|_{X \rightarrow B}(\bar{R}) = \begin{cases} 1.62 \bar{R} - 3.51 ; & 2.5 < \bar{R} < 3.1 \text{ \AA} \\ -1.745 \bar{R} + 6.91 ; & 3.1 < \bar{R} < 3.3 \text{ \AA} \\ -0.781 \bar{R} + 3.74 ; & 3.3 < \bar{R} < 4.6 \text{ \AA} \end{cases}$$

$$V_A(R) = \begin{cases} -3241 + 2.958 \times 10^8 / R^{11} & ; R < 2.7873 \text{ \AA} \\ 1100 [ 1 - e^{-2.95(R-3.056)} ]^2 & ; R > 2.7873 \text{ \AA} \end{cases}$$

$$|\mu_e|_{X \rightarrow A} = 0.202 \text{ D}$$

$$V_{^1\Pi_u}(R) = \begin{cases} \text{as in Ref. 24} & ; R > 4.200 \text{ \AA} \\ -180 & ; R > 4.200 \text{ \AA} \end{cases}$$

$$|\mu_e|_{X \rightarrow ^1\Pi_u} = 0.369 \text{ D}$$

where R is measured in Å, energy is in  $\text{cm}^{-1}$ , and  $\bar{R}$  is the R-centroid.

The X-state Morse parameters were chosen to optimize the fit to the outer limb of the RKR potential, since this is most important to the Franck-Condon calculations. The use of approximate potentials will not reproduce the state-to-state interference effects,<sup>81</sup> but these effects should be largely averaged out in the liquid. The bound Morse wavefunctions were calculated analytically.<sup>82</sup> The wavefunctions were calculated for  $v=0-50$  in the X state and for all bound levels in the upper states. For the unbound states, wavefunctions were calculated every  $50-60 \text{ cm}^{-1}$  by integrating Schrodinger's equation from  $2.2 \text{ \AA}$  outward. Integration was carried out until the wavefunction reached its asymptotic behavior, so proper normalization could be performed.<sup>83</sup> Franck-Condon and R-centroid integrations were done from  $2.2-3.74 \text{ \AA}$  at a  $.003 \text{ \AA}$  spacing.

## APPENDIX C. VIBRATIONAL POPULATION DISTRIBUTION CALCULATION

The data inversion to find the population distribution requires several provisions to obtain reasonable results. First, to get the total absorption at a given wavelength, the absorption of the ground state at that wavelength must be added to the absorption change measured by the data. Thus one number must be chosen which represents the total population relaxing in the X state, but which is the same for all wavelengths and all times. The total population should be such that the total absorption at 500 nm is near the maximum bleach observed. Furthermore, none of the populations calculated should be negative, nor should the lowest level populate before the higher levels. These conditions restrict the value of the population to a narrow range. Variation of the population within this range causes small variations in the population in the lowest energy region and negligible changes elsewhere.

For the data obtained using 12 ps A-state risetime, all the conditions on the population value cannot be simultaneously satisfied. This arises because the subtracted bleach curve has a nearly flat early portion, whereas a partial early recovery is expected (see text). If a risetime of 17 ps is used, a qualitatively correct bleach curve is obtained and a realistic population distribution is found. A risetime of 17 ps was used for all the data used to generate figure 19. It is not surprising that this is a different risetime than that cited earlier. Since the exponential rise assumed for the A state is probably not the correct functional form, slightly different exponential risetimes will give the best results in different situations.

Finally, the function  $S'$  must be chosen to give the proper limit at long times. For most of the energy regions,  $S'$  is set equal to the average value of  $S$  over that region. For the lowest region, however, the value is set to the value at the bottom of the well. This insures that at long times, when the population is all at the very bottom of the well, the correct absorption spectrum will be predicted.

References

1. E. Rabinowitch and W. C. Wood, *Trans. Faraday Soc.* 32, 547 (1936).
2. T. J. Chuang, G. W. Hoffman and K. B. Eisenthal, *Chem. Phys. Lett.* 25, 201 (1974).
3. D. J. Nesbitt and J. T. Hynes, *J. Chem. Phys.* 77, 2130 (1982).
4. D. F. Kelley, N. A. Abul-Haj, D.-J. Jang, *J. Chem. Phys.* 80, 4105 (1984).
5. D. F. Kelley and N. A. Abul-Haj, in Ultrafast Phenomena IV, edited by D. H. Auston and K. B. Eisenthal, *Springer Ser. Chem. Phys.* 38 (Springer, New York, 1984), p. 292.
6. N. A. Abul-Haj and D. F. Kelley, *Proc. Soc. Photo-Optical Instrum. Engin.* (in press).
7. P. Bado, C. Dupuy, D. Magde, K. R. Wilson, and M. M. Malley, *J. Chem. Phys.* 80, 5531 (1984).
8. P. Bado and K. R. Wilson, *J. Phys. Chem.* 88, 655 (1984).
9. P. Bado, P. H. Berens, J. P. Bergsma, S. B. Wilson, K. R. Wilson, and E.J. Heller, in Picosecond Phenomena III, edited by K. B. Eisenthal, R. M. Hochstrasser, W. Kaiser, A. Laubereau, *Springer Ser. Chem. Phys.* 23 (Springer, New York, 1982), p. 260.
10. P. Bado, C. G. Dupuy, J. P. Bergsma, and K. R. Wilson, in Ultrafast Phenomena IV, edited by D. H. Auston and K. B. Eisenthal, *Springer Ser. Chem. Phys.* 38 (Springer, New York, 1984), p. 296.
11. M. Berg, A. L. Harris, and C. B. Harris, *Phys. Rev. Lett.* 54, 951 (1985).
12. M. Berg, A. L. Harris, J. K. Brown and C. B. Harris, in Ultrafast Phenomena IV, edited by D. H. Auston and K. B. Eisenthal, *Springer Ser. Chem. Phys.* 38 (Springer, New York, 1984), p. 300.
13. A. L. Harris, M. Berg, and C. B. Harris, submitted for publication to *The Journal of Chemical Physics*, 1985.
14. J. Zimmerman and R. M. Noyes, *J. Chem. Phys.* 18, 658 (1950).
15. F. W. Lampe and R. M. Noyes, *J. Am. Chem. Soc.* 76, 2140 (1954).
16. D. Booth and R. M. Noyes, *J. Am. Chem. Soc.* 82, 1868 (1960).
17. L. F. Meadows and R. M. Noyes, *J. Am. Chem. Soc.* 82, 1872 (1960).
18. R. M. Noyes, *Z. Electrochem.* 64, 153 (1960).

19. R M. Noyes, *Prog. React. Kinetics* 1, 129 (1961).
20. K. Luther and J. Troe, *Chem. Phys. Lett.* 24, 85 (1974).
21. K. Luther, J. Schroeder, J. Troe, and U. Unterberg, *J. Phys. Chem.* 84, 3072 (1980).
22. B. Otto, J. Schroeder and J. Troe, *J. Chem. Phys.* 81, 202 (1984).
23. H. Hippler, V. Schubert, and J. Troe, *J. Chem. Phys.* 81, 3931 (1984).
24. J. Tellinghuisen, *J. Chem. Phys.* 82, 4012 (1985).
25. Ref. 2 reported time parameters from a free flight model, Refs. 7 and 8 characterized times by the FWHM of the decay curves, and Ref. 12 used exponential fits to the decaying edge of the absorption.
26. C. A. Langhoff, B. Moore and M. DeMeuse, *J. Am. Chem. Soc.* 104, 3576 (1982).
27. C. A. Langhoff, B. Moore, and M. DeMeuse, *J. Chem. Phys.* 78, 1191 (1983).
28. D. F. Kelley and P. M. Rentzepis, *Chem. Phys. Lett.* 85, 85 (1982).
29. C. L. Brooks, III, M. W. Balk, and S. A. Adelman, *J. Chem. Phys.* 79, 784 (1983).
30. P. Bado, P. H. Berens, and K. R. Wilson, in Picosecond Lasers and Applications, edited by L. S. Goldberg, *Proc. Soc. Photo-Optical Instrum. Engin.* 322, p. 230 (1982).
31. P. Bado, P. H. Berens, J. P. Bergsma, M. H. Coladonato, C. G. Dupuy, P. M. Edelsten, J. D. Kahn, K. R. Wilson, and D. R. Fredkin, in Photochemistry and Photobiology: Proceedings of the International Conference, A. H. Zewail, ed. (Harwood, New York, 1983).
32. J. Tellinghuisen, *J. Chem. Phys.* 76, 4736 (1982).
33. J. Tellinghuisen, *J. Quant. Spectrosc. Radiat. Transfer* 19, 149 (1978).
34. M. Berg, A. L. Harris, J. K. Brown, and C. B. Harris, *Opt. Lett.* 9, 50 (1984).
35. For a review see M. Tamres and R. L. Strong, in Molecular Association, edited by R. Foster, (Academic Press, New York, 1979) Vol. 2, Chap. 5.
36. L. E. Orgel and R. S. Mulliken, *J. Am. Chem. Soc.* 79, 4839 (1957).
37. D. F. Evans, *J. Chem. Phys.* 23, 1424 (1955).

38. H. A. Benesi and J. H. Hildebrand, *J. Am. Chem. Soc.* 71, 2703 (1949).
39. S. R. Logan, R. Bonneau, J. Jousset-Dubien, and P. Fournier de Violet, *J. Chem. Soc., Faraday I* 71, 2148 (1975).
40. Atom/solvent contact charge-transfer absorptions are observed in the UV (Sec. IIIA). No evidence correlating absorption strengths from molecular states with the solvent's ionization potential was observed, indicating that molecule/solvent contact charge-transfer transitions are not important in these measurements.
41. The  $\text{CH}_2\text{Cl}_2$  used contained an alkene preservative which caused some UV absorption. Since the results in  $\text{CH}_2\text{Cl}_2$  solutions are very similar to results in  $\text{CHCl}_3$  and  $\text{CCl}_4$ , there appears to be no affect on the dynamics.
42. P. A. D. de Maine, *J. Chem. Phys.* 24, 1091 (1956).
43. R. Marshall and N. Davidson, *J. Chem. Phys.* 21, 2086 (1953).
44. R. S. Mulliken, *J. Chem. Phys.* 55, 288 (1971).
45. K. S. Viswanathan, A. Sur, and J. Tellinghuisen, *J. Mol. Spectrosc.* 86, 393 (1981).
46. J. Tellinghuisen, *J. Mol. Spectrosc.* 94, 231 (1982).
47. P. B. Beeken, E. A. Hanson, and G. W. Flynn, *J. Chem. Phys.* 78, 5892 (1983).
48. The absorption strength at 295 nm is uncertain because of a different experimental configuration at that wavelength. The absorption coefficient was obtained by scaling the absorption strength at each wavelength to the magnitude of the A'-state bleach component at 500 nm. It was assumed that  $\epsilon_{500}(\text{A}') = 0$  and  $\epsilon_{500}(\text{X}) = 800 \text{ L-mol}^{-1}\text{-cm}^{-1}$ .
49. J. Tellinghuisen, A. R. Whyte, and L. F. Phillips, *J. Phys. Chem.* 88, 6084 (1984).
50. L. M. Julien and W. B. Person, *J. Phys. Chem.* 72, 3059 (1968).
51. J. P. Perrot, M. Broyer, J. Chevaleyre, and B. Femelat, *J. Mol. Spectrosc.* 98, 161 (1983).
52. K. S. Viswanathan and J. Tellinghuisen, *J. Mol. Spectrosc.* 101, 285 (1983).
53. G. T. Evans and M. Fixman, *J. Phys. Chem.* 80, 1544 (1976).
54. B. Martire and R. G. Gilbert, *Chem. Phys.* 56, 241 (1981).

55. D. R. Bauer, J. I. Brauman, and R. Pecora, *J. Am. Chem. Soc.* 96, 6840 (1974).
56. F. D. Rossini, K. S. Pitzer, R. L. Arnett, R. M. Brown, and G. C. Pimentel, Selected Values of Physical and Thermodynamic Properties of Hydrocarbons and Related Compounds, American Petroleum Institute Project 44 (Carnegie Press, Pittsburgh, 1953) Tables 20c, 23c; J. A. Dean, ed., Lange's Handbook of Chemistry, 12<sup>th</sup> ed., (McGraw-Hill, New York, 1979), Table 10-35.
57. J. T. Hynes, R. Kapral, and G. M. Torrie, *J. Chem. Phys.* 72, 177 (1980).
58. M. Schell and R. Kapral, *Chem. Phys. Lett.* 81, 83 (1981).
59. K. J. Shin and R. Kapral, *J. Chem. Phys.* 69, 3685 (1978).
60. M. W. Balk, C. L. Brooks, III, and S. A. Adelman, *J. Chem. Phys.* 79, 804 (1983).
61. C. L. Brooks, III and S. A. Adelman, *J. Chem. Phys.* 80, 5598 (1984).
62. J. M. Dawes and M. G. Sceats, *Chem. Phys.* 96, 315 (1985).
63. D. L. Bunker and B. S. Jacobsen, *J. Am. Chem. Soc.* 94, 1843 (1972).
64. J. N. Murrell, A. J. Stace and R. Dammell, *J. Chem. Soc. Faraday Trans. 2* 74, 1532 (1978).
65. A. H. Lipkus, F. P. Buff and M. G. Sceats, *J. Chem. Phys.* 79, 4830 (1983).
66. J. M. Deutch and I. Oppenheim, *J. Chem. Phys.* 54, 3547 (1971); J. Albers, J. M. Deutch, and I. Oppenheim, *J. Chem. Phys.* 54, 3541 (1971); P. Mazur and I. Oppenheim, *Physica* 50, 241 (1970).
67. D. P. Ali and W. H. Miller, *J. Chem. Phys.* 78, 6640 (1983); D. P. Ali and W. H. Miller, *Chem. Phys. Lett.* 105, 501 (1984).
68. T. Shimanouchi, Tables of Molecular Vibrational Frequencies, Consolidated Volume I, Nat. Stand. Ref. Data Ser., Nat. Bur. Stand. (U.S.), 39 (U. S. Government Printing Office, Washington, D. C., 1972).
69. R. J. LeRoy, *J. Chem. Phys.* 52, 2683 (1970).

70. The resonant transfer width is taken to be  $h\alpha (kT/\mu)^{1/2}/2$ , where  $\alpha$  is the range of the exponential interaction potential and  $\mu$  is the reduced mass of the collision. Eq. 5.4 of Ref. 3, which was used to calculate the V-V energy transfer rates, should read:

$$\Delta E^{VV}(v \rightarrow v-1) = - \left( \frac{2}{\pi} \right)^{1/2} h \omega_{I_2} \left( \frac{2\mu |U_{if}|}{h\alpha} \right)^2 \left( \frac{\mu}{kT} \right)^{3/2} e^{\Delta E/2kT} \\ \times \int_0^\infty dv_0 v_0^4 \exp \left( \frac{-\mu v_0^2}{2kT} \right) \operatorname{sech}^2 \left( \frac{2\Delta E}{h v_0 \alpha} \right)$$

71. C. B. Moore, J. Chem. Phys. 43, 2979 (1965).
72. R. J. Myers and W. D. Gwinn, J. Chem. Phys. 20, 1420 (1952).
73. S. N. Ghosh, R. Trambarulo, and W. Gordy, J. Chem. Phys. 20, 605 (1952).
74. D. J. Nesbitt and J. T. Hynes, J. Chem. Phys. 76, 6002 (1982).
75. J. B. Koffend, R. Bacis, and R. W. Field, J. Chem. Phys. 70, 2366 (1979).
76. J. I. Steinfeld, J. Chem. Phys. 44, 2740 (1966).
77. G. A. Capelle and H. P. Broida, J. Chem. Phys. 58, 4212 (1973).
78. J. I. Steinfeld, Rate Data for Inelastic Collision Processes in the Diatomic Halogen Molecules, JILA Information Center Report No. 24 (University of Colorado, Boulder, 1984).
79. R. F. Barrow and K. Y. Yee, J. Chem. Soc., Faraday II 69, 684 (1973).
80. M. Geilhaupt and Th. Dorfmueller, Chem. Phys. 76, 443 (1983).
81. R. N. Zare, J. Chem. Phys. 40, 1934 (1964).
82. M. L. Sage, Chem. Phys. 35, 375 (1978).
83. M. S. Child, Molecular Collision Theory, (Academic Press, New York, 1974) Appendix A.

Chapter 3: Generation of Tunable Short Pulses in the Vibrational Infrared by Stimulated Electronic Raman Scattering from the Cesium 6s-5d Transition

I. INTRODUCTION

New sources of tunable short light pulses in the vibrational infrared (2-20  $\mu\text{m}$ ; 500-5000  $\text{cm}^{-1}$ ) are needed for studies of molecular and solid state dynamics. Because of the lack of tunable laser sources in the vibrational infrared, the generation of short pulses in this region has been based on various frequency shifting mechanisms. In the work presented in this chapter, one such frequency shifting technique, stimulated electronic Raman scattering (SERS) is investigated as a source of widely tunable nanosecond and picosecond infrared light pulses.<sup>1-3</sup> The experiments demonstrate that SERS infrared generation may be accomplished with tunable yellow-red light pulses on the cesium 6s-5d transition. The tuning range of nanosecond infrared pulses is thereby greatly extended using Nd:YAG-laser pumped rhodamine-dye lasers as pump sources. Tunable, intense picosecond infrared pulses are also generated by shifting light pulses from a reliable picosecond rhodamine-dye laser.

Existing methods for generating short infrared pulses are limited by tuning range, pulse width, and practical experimental considerations. Tunable nanosecond pulses are difficult to generate at wavelengths longer than 4  $\mu\text{m}$  by difference frequency mixing<sup>4</sup> or by stimulated Raman scattering in molecular gases.<sup>5</sup> Picosecond pulse

generation by difference frequency generation has been reported, but with low peak and average powers<sup>6,7</sup>. Picosecond pulses with higher peak powers can be generated by using optical parametric generation<sup>8-12</sup>, but this method suffers from the need to simultaneously tune several crystals and from problems of crystal damage. Furthermore, pulses of a few picoseconds duration have only been generated from low repetition rate, relatively unstable Nd:glass lasers.

Recently, stimulated electronic Raman scattering (SERS) in atomic vapors has been investigated as a method of generating tunable short infrared light pulses.<sup>13-19</sup> SERS has the advantages of high efficiency, lack of phase matching requirements and a non-damageable medium. Previous work has demonstrated the generation of narrowband<sup>14</sup> ( $\sim 0.5 \text{ cm}^{-1}$  bandwidth) and broadband<sup>15,16</sup> ( $>200 \text{ cm}^{-1}$  bandwidth) nanosecond infrared light pulses, using tunable blue and ultraviolet pump light. The generation of tunable picosecond infrared pulses by SERS has also been demonstrated using a blue picosecond pump laser.<sup>19</sup> The difficulties in operating tunable blue or UV pump lasers, especially for picosecond pulses, limits the practical applications of these techniques.

In the work described here tunable yellow-red nanosecond and picosecond light pulses from reliable rhodamine-dye lasers were used to generate frequency shifted infrared pulses by scattering from the cesium  $6s-5d$  Raman transition. Visible nanosecond pulses (550 nm to 650 nm) were used to generate widely tunable narrowband ( $3450 \text{ cm}^{-1}$  to  $900 \text{ cm}^{-1}$ ) and broadband ( $3390 \text{ cm}^{-1}$  to  $1800 \text{ cm}^{-1}$ ) nanosecond vibrational infrared light pulses. Picosecond visible pulses (568-604 nm) from an amplified synchronously pumped dye laser were used to generate picosecond infrared pulses ( $3040-1950 \text{ cm}^{-1}$ ).

Section II discusses the use of SERS on the cesium 6s-5d transition, and describes the atomic vapor source, which must be designed to minimize the concentration of light absorbing cesium dimers. Section III presents the results of the generation of narrowband and broadband nanosecond infrared pulses. Section IV describes the generation of picosecond infrared pulses.

## II. STIMULATED ELECTRONIC RAMAN SCATTERING IN CESIUM

### A. Stimulated Electronic Raman Scattering

In the SERS process, atomic energy level spacings of 10,000-30,000  $\text{cm}^{-1}$  may be used to provide large frequency shifts of visible or ultraviolet light. The visible or UV pump laser energy is coupled to a frequency-shifted (Stokes) wave through the third order nonlinear susceptibility,  $\chi^{(3)}$ , of the atomic vapor. Much work has examined the possibility for shifting visible pulses into the infrared,<sup>13-22</sup> and several studies have also demonstrated efficient shifting of excimer laser UV pulses into the blue-green.<sup>23-26</sup>

Although atomic vapors are characterized by a low number density in comparison with other nonlinear media, the nonlinear susceptibility can still be large if the optical frequencies are tuned into near-resonance with strong atomic transitions. In particular, enhancement in SERS is provided by near-resonance between the pump laser and the intermediate Raman level, usually lying above the final level of the Raman transition. For instance, in scattering on the cesium 6s-7s transition, the pump laser is in near-resonance with intermediate 7p levels (Fig. 1a). Extensive theoretical and experimental discussions of SERS and other nonlinear optical processes in atomic vapors may be found in Refs. 13 and 18.

If a single intermediate state in near resonance with the pump laser dominates the Raman scattering cross section the atom can be approximated as a 3-level system. If levels 1, 2, and 3 are the initial, intermediate, and final levels, the steady state Raman gain can

be written:<sup>13,20</sup>

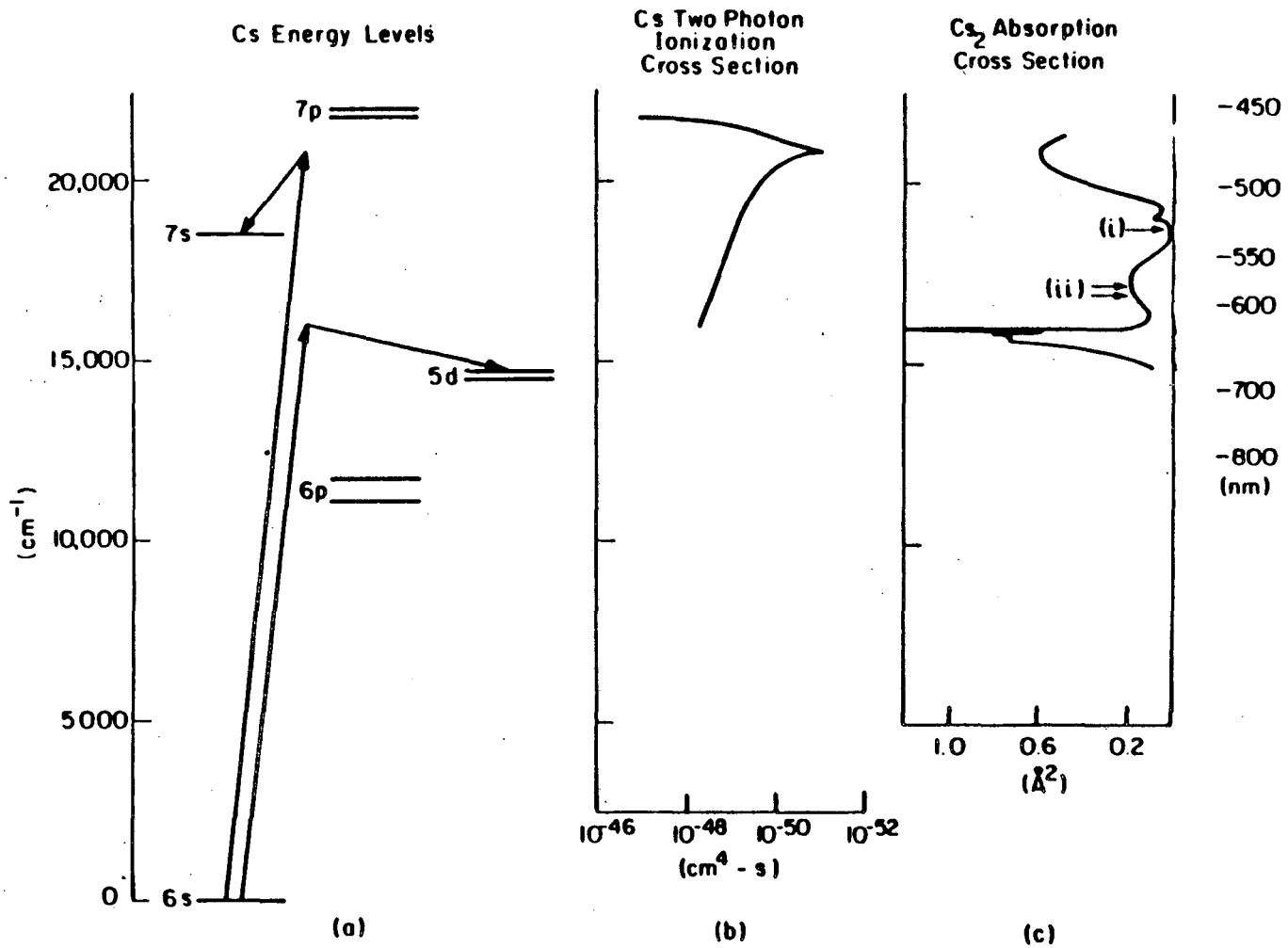
$$g \propto N \frac{I_L}{\Gamma} \left[ \frac{f_{12} f_{23} \nu_s}{\nu_{12} \nu_{23} (\nu_L - \nu_{12})^2} \right] \quad (1)$$

where  $N$  is the density of atoms,  $I_L$  is the pump laser intensity,  $\Gamma$  is the intermediate level linewidth,  $f_{ij}$  is the oscillator strength between levels  $i$  and  $j$ ,  $\nu_{ij}$  is the transition frequency between levels  $i$  and  $j$ , and  $\nu_L$  and  $\nu_s$  are the pump laser and shifted Stokes frequencies. In addition to the resonance denominator the Raman gain is determined by the oscillator strengths coupling the intermediate level to the initial and final levels. The gain is also proportional to the frequency of the shifted Stokes light, so that infrared generation is increasingly difficult at low frequencies ( $<1000 \text{ cm}^{-1}$ ).

#### B. Cesium 6s-5d Raman Transition

The 6s-5d transition in atomic cesium (see Fig. 1a) was chosen for this work because its  $14597 \text{ cm}^{-1}$  transition frequency shifts red pulses into the vibrational infrared spectral region. The relative energy needed to reach threshold (exponential gain of  $e^{gZ} = e^{30}$ ) as a function of the generated infrared frequency is plotted for the 6s-5d Raman and the previously studied 6s-7s Raman transitions in Fig. 2., using Eq. (1) and published values for the transition oscillator strengths.<sup>27</sup> The 6s-7s transition shows a strong resonance dip in the threshold energy when the pump frequency approaches the intermediate 6s-7p transition frequency. In contrast, the 6s-5d transition is predicted to have a relatively constant threshold because of the nature of its intermediate

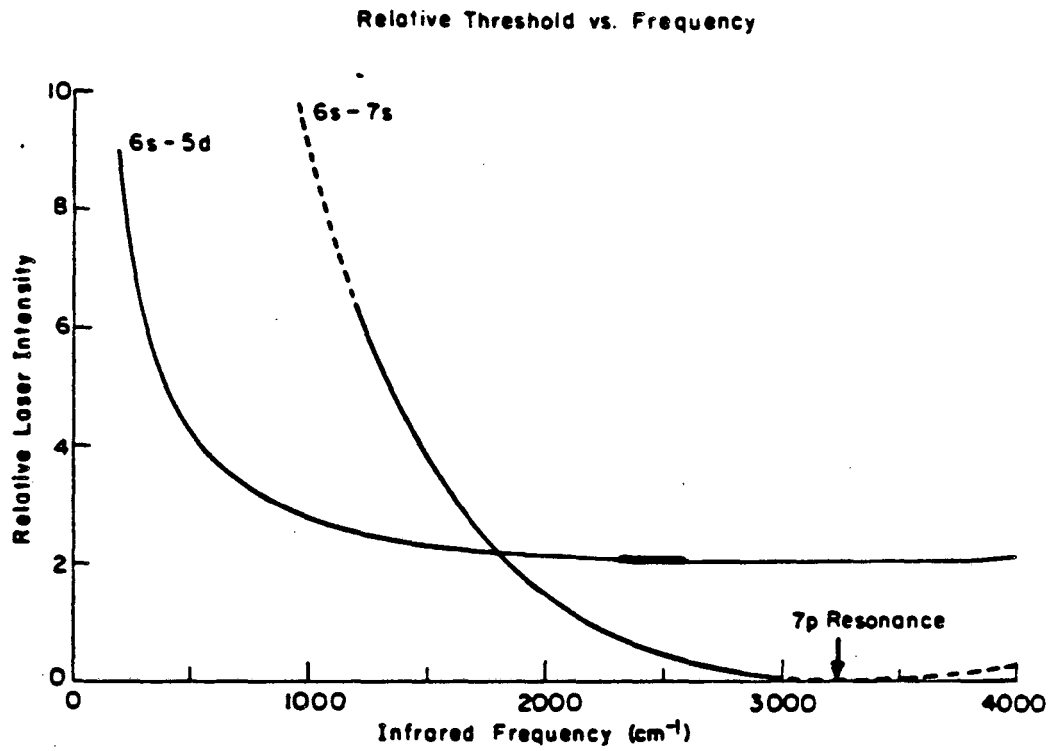
FIG. 1. Cs atom and Cs<sub>2</sub> dimer spectroscopy important for SERS infrared generation. a). Partial energy level diagram of the Cs atom showing the 6s-7s Raman transition used previously (see Refs. 14 and 19), and the 6s-5d Raman transition used in the present work. b) Theoretical two photon ionization cross section of the Cs atom as a function of visible frequency (Ref. 41). c) Absorption cross section of the Cs<sub>2</sub> dimer in the visible (Ref. 28). Arrow (i) marks the minimum in the dimer absorption cross-section at 18800 cm<sup>-1</sup>. Arrows (ii) mark the tuning range for picosecond infrared pulse generation.



XBL 835-5687

Figure 1 .

FIG. 2. Relative pump intensity needed to reach threshold calculated as a function of generated infrared frequency using Eq. (1) for the previously studied 6s-7s Raman transition (Refs. 14 and 19), and for the 6s-5d transition used in the present work. Losses due to diffraction of infrared light and to absorption of visible light by dimers are not included. The solid part of the 6s-7s line represents previous tuning range for picosecond pulses (Ref. 19).



JBL 635 5688

Figure 2

state resonance. Since the dominant intermediate 6p levels lie below the final level, the resonance enhancement is strongest at low infrared frequencies. This counteracts the decreased  $\nu_s$  factor in the Raman gain at low frequencies, providing a wide predicted tuning range.

The large oscillator strengths for the intermediate 6s-6p and 6p-5d transitions also result in a reasonably low predicted SERS threshold energy for the 6s-5d Raman transition. Previous picosecond and nanosecond pulse generation on the 6s-7s Raman transition has been accomplished at infrared frequencies as low as  $1200 \text{ cm}^{-1}$  and  $2100 \text{ cm}^{-1}$ , respectively.<sup>14,19</sup> Thus, based on the approximate gain calculation, a broad tuning range ought to be accessible at reasonable pump energies on the 6s-5d transition.

Several loss terms in the SERS process affect the experimental gain. First, the approximate gain calculation does not include the loss in Stokes infrared intensity which occurs from diffraction of the infrared beam out of the pumped region. At long wavelengths, the diffraction loss is substantial, and contributes to a more steeply rising threshold at low infrared frequencies.<sup>21,22</sup> This effect limits long wavelength infrared tuning.

A more serious loss process occurs because of absorption of visible pump light by cesium dimers in the atomic vapor. Fig. 1c illustrates that for pump frequencies away from the dimer absorption minimum at  $18800 \text{ cm}^{-1}$  (infrared frequency of  $4200 \text{ cm}^{-1}$ ) the dimer absorption strength is substantial.<sup>28</sup> On the 6s-7s transition the dimer absorption appears to be counteracted by the strong resonance obtained from the 7p intermediate states.<sup>13,19</sup> On the 6s-5d transition, however, the dimer absorption presents more serious problems. Without reducing the dimer

density, tunable nanosecond infrared generation is only possible above  $3890\text{ cm}^{-1}$ , and picosecond pulse generation has only been demonstrated at  $4200\text{ cm}^{-1}$ .<sup>20-22</sup>

It has been recently shown that by thermally dissociating the dimers in a superheated vapor, SERS threshold could be reached at  $3100\text{ cm}^{-1}$  with nanosecond pulses on the 6s-5d transition.<sup>21</sup> In the present work, an improved superheated vapor arrangement allows wide tunability and routine infrared generation with nanosecond pulses down to  $900\text{ cm}^{-1}$ , and the first SERS generation of tunable picosecond infrared pulses on the 6s-5d transition.

### C. Reduction of the Cesium Dimer Density

For a saturated vapor of cesium, attenuation of the visible pump light by absorption of cesium dimers prohibits SERS generation with visible light at wavelengths between 560 and 660 nm. With a typical atom density of  $5 \times 10^{17}\text{ cm}^{-3}$  (40 torr, 720 K) in a 100 cm vapor column, the equilibrium concentration of dimers is  $1.4 \times 10^{16}\text{ cm}^{-3}$ . The absorption cross section between 560 and 660 nm is greater than  $2 \times 10^{-17}\text{ cm}^2$ , and the transmission of pump light would only be  $10^{-13}$ .

By superheating the cesium vapor above its liquid-vapor equilibrium temperature, the cesium dimers can be thermally dissociated, and visible losses are reduced. Assuming that the atoms and dimers are each nearly ideal gases, and that the dimer density is a small fraction of the atom density, the dimer density can be simply calculated from the equilibrium

constant,  $K_p$ , for dimerization:

$$\rho_{\text{Cs}_2} = k_B T K_p (\rho_{\text{Cs}})^2$$

where  $k_B$  is Boltzmann's constant ( $1.362 \times 10^{-22} \text{ cm}^3 \text{ atm K}^{-1}$ ),  $T$  is the absolute temperature (K),  $K_p$  is the equilibrium constant ( $\text{atm}^{-1}$ ), and the densities are in units of  $\text{cm}^{-3}$ . The equilibrium constant is plotted as a function of absolute temperature in Fig. 3, based on published thermodynamic data.<sup>29,30</sup> The thermodynamic data of Ref. 30 were extrapolated to calculate  $K_p$  above 1500 K.

Using the temperature dependent equilibrium constant in Eq. (2), and a visible absorption cross section of  $2 \times 10^{-17} \text{ cm}^2$  (see Fig. 1c), the theoretical transmission of a superheated 100 cm cesium vapor column at 560-580 nm is plotted in Fig. 4. For atom densities below  $5 \times 10^{17} \text{ cm}^{-3}$ , the transmission of the column is very high for temperatures above 1200 K. At densities above  $5 \times 10^{17} \text{ cm}^{-3}$ , however, it is difficult to thermally dissociate all of the dimers, because the equilibrium constant does not decrease as rapidly at high temperature (Fig. 3). Available materials for the vapor oven limit practical operating temperatures to 1500 K. Therefore, an atom density of  $\sim 5 \times 10^{17} \text{ cm}^{-3}$  (78 torr at 1500 K) is a reasonable maximum, although this conclusion is somewhat dependent on the actual vapor column length.

In designing an oven to contain the atomic vapor, a compromise was made between maximum transmission and simple design and construction. While ceramics or refractory metals are capable of operation at temperatures approaching 2000 K, special designs would be necessary. Instead, a high temperature nickel-chromium alloy, Inconel 601, was

FIG. 3. Temperature dependence of the cesium monomer - dimer equilibrium constant from thermodynamic data of Refs. 29 and 30. Dashed line above 1500 K is calculated from extrapolated data of Ref. 30.

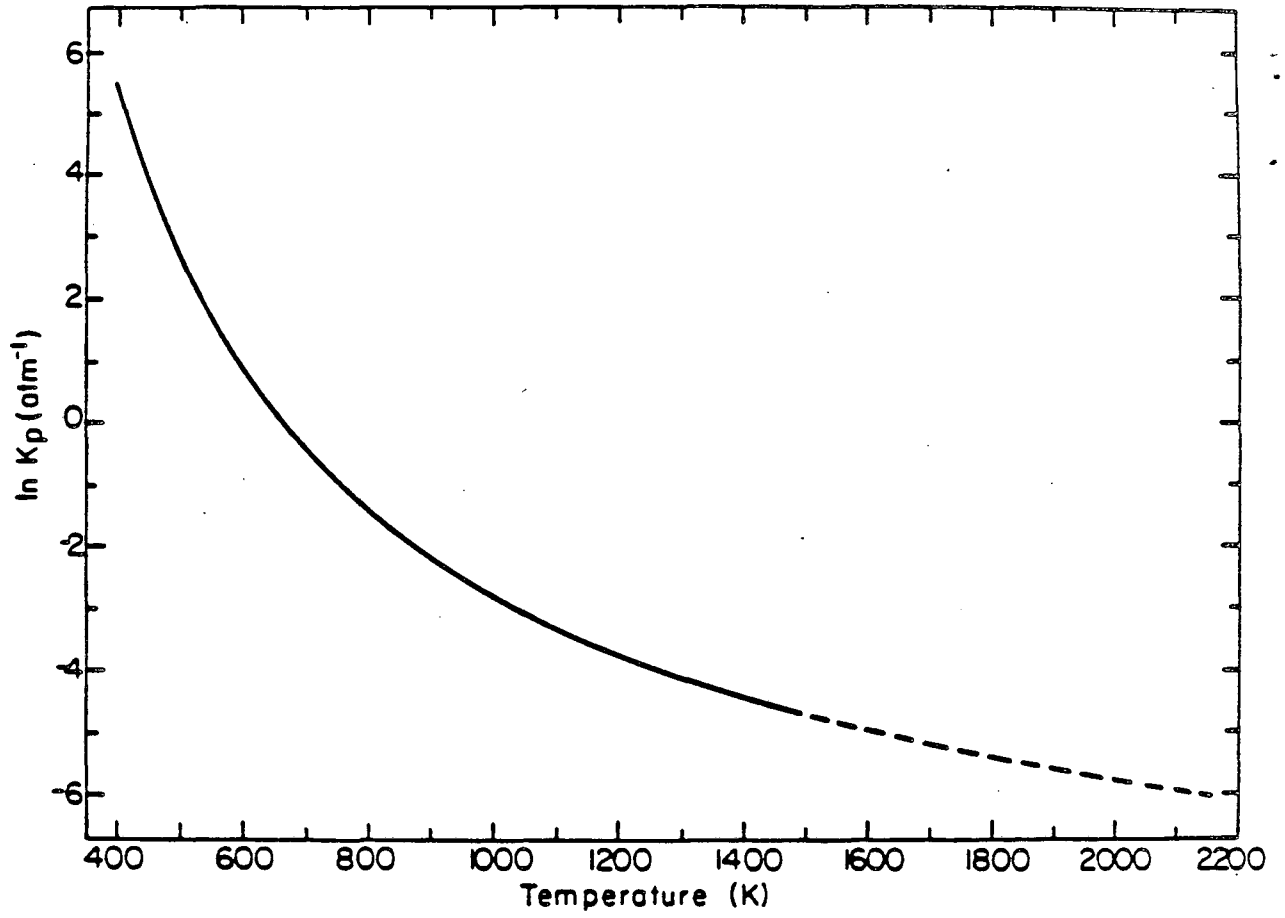
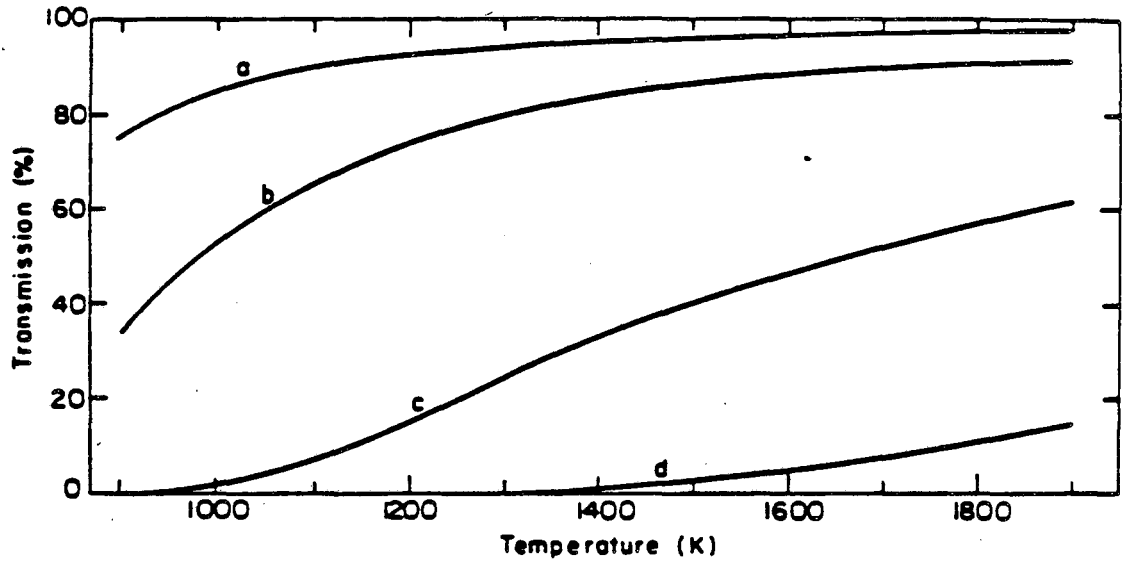


Figure 3

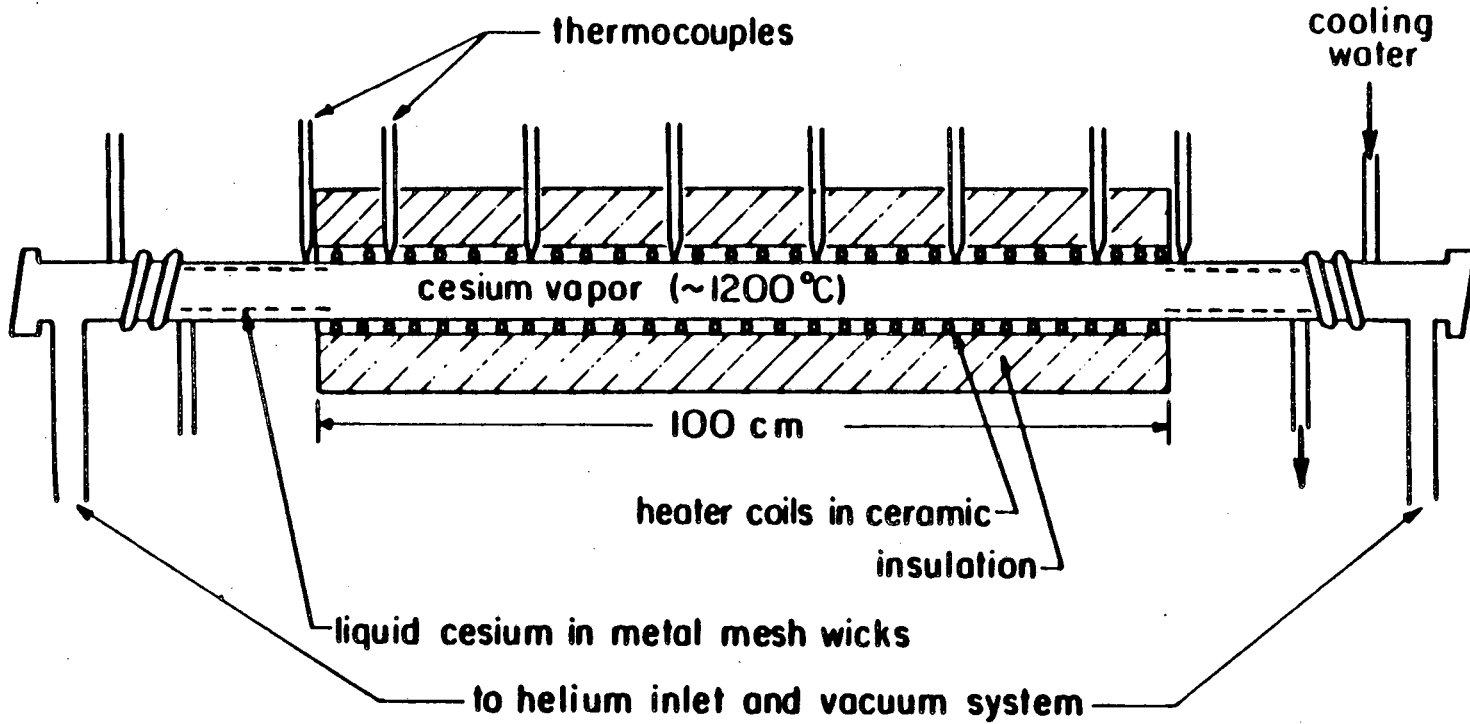
FIG. 4. Theoretical optical transmission as a function of temperature in a 100-cm vapor column of cesium, for a cesium dimer absorption cross section of  $2 \times 10^{-17} \text{ cm}^2$  (approximately that for 560-580 nm light). Atomic density ( $\text{cm}^{-3}$ ): a -  $10^{17}$ , b -  $2 \times 10^{17}$ , c -  $5 \times 10^{17}$ , d -  $10^{18}$ .



NEL 888-6574

Figure 4

FIG. 5. Split-wick heat pipe used to generate the cesium vapor column for stimulated electronic Raman scattering experiments.

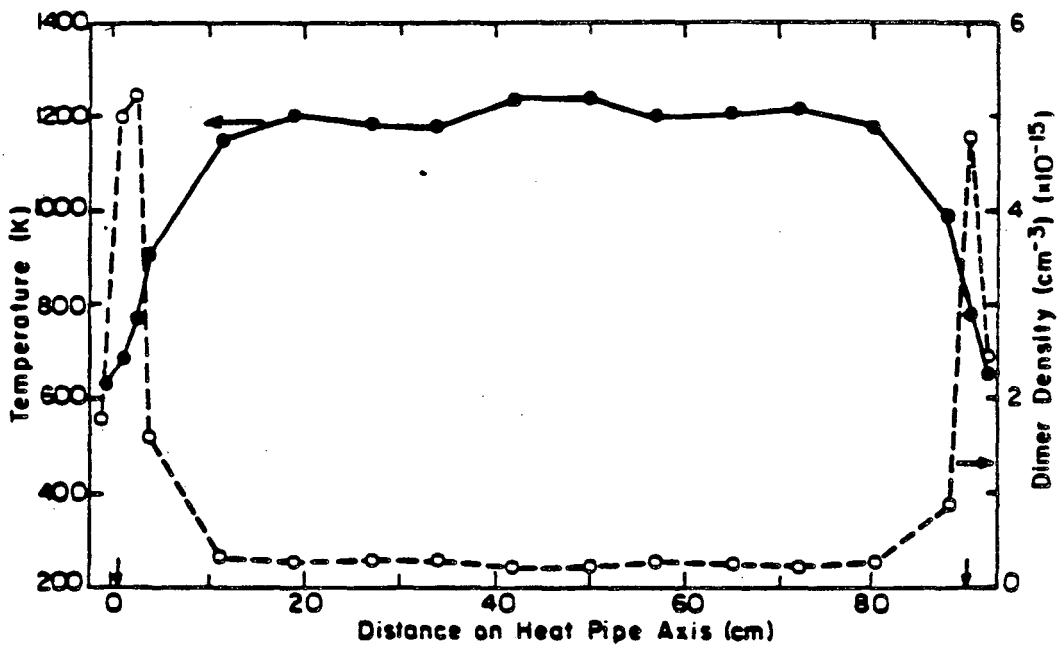


**SPLIT WICK CESIUM HEAT PIPE**

XBL8312-6465

Figure 5

FIG. 6. Measured wall temperature of the heat pipe as a function of position, and calculated cesium dimer concentration. The calculation of the dimer density assumes that the vapor temperature is equal to the wall temperature, and that the cesium vapor over the wicks is at equilibrium with the liquid. Arrows at 0 and 90 cm on the abscissa mark the beginning of the wicks at each end which contain the liquid cesium.



LAL 888-8578

Figure 6

chosen, which can be operated in air at 1500 K, yet can be easily machined and welded. In addition, the hot cesium vapor must be kept away from the entrance and exit windows. While this might be accomplished with a flowing gas system, a simpler split-wick heat pipe design was used.<sup>19</sup>

The helium buffered split-wick heat pipe is illustrated in Fig. 5. A 1.5 m x 2.5 cm O.D. Inconel 601 tube can be heated to 1500 K along a 90 cm central region. Commercial electrical resistance tube ovens are separately controlled in 5 sections (a central 30-cm section, and two 15-cm sections at each end) to maintain an even temperature along the pipe.<sup>31</sup> Cooling coils 15 cm from either end of the heaters prevent hot vapor from reaching the windows (BK-7 input window, NaCl output window). The cesium wicks which recirculate the condensed vapor consist of 4-5 rolls of 100 mesh 316 stainless steel screen, placed to end  $\frac{1}{2}$  cm from the ends of the heaters.

In operation, the helium buffer gas pressure controls the vapor pressure of the cesium. At the hot end of each wick, cesium boils and fills the central region of the tube. At the cooler end of each wick, the vapor condenses, and is drawn back toward the hot end. Further details on the operation and use of heat pipe ovens can be found in Ref. 13.

The transmission of the middle, superheated vapor section can be high (Fig. 4). Since the end-sections of vapor over the wicks are saturated, however, they contain most of the remaining dimers. The end section lengths were minimized by placement of the wicks and adjustment of the heater powers. The best operation was a compromise between shortening the saturated end sections and avoiding unstable interfaces,

which produce a mist that blocks visible transmission. Figure 6 illustrates the measured pipe temperature and calculated density of dimers with a typical set of operating conditions, and shows that even with careful placement of the wicks, most of the dimers remain in the end sections. The best transmission actually obtained at 560-590 nm and 50 torr vapor pressure was 20%. This compares to a theoretical transmission of 68% for a one meter vapor length heated to 1500 K, with no saturated end sections.

To generate nanosecond or picosecond infrared pulses, the dye laser beams of ~6 mm diameter were focused near the middle or far end of the heat pipe using a 3:1 telescope. The lowest SERS thresholds were found at atomic densities of  $\sim 3.5 \times 10^{17} \text{ cm}^{-3}$  (55 torr at 1500 K), in agreement with the expected competition between atom density and dimer absorption. Infrared energies were measured with a calibrated pyroelectric energy meter, after a germanium filter. Infrared spectra were taken with a Au:Ge detector (1.5 ns response time) and an infrared monochromator with  $0.4 \text{ cm}^{-1}$  resolution. All SERS scattering observed was to the  $5d \ ^2D_{5/2}$  sublevel.

### III. GENERATION OF WIDELY TUNABLE NANOSECOND INFRARED PULSES

#### A. Narrowband Infrared Generation

The narrowband dye laser was a commercial Nd:YAG pumped scanning dye laser. Using rhodamine and DCM dyes, 25-50 mJ light pulses of 5-10 nanosecond duration were obtained from 550 nm to 650 nm. The spectral bandwidth of the light pulses was specified as  $<0.4 \text{ cm}^{-1}$ .

The input energy threshold for narrowband SERS infrared generation at 50 torr operating pressure is 2 mJ at 560 nm ( $3225 \text{ cm}^{-1}$  infrared). The threshold rises to 6.5 mJ at 617 nm ( $1610 \text{ cm}^{-1}$  infrared), and rises above the available pump energy of 25 mJ at 645 nm ( $900 \text{ cm}^{-1}$  infrared). The observed increase in the threshold at lower Stokes infrared frequency is somewhat steeper than predicted by Fig. 2, or by a similar calculation which includes Stokes diffraction losses.<sup>21</sup> Since visible losses at 560 nm and 617 nm are nearly identical, they do not account for the discrepancy. As has been noted<sup>14</sup>, not all of the factors affecting the SERS gain are yet well understood.

The narrowband infrared energy was recorded as a function of visible input wavelength. A substantial fraction (~30%) of the infrared energy passing the germanium filter was found to be amplified spontaneous emission (ASE) from excited cesium atom transitions, near  $3230 \text{ cm}^{-1}$  and  $2860 \text{ cm}^{-1}$ . These emissions were eliminated or corrected for by using bandpass infrared filters to obtain true tunable SERS energy.

The infrared tuning curves for four dyes are shown in figure 7 (a-d). Together, they show tuning from  $3450 \text{ cm}^{-1}$  to  $900 \text{ cm}^{-1}$ , with

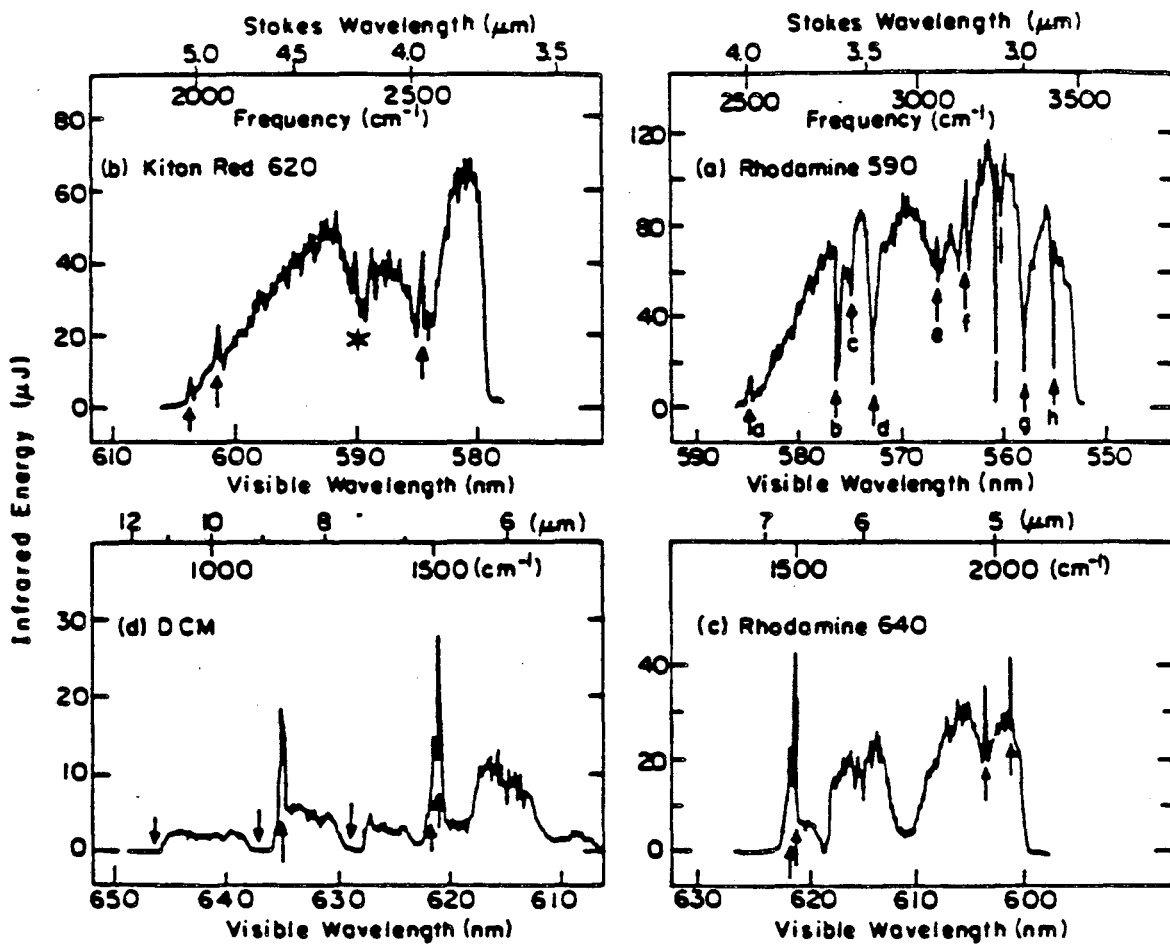
sufficient overlap between dyes to fill the tuning range. The quantum conversion efficiency reaches 2.5% in the range  $3300\text{ cm}^{-1}$  to  $2600\text{ cm}^{-1}$ , is around 1% at  $1700\text{ cm}^{-1}$ , then drops to 0.2% at  $900\text{ cm}^{-1}$ . Increased visible absorption by dimers<sup>28</sup> and increased Stokes diffraction losses<sup>21</sup> may cause the lower efficiency below  $1700\text{ cm}^{-1}$ .

The bandwidth of the narrowband infrared is  $0.5\text{ cm}^{-1}$  at  $2250\text{ cm}^{-1}$ , as measured by the linewidth of vibration-rotation absorptions from atmospheric  $\text{CO}_2$ . This shows a small or nonexistent broadening from the specified visible bandwidth of  $0.4\text{ cm}^{-1}$ . The infrared pulse width is typically 3-4 nanoseconds, considerably shorter than the visible pump.

Most of the structure in the tuning curves can be assigned to absorption of visible or infrared light by 6p and 5d cesium atoms (see Fig. 8). Cesium dimers predissociate after absorption of visible light in the 550 nm to 650 nm range to give primarily 6p atoms along with some 5d atoms.<sup>32,33</sup> In addition, 5d atoms are created in the SERS process. When the visible pump or the generated infrared light is tuned to a transition from a populated 6p or 5d level to higher levels, the infrared generation is strongly damped. In addition, when the visible light is absorbed to give highly excited Rydberg atoms, additional infrared ASE is seen from a number of cesium atom transitions (Fig 8). Some of this light passes the infrared filters, giving a peak in the plot of infrared energy out versus wavelength in. While at most wavelengths the tuning curves show true SERS energy, these sharp peaks are predominantly fixed frequency ASE emissions.

The dips and ASE peaks marked by arrows in Fig. 7 are therefore identified with absorptions from the 6p or 5d atomic levels. For instance, in Fig. 7a, the lettered arrows correspond to the transitions

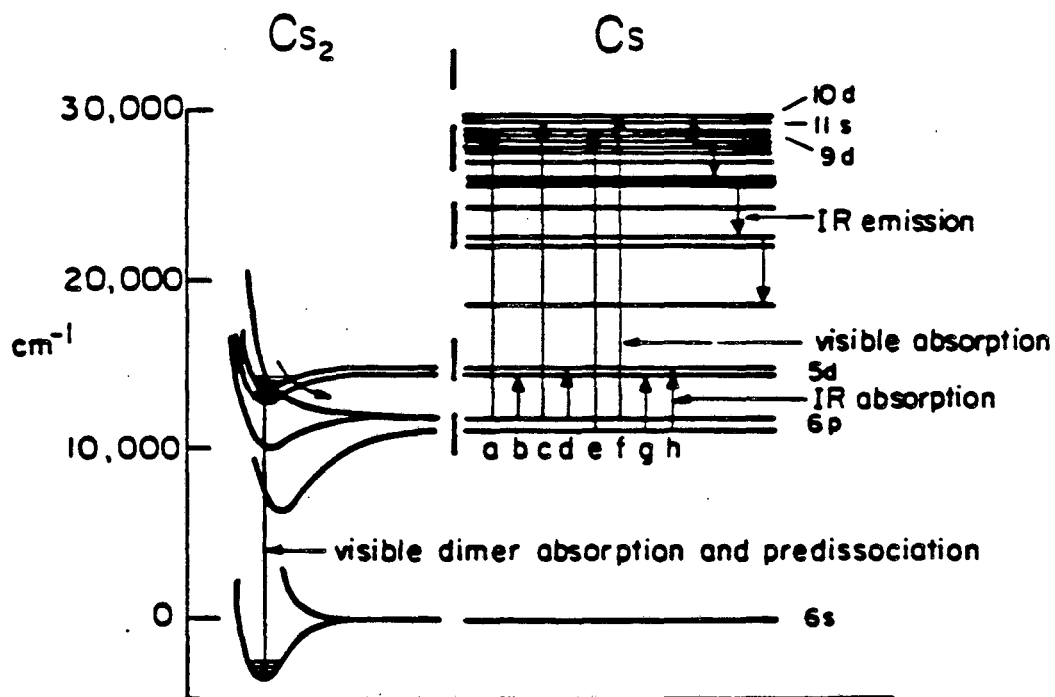
FIG. 7. Narrowband infrared energy obtained as a function of visible pump wavelength for four visible dyes. Arrows mark dips or ASE emission peaks resulting from 6p or 5d cesium atom absorptions. Labeled arrows in (a) correspond to labeled absorption transitions in Fig. 8. Lines in (a) mark dips assigned to 7s and 9s cesium atom absorptions. Asterisk in (b) marks atmospheric CO<sub>2</sub> infrared absorption. At slower scan rates CO<sub>2</sub> absorption lines are resolved and show a 0.5 cm<sup>-1</sup> line width.



XBL 839-64271

Figure 7

FIG. 8.  $\text{Cs}_2$  molecular states populated by 560-640 nm light predissociate to give Cs atoms in the 6p states. Subsequent absorption of visible or infrared light by 6p atoms creates tuning structure seen in Fig. 7. Transitions a-h correspond to structures in Fig. 7a, and are labeled in order from long pump wavelength to short pump wavelength. Transitions a,c,e, and f give absorptions of visible pump light; transitions b,d,g,and h give absorption of the shifted SERS infrared light. Amplified spontaneous emission of infrared light from higher atomic states can create peaks in the measured output infrared energy when visible light pumps the upper atomic states (see Fig. 7a).



XBL 8312-6666

Figure 8

marked in Fig. 8. Additional structure is also observed, including unassigned broad dips at 611 nm ( $1770 \text{ cm}^{-1}$  infrared), due to visible absorption, and 619 nm ( $1570 \text{ cm}^{-1}$  infrared), due to infrared absorption. A sharp absorption also appears at 560.8 nm ( $3230 \text{ cm}^{-1}$  infrared), which is assigned to cesium atom 7s-7p infrared absorption.

#### B. Broadband Infrared Nanosecond Pulses

In order to generate broadband infrared pulses, the pump radiation was obtained from a broadband dye laser consisting of a three stage dye amplifier originally constructed to amplify picosecond dye laser pulses. The amplifier was modified by placing a mirror at the input end and by turning off the saturable absorber dye jets which normally isolate one stage from the next. The system was otherwise operated as described in Chapter 4.

The threshold for infrared generation with broadband pulses centered at 560 nm is identical to the narrowband threshold at 560 nm. The threshold to longer wavelengths increases similarly in both cases. The lack of dependence on bandwidth is in agreement with experimental work on other transitions,<sup>15,16</sup> but contrasts sharply with previous work on the 6s-5d transition.<sup>21</sup> Theoretical calculations predict that the Raman gain should not be affected by increased bandwidth due to frequency modulation, but any associated amplitude modulation is difficult to model.<sup>34</sup> In any case, the present result demonstrates that the SERS threshold on this transition does not change even when the bandwidth is increased from  $0.5 \text{ cm}^{-1}$  to  $>200 \text{ cm}^{-1}$ .

The  $\sim$  nanosecond broadband visible pulses generate infrared pulses

shorter than the 1.5 nanosecond response time of the Au:Ge detector. Table I summarizes the visible and infrared pulse energies obtained with broadband pulses, and the infrared ranges covered with each broadband dye. The visible-to-infrared photon conversion efficiency, shown in the last column of Table I, decreases at lower frequencies, as in the narrowband infrared generation. The 14 mJ of broadband light from DCM was insufficient to reach threshold, which should be in the range of 15-20 mJ based on narrowband measurements. A more efficient broadband dye laser would improve the dye energies, broaden the tuning ranges, and might allow broadband generation well below  $1800 \text{ cm}^{-1}$ .

The broadband infrared spectra show dips at the same points as found in the narrowband spectra, due to excited cesium atom absorptions. In addition, when the visible pulse overlaps 6p visible absorptions, the output contains a number of ASE lines, as in the case of the narrowband pulses. Figure 9 illustrates the spectrum of the broadband infrared output obtained when the broadband visible laser is operated with rhodamine 640 dye. The arrows mark absorptions from the 6p levels, or emission from higher atomic levels pumped by the visible laser. It is estimated that ASE lines account for approximately 30% of the measured broadband infrared energies listed in Table I.

### C. Summary of Nanosecond Pulse Infrared Generation

The energies obtained in both the narrowband and broadband infrared generation compare reasonably well with previous results obtained on a series of higher cesium and rubidium transitions using blue and ultraviolet dyes.<sup>14-16</sup> The advantage of the present method lies in the

Table 1. Energies and spectral widths of broadband visible and SERS infrared light pulses.

<u>Dye/Solvent</u>	<u>Visible Pump Pulse</u>		<u>SERS Infrared Pulse</u>		Photon Conversion Efficiency (%)
	energy (mJ)	10% intensity points (nm)	energy (μJ)	10% intensity points (cm <sup>-1</sup> )	
Rhodamine 590/water	9	555 - 568	33	3390 - 3060	2.0
Rhodamine 610/methanol	37	569 - 587	75	2725 - 2560	2.6
Kiton Red 620/water	35	585 - 596	42	2450 - 2160	0.9
Rhodamine 640/water	20	595 - 615	5	2120 - 1798	0.3
DCM/methanol	14	627 - 658	--	---	---

FIG. 9. Spectrum of the broadband infrared light produced by cesium 6s-5d SERS shift of broadband visible light with rhodamine 640 dye in the broadband laser (see Table I). Arrows mark absorption dips from 6p cesium atoms and emission peaks from higher state atoms pumped by the visible pulse, as illustrated in Fig. 8. Vertical lines mark atmospheric water vapor absorption in the air path to the spectrometer.

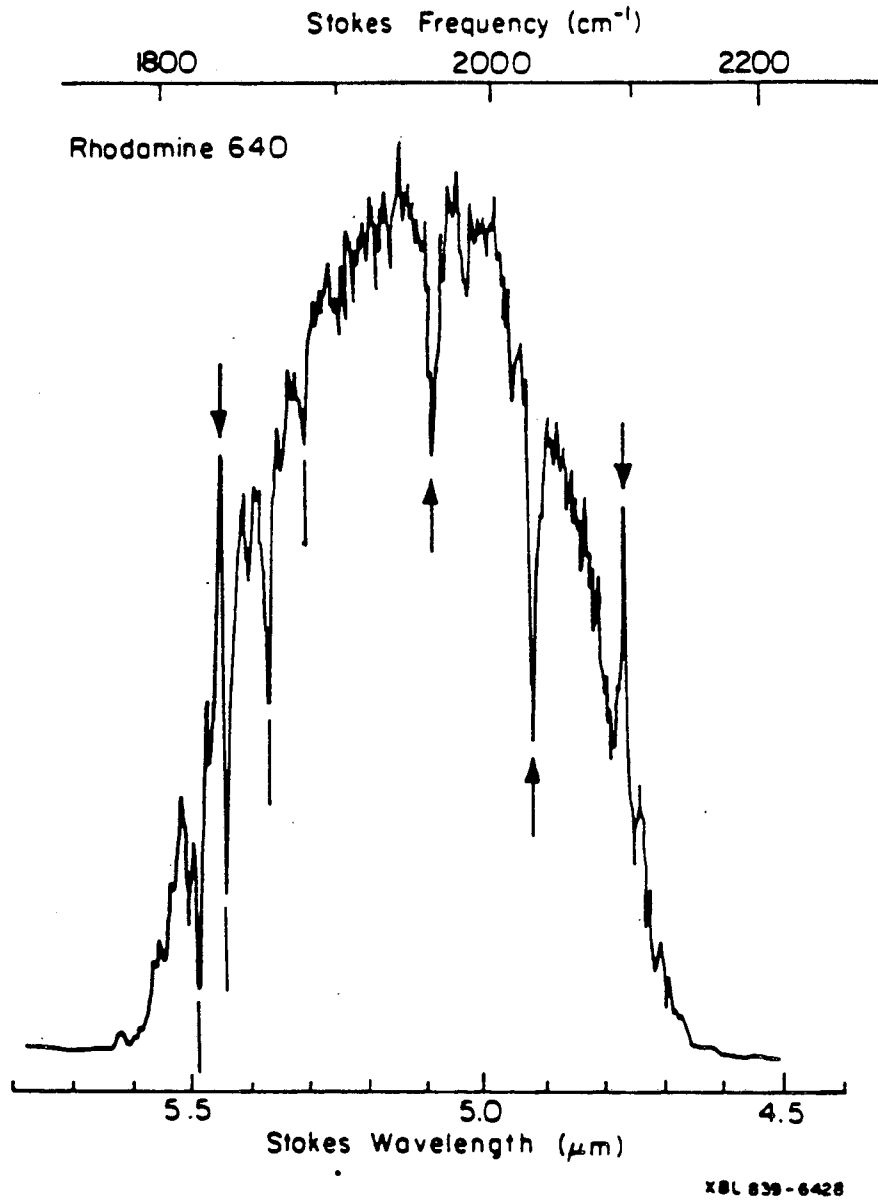


Figure 9

use of a single vapor and a single transition, along with reliable rhodamine dyes, to produce wide tuning ranges. Including the results of previous work,<sup>21</sup> coherent infrared radiation can now be generated from  $6000\text{ cm}^{-1}$  to  $900\text{ cm}^{-1}$  ( $1.7\text{ }\mu\text{m}$  to  $11.1\text{ }\mu\text{m}$ ) on the 6s-5d cesium transition, with a small tuning gap between  $3890$  and  $3450\text{ cm}^{-1}$  where SERS has not been attempted with the dyes available. This provides the broadest SERS tuning range obtained to date on a single atomic transition. Further reductions in the dimer density would be expected to improve the efficiency and reduce the structure in the tuning curves, and might extend the tuning range to even lower frequencies.

The tuning curve structure should also disappear if light pulses shorter than the predissociation lifetimes of the cesium dimers are used. In the picosecond SERS infrared generation to be discussed in the next section, tuning from  $3000\text{ cm}^{-1}$  to  $1950\text{ cm}^{-1}$  on the 6s-5d transition was achieved with optical pulses with 1-ps pulse width. No structure due to 6p absorptions is seen in the picosecond tuning curves.

#### IV. GENERATION OF TUNABLE PICOSECOND INFRARED PULSES

This section discusses the SERS generation of picosecond infrared in a system based on an amplified synchronously pumped dye laser using rhodamine dyes. Infrared picosecond pulses in the range  $3040\text{--}1950\text{ cm}^{-1}$  have been generated with up to 4.6% quantum efficiency. Extensions of this tuning range seem achievable. This is the first system to produce reliable pulses with pulse widths of less than a few picoseconds and with high peak power at a relatively high repetition rate in the vibrational infrared.

The amplified picosecond laser produces 1-2 mJ pulses from 565 nm to 610 nm (see Fig. 10). The pulse to pulse energy stability (standard deviation) is typically  $\pm 10\%$ . The amplified pulses have an autocorrelation with a 1.5 ps FWHM ( $1.0\text{ ps sech}^2$  pulse) and an average single pulse bandwidth of  $11\text{ cm}^{-1}$  giving a time-bandwidth product of 0.33 compared to 0.32 for a bandwidth limited  $\text{sech}^2$  pulse shape<sup>35</sup>. Further details of the laser system performance may be found in Chapter 4 of this thesis.

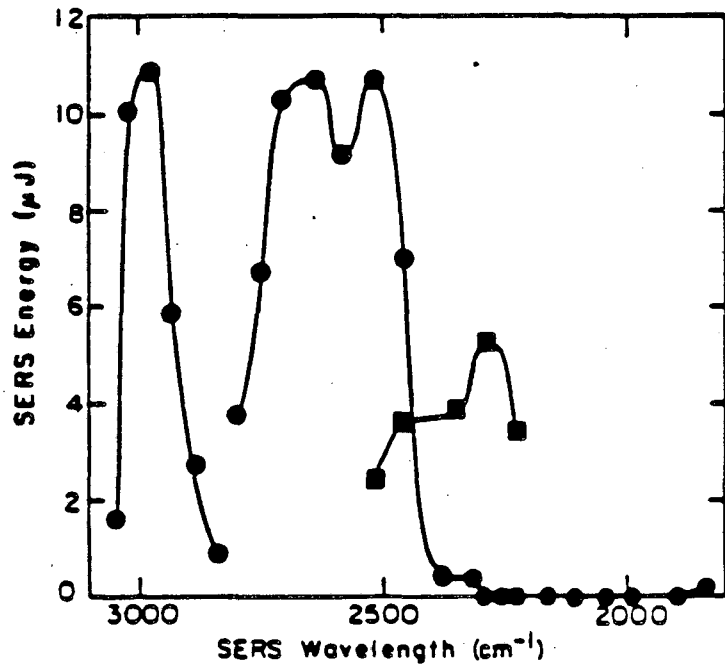
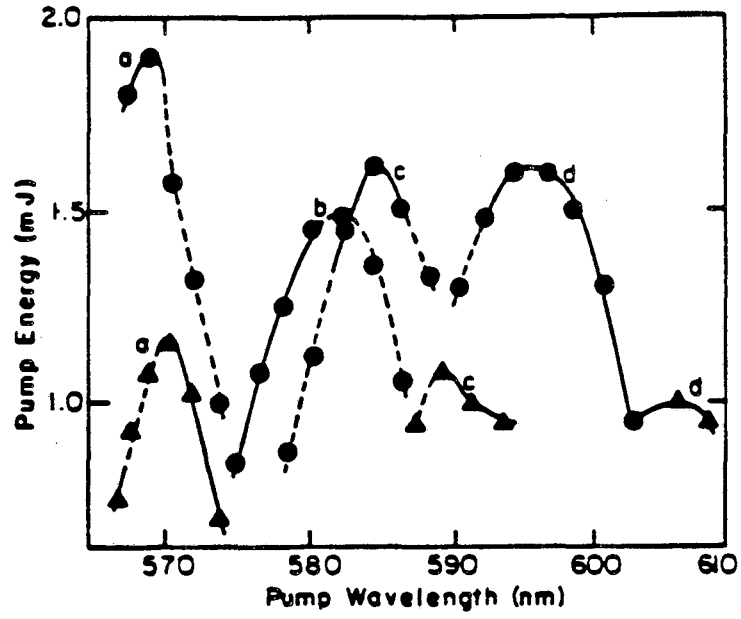
The SERS threshold is lowest when the beam profile is smooth and uniform. This is the case when water is used as the dye solvent in the amplifier system. If methanol is used, the turbulence of the dye flow occurring in the final amplifier stage is translated into random intensity variations across the amplified beam profile. Since this results in poorer focusing of the beam, the threshold of the SERS process is raised. The higher energies generally obtained with methanol solutions compensate somewhat for the detrimental effects of turbulence.

As in the nanosecond SERS work, the dye laser beam was focused into

the heat pipe with a 3:1 telescope. In addition to the tunable SERS output, fixed frequency emissions near  $3230\text{ cm}^{-1}$  (7p-7s) and  $2860\text{ cm}^{-1}$  (5d-6p) account for a significant fraction of the infrared energy, and were either blocked by infrared filters or corrected for in the energy measurements. The median infrared SERS energy obtained, as well as the visible energy used to obtain it, are shown as a function of wavelength in Fig. 10. In all cases, scattering to the  $5d_{5/2}$  sublevel was observed. A peak quantum efficiency of 4.6% occurs at  $2520\text{ cm}^{-1}$ . The dip in infrared generation near  $2850\text{ cm}^{-1}$  is due to the lack of a good dye for amplification of the picosecond pulse. This can probably be remedied by using different solvents to shift the dye tuning curves<sup>36</sup>. The bandwidth of the infrared pulses varied from 6 to  $10\text{ cm}^{-1}$ . This implies an infrared pulse length of 1-2 ps, if a Gaussian bandwidth limited pulse is assumed.<sup>35</sup> Since stimulated Raman scattering in the transient limit is expected to generate a Stokes pulse shorter than the pump pulse,<sup>37</sup> it is reasonable to believe that the infrared pulse is of this length. Furthermore, previous work on the cesium 6s-7p transition has implied a similar infrared pulse width.<sup>19</sup>

In contrast with the wide tuning range found in the nanosecond SERS generation discussed in the last Section, a reduction in picosecond SERS efficiency occurs below  $2500\text{ cm}^{-1}$  and is due to an increase in the non-linear losses that occurs with the shorter pulses. This conclusion is based on the fact that the tuning range can be extended by using longer pulses which have lower peak intensities but the same total energy. Figure 11 shows a large increase in SERS energy at  $2350\text{ cm}^{-1}$  as the input pulse to the dye amplifier is broadened.<sup>38</sup> At shorter wavelengths the SERS energy is relatively insensitive to pulse width. In the

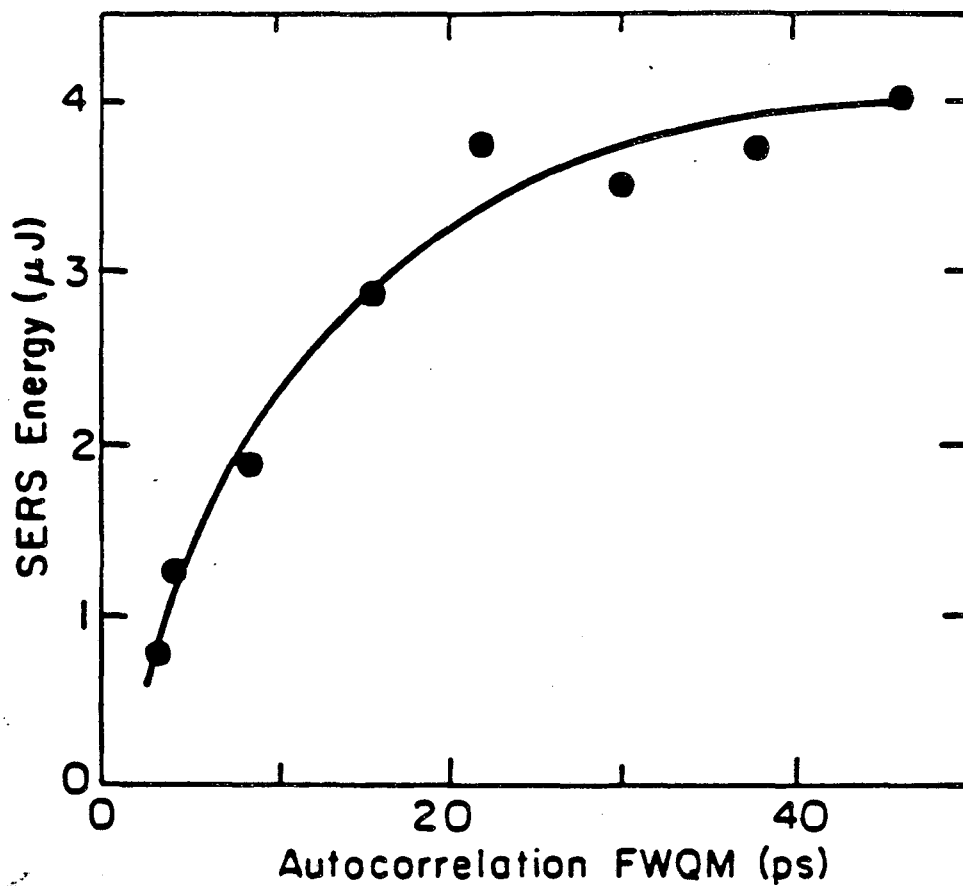
FIG. 10. Top: Visible pump pulse energy versus wavelength; a. R590, b. R 610, c. KR 620, d. R 640 ● - methanol solutions, ▲ - water solutions (no surfactants). Points used for best SERS generation are outlined with the solid portions of the curves. Bottom: ● - SERS energy generated with short pulses, □ - SERS energy generated with broad pulses.



KBL 839-4338

Figure 10

Fig. 11. SERS energy generated at  $2350 \text{ cm}^{-1}$  versus autocorrelation width of the input to the dye amplifier. Autocorrelation widths are measured at one quarter of the maximum height.



XBL839-6335

Figure 11

transient regime the SERS process should not be affected by pulse width changes at constant energy<sup>39</sup>; thus, the results of Fig. 11 imply that competing non-linear effects are being significantly reduced as the pulse width is increased. Furthermore, by broadening the input pulse autocorrelation from 2.2 ps to 21 ps, the transmission of the visible pulse through the heat pipe increases approximately 10%.

As an example of the increased tuning range of longer pulses, Fig. 10 (squares) shows the SERS energy generated over the tuning curve of Kiton Red in water with 21 ps input pulses (~10 ps amplified pulse). Significant amounts of SERS were also generated at the far end of the dye laser tuning range ( $1950\text{ cm}^{-1}$ ), although the actual energy was not measured. These results suggest that tuning even further into the vibrational infrared should be possible with the longer pulses.

The likely sources of non-linear loss are two photon ionization of cesium atoms or cesium dimers. Unfortunately experimental cross sections for these processes do not extend to the wavelengths used here.<sup>40</sup> The calculated cross section for the two photon ionization of cesium atoms,<sup>41</sup> however, is of the correct magnitude to contribute to the losses for 1-2 mJ pulses whose widths are on the order of a picosecond and is increasing with longer wavelength in this region (Fig. 1b).

It should be noted that a small amount of SERS was observed at the far end of the dye laser tuning range ( $1950\text{ cm}^{-1}$ ) even with short pulses (Fig. 10a). The increase in the generated infrared may result from approaching a minimum in the dimer absorption at 615 nm.<sup>28</sup> This suggests that a further reduction of the dimer concentration might extend the tuning range for the shorter pulses.

## V. SUMMARY

SERS from the 6s-5d transition in cesium has been demonstrated as a practical source of intense tunable short infrared pulses. Widely tunable narrowband nanosecond infrared pulses of up to 120  $\mu\text{J}$  were generated from 3450  $\text{cm}^{-1}$  to 900  $\text{cm}^{-1}$ . Broadband nanosecond pulses were generated from 3390  $\text{cm}^{-1}$  to 1800  $\text{cm}^{-1}$  with similar threshold and efficiency to that of the narrowband pulses. These tuning ranges were covered with visible pump pulses from reliable rhodamine dye lasers.

Picosecond visible pulses (568-604 nm) from an amplified synchronously pumped dye laser were used to generate picosecond infrared pulses from 3040-1950  $\text{cm}^{-1}$ . No tuning limitations to shorter wavelengths are foreseen for the picosecond pulses. Tuning to longer wavelengths with broad (>10 ps) pulses also seems possible. However, tuning below 2300  $\text{cm}^{-1}$  with <1 ps pulses may require additional reductions in the cesium dimer concentration. Further understanding of the exact origin of the non-linear losses will ultimately determine how well the 6000-900  $\text{cm}^{-1}$  tuning range for nanosecond pulses can be matched by picosecond pulses on this transition.

## REFERENCES

1. A. L. Harris, J. K. Brown, M. Berg and C.B. Harris, *Opt. Lett.* 9, 47 (1984).
2. M. Berg, A. L. Harris, J. K. Brown, and C. B. Harris, *Opt. Lett.* 9, 50 (1984)
3. A. L. Harris, M. Berg, J. K. Brown, and C. B. Harris, in Ultrafast Phenomena IV, edited by D. H. Auston and K. B. Eisenthal, Springer Series in Chemical Physics, Vol. 38 (Springer-Verlag, New York, 1984), p. 50.
4. L. Mannik and S. K. Brown, *Opt. Commun.* 47, 62 (1983).
5. W. Hartig and W. Schmidt, *Appl. Phys.* 18, 235 (1979).
6. C. A. Moore and L. S. Goldberg, *Opt. Commun.* 16, 21 (1976).
7. I. S. Ruddock, R. Illingworth, and L. Reekie, *Appl. Phys. B* 29, 177 (1982).
8. A. Seilmeier and W. Kaiser, *Appl. Phys* 23, 113 (1980).
9. A. Fendt, W. Kranitzky, A. Laubereau and W. Kaiser, *Opt. Commun.* 28, 142 (1979).
10. B. Bareika, G. Dilchys, E. D. Isyanova, A. Piskarskas and V. Sirutkaitis, *Sov. Tech. Phys. Lett.* 6, 301 (1980).
11. T. Elsaesser, A. Seilmeier and W. Kaiser, *Opt. Commun.* 44, 293 (1983).
12. T. Elsaesser, A. Seilmeier, W. Kaiser, P. Koidl, and G. Brandt, *Appl. Phys. Lett.* 44, 383 (1984).
13. D. C. Hanna, D. Cotter, and M. A. Yuratich, Nonlinear Optics of Free Atoms and Molecules, Springer Series in Optical Sciences, Vol. 17 (Springer-Verlag, New York, 1979).
14. D. Cotter, D. C. Hanna, and R. Wyatt, *Opt. Commun.* 16, 256 (1976).
15. D. S. Bethune, J. R. Lankard, M. M. T. Loy, and P. P. Sorokin, *IBM J. Res. Develop.* 23, 556 (1979).
16. D. S. Bethune, A. J. Schell-Sorokin, J. R. Lankard, M. M. T. Loy and P. P. Sorokin, in Adv. in Laser Spectroscopy, Vol. II, edited by B. A. Garetz and J. R. Lombardi (Wiley-Interscience, New York, 1983), p.1.
17. For example: a) J. Manners, *Opt Commun.* 44, 366 (1983). b) P. Bernage, P. Niay and R. Houdart, *Opt. Commun.* 36, 241 (1981). c) R. Burnham and N. Djeu, *Opt. Lett.* 3, 215 (1978).

18. D. Cotter and D. C. Hanna, *Opt. Quant. Elect.* 9, 509 (1977).
19. R. Wyatt and D. Cotter, *Opt. Commun.* 37, 421 (1981).
20. R. T. Hodgson, *Appl. Phys. Lett.* 34, 58 (1979).
21. R. Wyatt and D. Cotter, *Appl. Phys.* 21, 199 (1980).
22. R. Wyatt and D. Cotter, *Opt. Commun.* 32, 481 (1980).
23. N. Djeu and R. Burnham, *Appl. Phys. Lett.* 30, 473 (1977).
24. S. J. Brosnan, H. Komine, E. A. Stappaerts, M. J. Plummer, and J. B. West, *Opt. Lett.* 7, 154 (1982).
25. D. Cotter and W. Zapka, *Opt. Commun.* 26, 251 (1978).
26. R. Burnham and N. Djeu, *Opt. Lett.* 6, 217 (1978).
27. E. M. Anderson and V. A. Zilitis, *Opt. Spectrosc.* 16, 211 (1964).
28. M. Lapp and L. P. Harris, *J. Quant. Spectrosc. Radiat. Transfer* 6, 169 (1966).
29. D. R. Stull and G. C. Sinke, Thermodynamic Properties of the Elements, *Advances in Chemistry Series*, No. 18 (American Chemical Society, Washington, D.C., 1956).
30. W. H. Evans, R. Jacobsen, T. R. Munson, and D. D. Wagman, *J. Res. Nat. Bur. Stand.* 55, 83 (1955).
31. Thermcraft, Inc., P.O. Box 12037, Winston-Salem, NC 27107
32. C. B. Collins, F. W. Lee, J. A. Anderson, P. A. Vicharelli, D. Popescu and I. Popescu, *J. Chem. Phys.* 74, 1067 (1981).
33. M. Raab, G. Honing, W. Demtroder and C. R. Vidal, *J. Chem. Phys.* 76, 4370 (1980).
34. M. G. Raymer and J. Mostowski, *Phys. Rev. A* 24, 1980 (1981).
35. E. P. Ippen and C. V. Shank in Ultrashort Light Pulses, edited by S. L. Shapiro, *Topics in Applied Physics*, Vol. 18 (Springer-Verlag, New York, 1977) p. 88.
36. K. H. Drexhage, *Laser Focus* 9, 35 (1973).
37. R. L. Carmen, F. Shimizu, C. S. Wang and N. Bloembergen, *Phys. Rev. A* 2, 60 (1970); S. M. George and C. B. Harris, *Phys. Rev. A* 28, 863 (1983).
38. Experience has shown that the amplified pulse width scales with the input pulse width, but remains shorter. The amplified pulse energy

and bandwidth, however, remain approximately constant.

39. A. Laubereau and W. Kaiser, Rev. Mod. Phys. 50, 607 (1978).
40. J. Morellec, D. Normand, G. Mainfray and C. Manus, Phys. Rev. Lett. 44, 1394 (1980).
41. H. Bebb, Phys Rev. 149,25 (1966).

Chapter 4: Theory and Performance of a High Gain Picosecond Dye-  
Laser Amplifier

I. INTRODUCTION

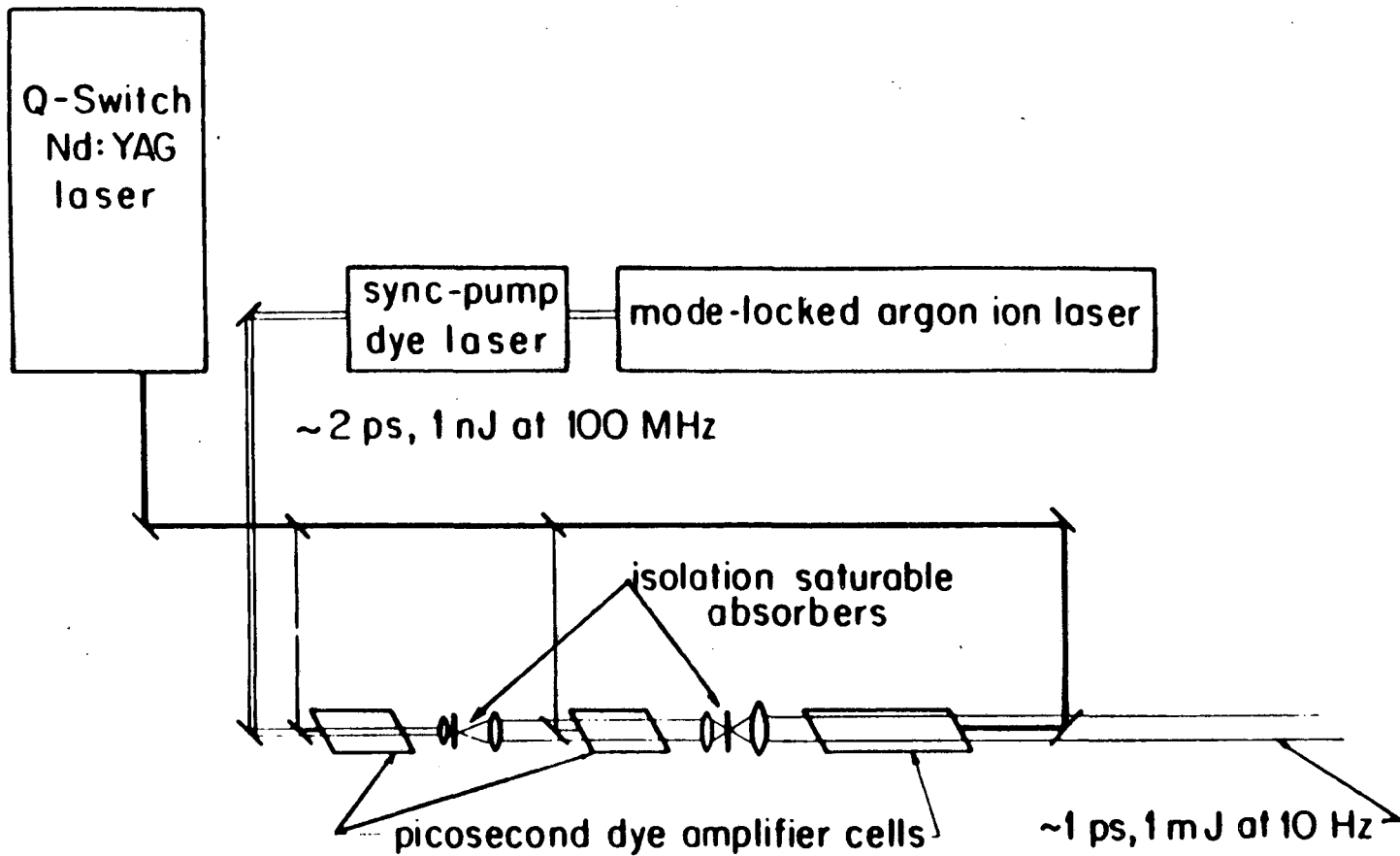
Laser pumped dye amplifiers are proving to be a very useful source of high power picosecond pulses in the visible region. In this chapter, a picosecond dye amplifier is described which provides a reliable source of high energy (1-2 mJ) pulses of ~1 ps pulse width, tunable from 560 nm to >610 nm. The design of the amplifier has been optimized to obtain maximum pulse energy and good spatial quality, with both short and long term energy stability which is routinely  $\pm 10\%$ . These features of the amplifier system, in combination with the ability to generate picosecond pulses in other wavelength regions by nonlinear optical techniques, have provided substantial improvements in the transient spectroscopy of reacting chemical systems (see Chapter 2). The high energy obtained has also contributed to progress in the generation of tunable picosecond pulses in the vibrational infrared region (Chapter 3).

The theory and experimental arrangement of effective high gain amplifiers for picosecond pulses have been described in several recent publications.<sup>1-5</sup> In the present work principles of high gain amplifier design are applied to optimize the output energy and stability. The results of both computer simulations and approximate equations which model the performance of individual amplifier cells are presented. The amplifier performance is then summarized.

A schematic of the dye-laser system appears in Fig. 1. The

continuous pulse train from a commercial synchronously pumped picosecond dye laser is amplified in three amplifier stages. Each stage consists of a circulating-dye cell which is optically pumped by a fraction of the pulse energy from an amplified, frequency-doubled, Q-switched Nd:YAG laser operating at 10 Hz. The pump duration of 15 ns is shorter than the period between the picosecond pulses so that one picosecond pulse is amplified with each pump pulse. In order to take advantage of the good beam quality of the pump laser, and to provide highest gain and ease of alignment, the cells are pumped longitudinally.<sup>4,5</sup> Between each amplifier stage, the picosecond pulse is focused into saturable absorber dye jets which reduce amplified spontaneous emission. The principles which form the basis for this design are discussed in Sec. II. The performance of the laser amplifier is summarized in Sec. III.

FIG. 1. Amplified picosecond dye-laser system. Double line - path of picosecond pulses, single line - path of pump pulse for the three stage dye-laser amplifier.



XBL 8312-6664A

Figure 1

## II. THEORY OF A HIGH GAIN PICOSECOND AMPLIFIER

### A. High Gain Amplifier - Multiple stages

In order to obtain an output power of ~1 gigawatt (1 mJ, 1 ps) in the amplified pulse, the ~0.1 nJ input pulse from the synchronously pumped dye laser must be amplified by a factor of  $\sim 10^7$ . A gain of this magnitude cannot be readily obtained in a single amplifier cell without the buildup of unacceptable levels of amplified spontaneous emission (ASE). The maximum practical gain from a single amplifier cell is determined by its geometry:<sup>6</sup>

$$G_{\max} = \frac{t_{\text{spont}}}{\tau} \cdot \frac{4L^2}{r^2}$$

where  $t_{\text{spont}}$  and  $\tau$  are the spontaneous emission and fluorescence lifetimes, and  $L$  and  $r$  are the length and radius of the amplifying region. Since  $\tau \approx t_{\text{spont}}$  in efficient laser dyes, a single dye laser amplifier cell with a gain of  $10^7$  must have  $L/r > 10^3$ . Since the cell diameter must be several millimeters to support an output pulse energy of 1 mJ, the length of a single cell amplifier would have to be several meters.

By contrast, several optically isolated amplifier cells can have progressively larger diameters. Narrow early cells provide high gain, and a wider final cell can provide pulse energy. The overall gain can be high with reasonable cell geometries. In the present system, optical isolation is accomplished with saturable absorber dyes, and the first stage must provide enough gain so the pulse can saturate the first

saturable absorber dye. This cell is operated near the small signal gain limit. The second cell is operated with strong signal saturation which stabilizes the pulse energy. The third cell determines the final output energy. The following subsections briefly discuss the design criteria applied to each of these cells.

### B. First Amplifier Stage - High Gain

To saturate the absorption in the first absorber dye jet, the focused picosecond pulse must pump a large fraction of the dye molecules into the nonabsorbing excited state. Since the recovery times of saturable absorbers such as malachite green and crystal violet are much longer than the 1-ps pulse width,<sup>7,8</sup> the absorber transmits when the number of incident photons exceeds the number of absorber molecules in the active region, giving a saturation energy:

$$E_{\text{sat}} = h\nu_{\text{sig}} \frac{A (-\ln T_0)}{\sigma_a}$$

where  $h\nu_{\text{sig}}$  is the energy of a signal photon

$A$  is the area of the amplified pulse at the absorber dye jet

$T_0$  is the small signal transmission of the absorber

$\sigma_a$  is the dye absorption cross section in its ground state, at the signal wavelength.

For a spot diameter of 60  $\mu\text{m}$ , and assuming  $T_0 = 1 \times 10^{-5}$ ,  $\sigma_a = 1 \times 10^{-16} \text{ cm}^2$ , then  $E_{\text{sat}} = 1 \text{ } \mu\text{J}$ . Thus, with an input pulse energy of 0.1 nJ, the first amplifier cell must have a gain of  $\sim 10^4$ .

With a dye concentration  $N = 1 \times 10^{16} \text{ cm}^{-3}$ , an emission cross section

$\sigma_e = 10^{-16} \text{ cm}^2$  at the signal wavelength, and assuming that all of the molecules can be pumped into the excited state, a 10 cm amplifier cell would have a small signal gain  $G_0 = \exp(10 \sigma_e N) = 10^5$ . The actual gain of the signal pulse is determined by the extent to which the pump can compete with ASE to hold dye molecules in the upper laser level, and the extent of signal saturation in the amplifier cell.

In order to investigate the pump and ASE interactions in a longitudinally pumped amplifier cell, a numerical simulation was made of an amplifier cell with 0.1 cm radius and 10 cm length, pumped at 532 nm. The dye parameters were chosen to match those of rhodamine 590 (Table I), one of several efficient laser dyes in the yellow-red. The standard rate equations for dye-molecule lasers were used.<sup>3,5,9,10</sup> The cell was assumed to reach a steady state condition during the pump pulse, and forward and backward waves of ASE were considered. Such simulations have previously been applied to transversely pumped amplifier cells,<sup>9,10</sup> and to their use in picosecond pulse amplification.<sup>2,3</sup> The present simulation provides insight into the somewhat more complicated interactions between the collinear pump and ASE fluxes in the longitudinally pumped amplifier cell. The simulation is described in more detail in Appendix A of this chapter.  $N$ ,  $N_0$ , and  $N_1$  are the total, ground, and excited state dye concentrations ( $\text{cm}^{-3}$ ), and  $\sigma_a$  and  $\sigma_e$  are the absorption and emission cross sections ( $\text{cm}^2$ ) at the signal wavelength.

The concentration fraction of excited state molecules,  $N_1/N$ , obtained in the simulation is shown at three dye concentrations and several pump intensities in Fig. 2. At a dye concentration of  $3 \times 10^{15} \text{ cm}^{-3}$ , the small signal gain does not exceed 100, ASE does not affect the

excited state population, and nearly 100% of the molecules can be held in the excited state with a modest pump intensity of  $4 \times 10^{24} \text{ s}^{-1} \text{ cm}^{-2}$ , equivalent to a 0.5 mJ, 10 ns pump pulse into the  $0.03 \text{ cm}^2$  cross sectional area of the cell. As the dye concentration is increased to reach higher gain, ASE depletes the excited state population, particularly at the end of the cell where the pump exits. At a dye concentration of  $3 \times 10^{16} \text{ cm}^{-3}$ , this effect is severe enough that the pump cannot saturate the dye population, and the effective active region is reduced to  $\sim 4 \text{ cm}$ .

At the intermediate concentration of  $1 \times 10^{16} \text{ cm}^{-3}$ , high gain is obtained without excessive ASE. To evaluate the operation of the cell at this concentration, the small signal gain,  $G_0$ , can be obtained:

$$G_0 = \exp \left[ \sigma_e \int_0^L N_1(z) dz - \sigma_a \int_0^L N_0(z) dz \right] \quad (1)$$

The actual gain,  $G_{\text{act}}$ , is much lower due to signal saturation, and depends on signal input energy. When the cell is at steady state, and the signal pulse is short, the actual gain can be calculated as an initial value problem, giving:<sup>12,13</sup>

$$G_{\text{act}} = \frac{A}{c_0} \left[ 1 + G_0 \left( e^{c_0/A} - 1 \right) \right] \quad (2)$$

where  $A$  is the cross sectional area of the amplifier, and  $c_0$  is related to the input signal energy,  $E_{\text{sig}}$ :

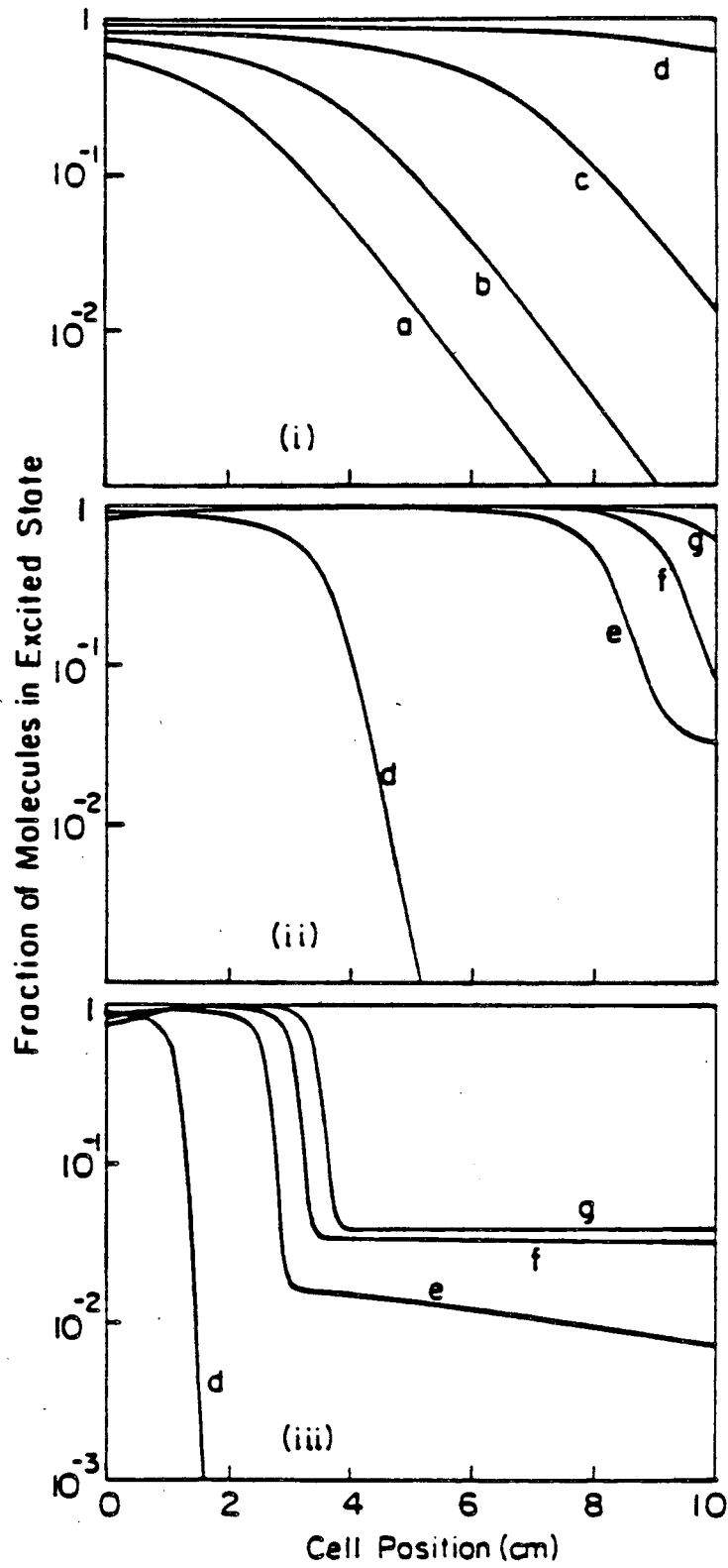
$$c_0 = \frac{E_{\text{sig}}}{h\nu_{\text{sig}}} (\sigma_e + \sigma_a)$$

The forward ASE intensity, which is of concern in the operation of later stages, is also obtained directly from the simulation. The small signal gain, the actual gain for 0.1-nJ and 1- $\mu$ J input signal pulses, and the ASE intensity at several pump intensities are listed in Table II at the dye concentration  $1 \times 10^{16} \text{ cm}^{-3}$ .

The results indicate that such a longitudinally pumped cell compares very favorably as a high gain amplifier with transversely pumped cells.<sup>2,3</sup> At reasonable pump intensities of  $2 \times 10^{25}$  or  $8 \times 10^{25} \text{ sec}^{-1} \text{ cm}^{-2}$  (2 or 8 mJ in a 10 ns pulse), the actual gain for a 0.1-nJ signal pulse is calculated to be  $1-10 \times 10^5$ , exceeding the 1- $\mu$ J output energy needed to saturate the first absorber dye. The ratio of the output picosecond pulse intensity to that of the ASE is 500-1500 (Table IIB) at these pump intensities, for a 0.1-nJ input pulse. The energy of the ASE is of course much greater than the picosecond pulse energy, because the ASE lasts as long as the pump pulse ( $\sim 10$  ns). This points up the need to remove the ASE before entering subsequent amplifier cells.

The simulation also indicates that the assumption of steady state conditions is valid. For a dye concentration of  $1 \times 10^{16} \text{ cm}^{-3}$  and pump intensities of  $2-8 \times 10^{25} \text{ s}^{-1} \text{ cm}^{-2}$ , the amount of energy stored in the dye cell represents 2-3 ns of the pump. This is shortened considerably from the dye fluorescence lifetime of 9 ns because of the depleting effect of strong ASE. The response time of the cell is fast enough to track the intensity of a 10-15 ns pump pulse. This also demonstrates that the stability of the pump process depends upon the peak intensity of the pump pulse rather than the integrated energy.

FIG. 2. Fraction of dye molecules in the excited state,  $N_1/N$ , as a function of cell position, from numerical simulation of a longitudinally pumped 0.2 cm diameter, 10 cm long amplifier cell at steady state. Dye parameters are for rhodamine 590 and pump is at 532 nm. Dye concentration ( $\text{cm}^{-3}$ ): i)  $3 \times 10^{15}$ ; ii)  $1 \times 10^{16}$ ; iii)  $3 \times 10^{16}$ . Pump intensity ( $\text{s}^{-1} \text{cm}^{-2}$ ): a -  $5 \times 10^{23}$ , b -  $1 \times 10^{24}$ , c -  $2 \times 10^{24}$ , d -  $4 \times 10^{24}$ , e -  $2 \times 10^{25}$ , f -  $8 \times 10^{25}$ , g -  $4 \times 10^{26}$ .



XBL 858-6545

Figure 2

TABLE I. Dye parameters for rhodamine 590 as used in the numerical simulation of a dye amplifier cell (see Appendix A).

<u>Parameter</u>	<u>Value</u>	<u>Ref.</u>
$\sigma_p$ (532 nm)	$3.9 \times 10^{-16} \text{ cm}^2$	11
$\sigma_a$ (565 nm)	$7.6 \times 10^{-18} \text{ cm}^2$	11
$\sigma_e$ (565 nm)	$1.83 \times 10^{-16} \text{ cm}^2$	11
$k$ ( $=1/\tau_f$ )	$1.37 \times 10^8 \text{ s}^{-1}$	11
E	0.3	9,10

TABLE II. Results of the numerical simulation of a dye amplifier cell for a dye concentration of  $1 \times 10^{16} \text{ cm}^{-3}$ , at several pump intensities.

A. Small signal gain,  $G_0$ ; and actual gain,  $G_{\text{act}}$ , for several input pulse energies.

Pump Intensity <sup>a</sup> ( $\text{s}^{-1} \text{ cm}^{-2}$ )	$G_0$	$G_{\text{act}}$		
		Input Signal Pulse Energy (J)		
		$10^{-10}$	$10^{-8}$	$10^{-6}$
$4 \times 10^{24}$	120	120	118	64
$2 \times 10^{25}$	$9.2 \times 10^5$	$5.4 \times 10^5$	$2.8 \times 10^4$	535
$8 \times 10^{25}$	$8.2 \times 10^6$	$1.6 \times 10^6$	$4.0 \times 10^4$	660
$4 \times 10^{26}$	$3.3 \times 10^7$	$2.4 \times 10^6$	$5.0 \times 10^4$	750

B. Intensity of forward ASE; and signal output intensity for a 1-ps pulse, at several input pulse energies.

Pump Intensity ( $\text{s}^{-1} \text{ cm}^{-2}$ )	Forward ASE Intensity ( $\text{s}^{-1} \text{ cm}^{-2}$ )	Output Signal Intensity ( $\text{s}^{-1} \text{ cm}^{-2}$ )		
		Input Signal Pulse Energy (J)		
		$10^{-10}$	$10^{-8}$	$10^{-6}$
$4 \times 10^{24}$	$6.5 \times 10^{20}$	$1.1 \times 10^{24}$	$1.1 \times 10^2$	$6.1 \times 10^{27}$
$2 \times 10^{25}$	$3.5 \times 10^{24}$	$5.2 \times 10^{27}$	$2.7 \times 10^{28}$	$5.1 \times 10^{28}$
$8 \times 10^{25}$	$3.0 \times 10^{25}$	$1.5 \times 10^{28}$	$3.8 \times 10^{28}$	$6.3 \times 10^{28}$
$4 \times 10^{26}$	$1.3 \times 10^{26}$	$2.3 \times 10^{28}$	$4.7 \times 10^{28}$	$7.1 \times 10^{28}$

a) Pump Intensity at 532 nm:  $10^{25} \text{ s}^{-1} \text{ cm}^{-2} = 3.8 \text{ MW cm}^{-2}$

b) Signal and ASE Intensity at 595 nm:  $10^{25} \text{ s}^{-1} \text{ cm}^{-2} = 3.3 \text{ MW cm}^{-2}$

### C. Second amplifier stage - Energy Stability

The second amplifier stage is designed to stabilize the signal pulse energy, while providing enough gain to allow efficient energy extraction in the final amplifier cell. This is accomplished with a cell identical to the one in the first stage. Since the input energy to the second stage is close to  $1 \mu\text{J}$ , the pulse saturates the gain. Table II shows that for a signal input energy of  $1 \mu\text{J}$ , the gain is predicted to be  $5-6 \times 10^2$ , while for an input of only  $0.01 \mu\text{J}$ , the gain is  $3-4 \times 10^4$ . Thus, even when the input changes by a factor of 100, the output energy changes very little. This provides a stable input to the final amplifier stage, with enough power to efficiently extract the stored energy of the final cell. In addition, only modest pump intensity is needed, so most of the pump energy can be used in the final amplifier stage.

### D. Final Amplifier Stage - Energy Storage

The final output energy of the amplifier system is determined primarily in the final amplifier stage. The important features of both energy storage and extraction in the final amplifier cell can be illustrated using an approximate expression for the small signal gain,  $G_0$ , of a longitudinally pumped amplifier cell. If the gain constant is assumed to be spatially uniform, the effects of ASE depletion can be approximated by replacing the dye fluorescence lifetime with a shorter, effective lifetime.<sup>5</sup> The approximation of a spatially uniform gain constant can be compared to the simulation results in Fig. 2ii, for a

longitudinally pumped amplifier cell. The excited state population (and gain) is nearly uniform under the conditions where the cell provides good amplification (curves e,f), so the approximation should be useful.

The approximate expression for  $G_0$  is (including a term missing in Ref. 5):

$$G_0 = c_1 \exp \left\{ \frac{c_2}{\left[ 1 + \frac{2D}{3L} \ln G_0 + \frac{A G_0}{2\pi L^2} (\ln G_0)^{-3/2} \left( 1 + \frac{4}{\ln G_0} + \frac{18}{(\ln G_0)^2} \right) \right]} \right\} \quad (3)$$

$$\text{where } c_1 = (1-f)^{(\sigma_p/\sigma_a)}$$

$$c_2 = \frac{\phi_p \tau \sigma_e \sigma_p f}{\sigma_p}$$

$f$  = fraction of pump energy absorbed in the cell

$\phi_p$  = pump intensity ( $s^{-1} \text{ cm}^{-2}$ ).

$\tau$  = dye fluorescence lifetime (s).

$\sigma_p$  = dye absorption cross section at the pump wavelength ( $\text{cm}^2$ ).

$\sigma_a, \sigma_e$  = dye absorption and emission cross sections at the signal (and peak ASE) wavelength ( $\text{cm}^2$ ).

$L, D, A$  = length, diameter, and area of the amplifier cell.

To obtain the actual gain, Eq. (2) is combined with Eq. (3). The dye parameters assumed for this calculation were those of rhodamine 640 (Table III), amplifying a signal pulse at 595 nm. The pump energy was assumed to be 200 mJ in a 10 ns pulse at 532 nm. Because of the approximations in Eq. (3), this method will not predict accurate output energies. In particular, the calculation predicts output energies

several times too high since it ignores losses from triplet molecules and orientational gain saturation.<sup>5</sup> However, the results provide an approximate picture of the competing effects which control the final output energy.

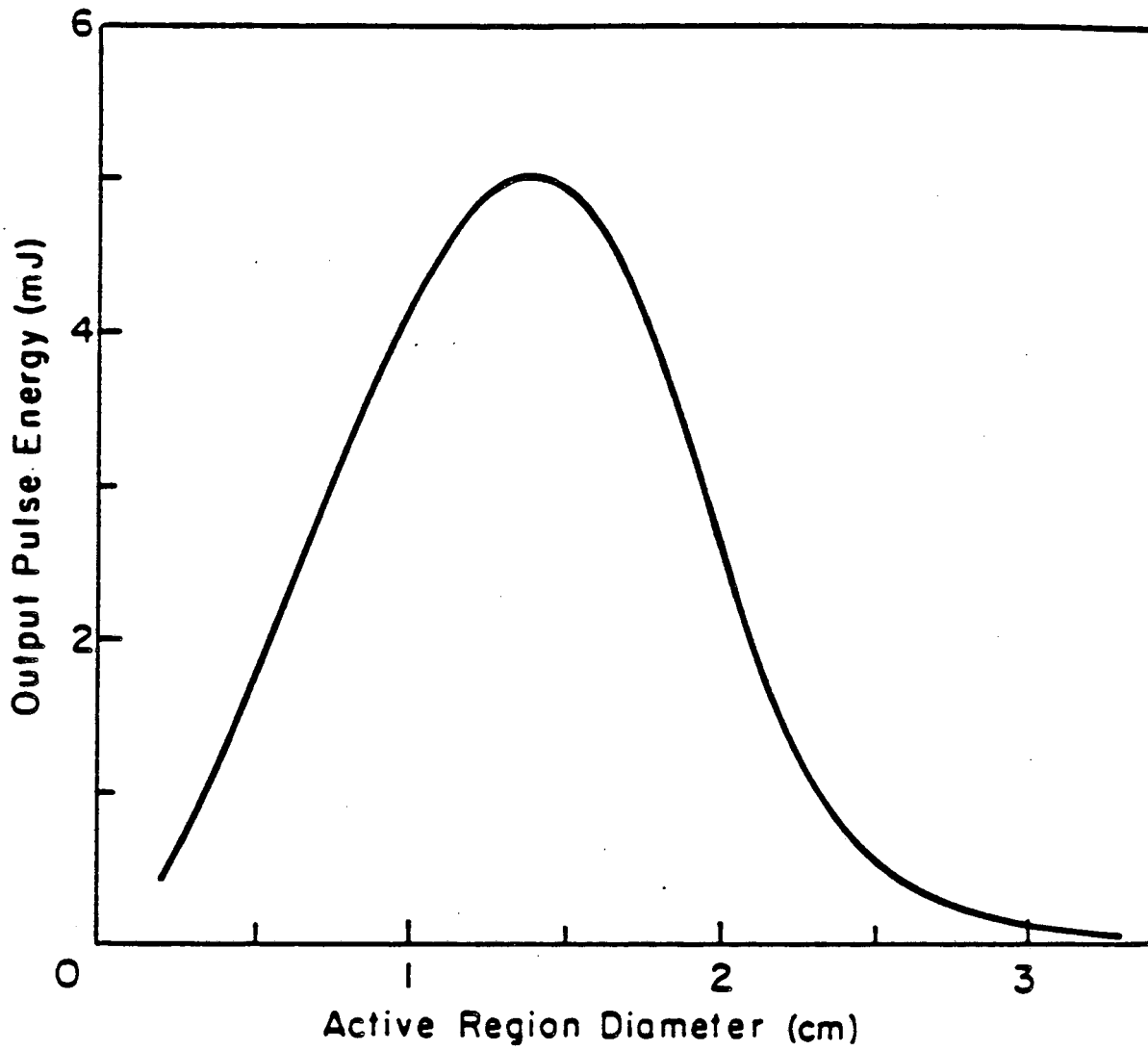
For a fixed cell length, and assuming a fixed fraction of the pump absorbed (Table III), the actual gain is found to peak at an optimum cell diameter for each input signal energy (Fig. 3). This is due to competing effects. At small diameters, the dye concentration must be high to absorb all of the pump energy in a small volume. The small signal gain is large, resulting in strong ASE which depletes the stored energy. At larger diameters, the dye concentration is lower, resulting in lower gain and less ASE, so that energy storage is increased. If the diameter is too large, however, the input signal intensity decreases and becomes too small to saturate the laser transition, so energy extraction is poor. At the optimum diameter, a compromise is reached between energy storage and energy extraction.

The calculated dependence of the optimum cell diameter and the resulting extracted energy on both the cell length and the input signal energy are plotted in Fig. 4. The predicted extracted energy is strikingly insensitive to both the cell length and the input signal intensity. For instance, doubling the cell length from 10 cm to 20 cm at any input signal energy increases the extracted energy by only 30%. Changing the input energy by a factor of 10, from 10  $\mu$ J to 100  $\mu$ J, changes the extracted energy by 60%. Thus, at a fixed pump power, the extracted energy is determined mostly by choosing a reasonable diameter for the final cell. The optimum diameter is predicted to be 1-2 cm, assuming practical cell lengths of 10-20 cm and reasonable input signal

energies of 10-100  $\mu$ J.

The weak dependence of the output energy on the input signal energy to the final stage illustrates the advantage of concentrating most of the pump energy at the final cell. If additional pump energy were used to pump the second stage, or even an intermediate stage in a four cell system, the increased input signal energy at the final cell would have little effect on the output. The loss of pump energy at the final cell might in fact decrease the overall performance. This is particularly true because the signal pulse energy is decreased by a factor of 5 between stages due to losses in the saturable absorber dye and optics.

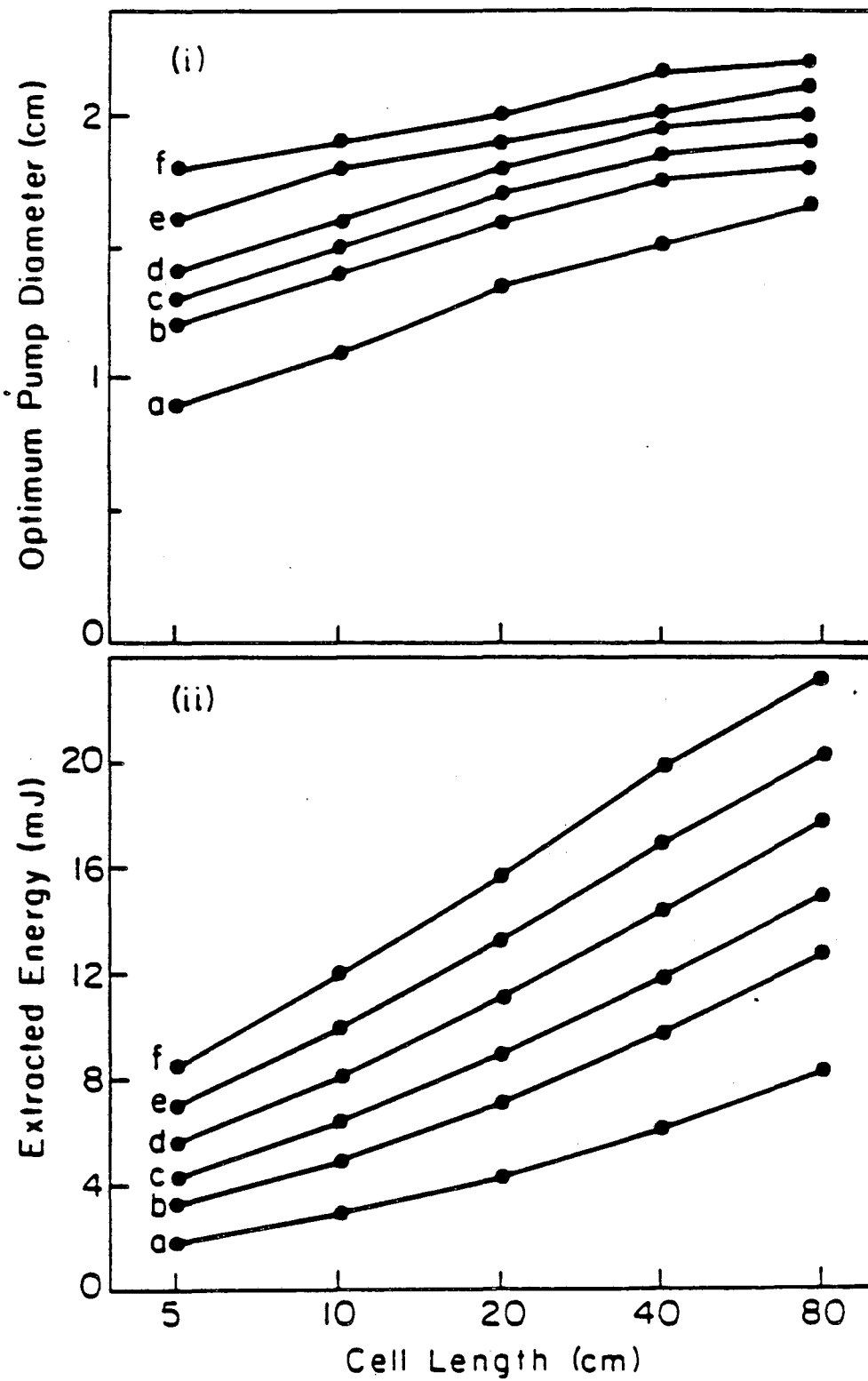
FIG. 3. Energy extracted from a 10 cm amplifier cell as a function of the active region (pumped) diameter, as calculated using Eqs. (2) and (3). Dye and operating parameters are fixed as in Table 3. Signal diameter is assumed to match pump diameter. Input signal energy is 10  $\mu$ J.



XBL 858-6547

Figure 3

FIG. 4. Calculated optimum diameter and resulting extracted energy of the final amplifier cell, using Eqs. (2) and (3), as a function of cell length and incident signal pulse energy. The dye and operating parameters are as listed in Table 3. i. Cell diameter for maximum extracted energy. ii. Extracted energy (output energy with input energy subtracted) at optimum cell diameter. Input pulse energies ( $\mu\text{J}$ ): a - 1, b - 10, c - 30, d - 100, e - 300, f - 1000. Predicted output energy is too high, but trends should be accurate (see text).



LBL 850-6548

Figure 4

TABLE III. Parameters used in the calculation of the energy extraction in the final amplifier stage. The dye parameters are for rhodamine 640.

<u>Parameter</u>	<u>Value<sup>a</sup></u>
signal wavelength	595 nm
pump wavelength	532 nm
pump power	$3.5 \times 10^{25} \text{ s}^{-1}$ (note b)
f = fraction of pump absorbed	0.9
$\sigma_p$	$1.2 \times 10^{-16} \text{ cm}^2$
$s_a$	$7.72 \times 10^{-17} \text{ cm}^2$
$\sigma_e$	$3.7 \times 10^{-16} \text{ cm}^2$
$\tau$	$4.3 \times 10^{-9} \text{ s}$

<sup>a</sup> Dye parameters for rhodamine 640 are taken from Ref. 5.

<sup>b</sup> Pump power is 13 MW, equivalent to 200 mJ in a 15 ns pulse.

### E. Optical Isolation of Amplifier Stages

If the ASE is not to be amplified strongly through the amplifier system, the small signal transmission of the absorber dye jets must be approximately the inverse of the small signal gain in each amplifier cell. For small signal gains of  $10^5$  (see Table II), the absorber transmission must therefore be approximately  $10^{-5}$ . For a dye absorption cross section around  $2 \times 10^{-16} \text{ cm}^2$  (malachite green at 580 nm), the area density of dye molecules must be  $\sim 5 \times 10^{16} \text{ cm}^{-2}$ .

To saturate the absorber, the picosecond pulse must contain  $> 5 \times 10^{16}$  photons  $\text{cm}^{-2}$ . This requires a small beam diameter, so the picosecond pulse is focused into a thin jet stream of absorber dye in ethylene glycol. With a jet thickness of 0.01 cm, the necessary dye concentration of  $5 \times 10^{18} \text{ cm}^{-3}$  (10 millimolar) is within the solubility range of malachite green or crystal violet dye. In a 1-ps pulse, the intensity must exceed  $5 \times 10^{28} \text{ s}^{-1} \text{ cm}^{-2}$ , or  $10^{10} \text{ W cm}^{-2}$ , which is high enough to cause problems from nonlinear optical effects. This will be seen to limit the saturated transmission in the dye jets to 20% (see Sec. IIIA).

Saturable absorbers sharpen the leading edge of the picosecond pulse, counteracting the broadening associated with gain saturation in the later amplifier stages.<sup>5</sup> Pulse durations of 1 ps or less can be maintained, in contrast with pulse broadening occurring in amplifier systems using other optical isolation techniques.

## F. Summary of Amplifier Theory

Several optically isolated amplifier cells with increasing diameters are needed to obtain an overall signal gain of  $10^6$  to  $10^7$  and an output energy of 1 mJ in a picosecond pulse. An approximate analysis of the energy extraction process shows that the final output energy is only weakly dependent upon input energy at the final cell. Therefore, most of the pump energy should be concentrated in the final amplifier stage for efficient conversion of pump to signal energy. The design of the first stage is constrained by the need to saturate the first absorber dye. A numerical analysis of the performance of the first cell shows that a design with 0.2 cm diameter and 10 cm length should provide sufficient ( $\sim 10^4$ ) actual gain, using a small fraction of the available pump energy. An identical second cell should stabilize the signal pulse energy due to strong signal saturation, while providing enough gain to allow efficient energy extraction in the final cell.

## II. PICOSECOND DYE AMPLIFIER PERFORMANCE

### A. Output Energy and Tuning Curves

A three stage picosecond pulse amplifier was constructed based upon the principles outlined in the previous section (Fig. 1). The geometry and typical operation of each of the three amplifier stages are summarized in Table IV.

The first two amplifier cells have similar geometries and are each pumped by a small fraction of the total pump pulse energy. The typical experimentally measured gains of the first two cells may be compared to the calculated gains listed in Table II. The calculated gain is sensitive to the dye concentration, especially in the near-exponential small signal limit of the first cell. However, the measured performance is qualitatively similar to the predictions, with a first cell gain approaching  $10^4$ , and a saturated second cell gain of several hundred.

Based on the considerations discussed in part IID, the final amplifier cell is pumped by most of the available energy, and is designed with a larger diameter, to maximize the final output energy. Although the calculations suggest that even larger (1-2 cm) diameters might improve the output energy (Fig. 4), such changes did not measurably improve the performance. In agreement with the calculations, the output energy also showed little change when the final cell length was changed from 10 cm to 20 cm; cells longer than 20 cm were not tested.

The output energy tuning curves obtained with a series of amplifier dyes in both water and methanol solutions are illustrated in Fig. 5.

Output energies above 1 mJ are obtained across most of the region from 565 nm to 605 nm. Additional tuning to longer wavelengths should be possible using other dyes.<sup>5</sup> The tuning curves are somewhat narrower than those obtained with the same dyes in nanosecond dye lasers. This effect probably results from the very high exponential gain which is necessary in the first cell; even moderate reductions in the gain coefficient at wavelengths off the peak of the tuning curve may result in a pulse energy which is too small to saturate the first dye jet. The output energies are approximately consistent with, but somewhat lower than, the predictions of Section IID. As noted in that section, the optimistic predictions may result from the neglect of triplet losses and orientation dependent gain saturation<sup>5</sup>.

The output pulse has a smooth near-Gaussian spatial beam profile which matches the profile of the pump Nd:YAG laser. Turbulence in the circulating dye cells does, however, create small scale variations in the beam profile, which are more severe in methanol solutions than in water solutions. Therefore, most experimental work was carried out using water solutions in the amplifier system, although the output energies are higher in methanol solutions,.

The output energy had an r.m.s. deviation of  $\pm 10\%$  shot-to-shot. Fluctuations in the peak power of the pump pulse appeared to be the primary source of the fluctuations in the output energy. As expected for a strongly saturated system, the output energy was not sensitive to the input at the first cell; at the peaks of the tuning curves, a factor of two change in input energy resulted in less than a 10% change in output.

While the performance of the dye amplifier cells was generally as

expected, the saturable absorber dye jets provided only ~20-25% transmission, which is lower than previously reported.<sup>5</sup> The transmission could not be increased by increasing the intensity since, when the jet was placed too close to the focal point, the intensity of the focused pulse was sufficient to cause sparking, with transmission reductions and breakup of the beam profile. The sparking occurred at the same intensity without dye in the jet, and was attributed to optical breakdown in the ethylene glycol solvent.

Although such losses have not been reported previously, they occur at intensity levels where nonlinear optical effects may be expected. The saturable absorber dye molecules must be present at an area density of  $\sim 5 \times 10^{16} \text{ cm}^{-2}$  to provide a small signal transmission of  $10^{-4}$  (assuming an absorption cross section of  $2 \times 10^{-16} \text{ cm}^2$ ). For a pulse which is shorter than the ground state recovery time of the saturable absorber, the integrated flux must therefore exceed  $5 \times 10^{16} \text{ cm}^{-2}$  to saturate the dye. In a 1-ps pulse, the intensity must exceed  $10^{10} \text{ W cm}^{-2}$ , a level at which nonlinear effects such as self-focussing become important. Other effects such as excited state absorption in the dyes may also play a role.<sup>8</sup> The peak transmission was similar in both malachite green and crystal violet absorber dyes, however, suggesting that there may be intrinsic limitations to the transmission of short pulses resulting from the high intensities attained.

FIG. 5. Output pulse energy as a function of wavelength. Synchronously pumped dye laser was operated with rhodamine 590 at all wavelengths. Amplifier dyes: a - rhodamine 590, b - rhodamine 610, c - Kiton Red 620, d - rhodamine 640. ● , methanol solutions; ▲, water solutions (no surfactants).

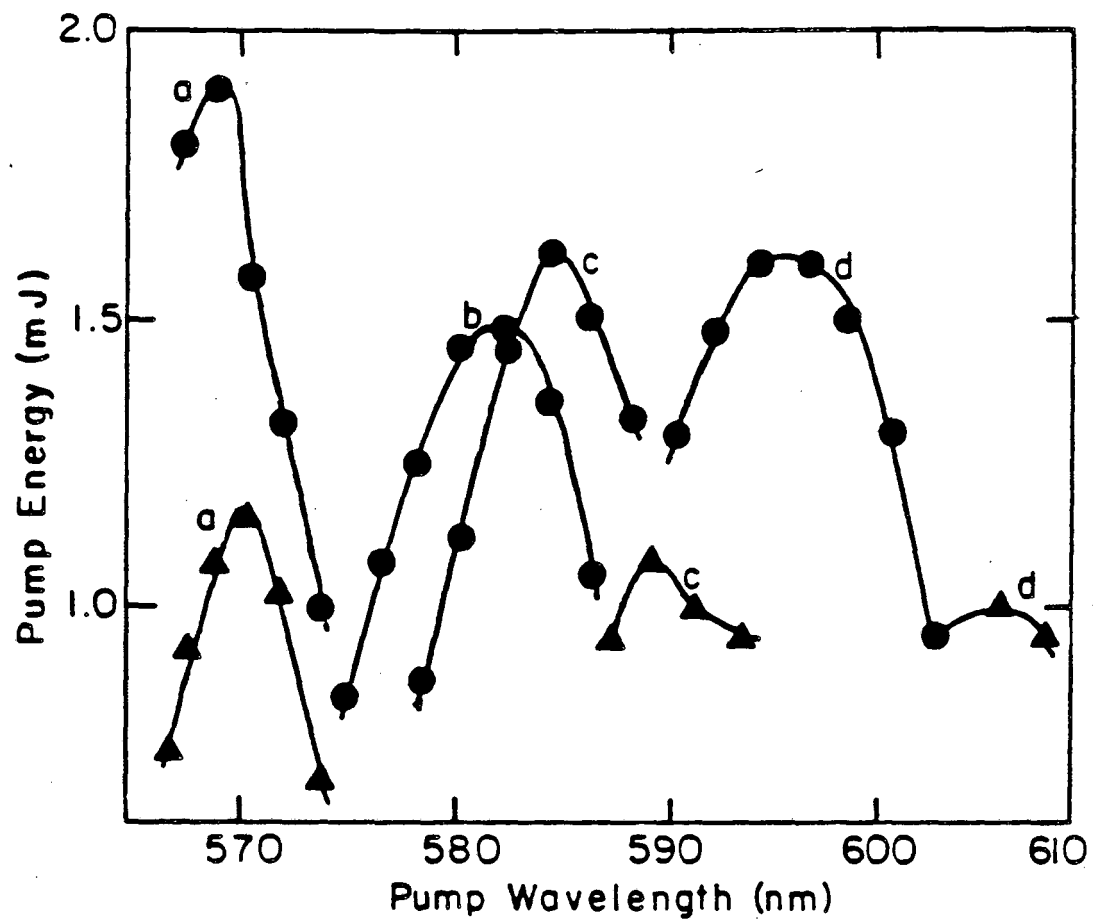


Figure 5

Table IV: Design and Typical Performance of Dye Amplifier Stages

<u>Stage</u>	<u>Cell Length (cm)</u>	<u>Pump Energy (mJ)</u>	<u>Pump Diameter (cm)</u>	<u>Signal Input Energy (<math>\mu</math>J)</u>	<u>Signal Output Energy (<math>\mu</math>J)</u>	<u>Gain</u>
1st	10	10	0.15	$2 \times 10^{-4}$	1	5000
2nd	10	15	0.22	0.2	60	300
3rd	20	210	0.6	12	1000	80

## B. Pulse width and spectrum

The spectrum and pulse width of the input and output pulses were investigated with either a one-plate or a two-plate birefringent tuning filter in the synchronously pumped dye laser. Both average and single-pulse spectra of the amplified pulses could be measured using an optical multichannel analyzer and monochromator. Only the average spectrum of the input pulses could be readily measured, because of the high repetition rate and low pulse energy. The pulse widths were measured by standard, zero-background autocorrelation measurements using frequency-doubling crystals.

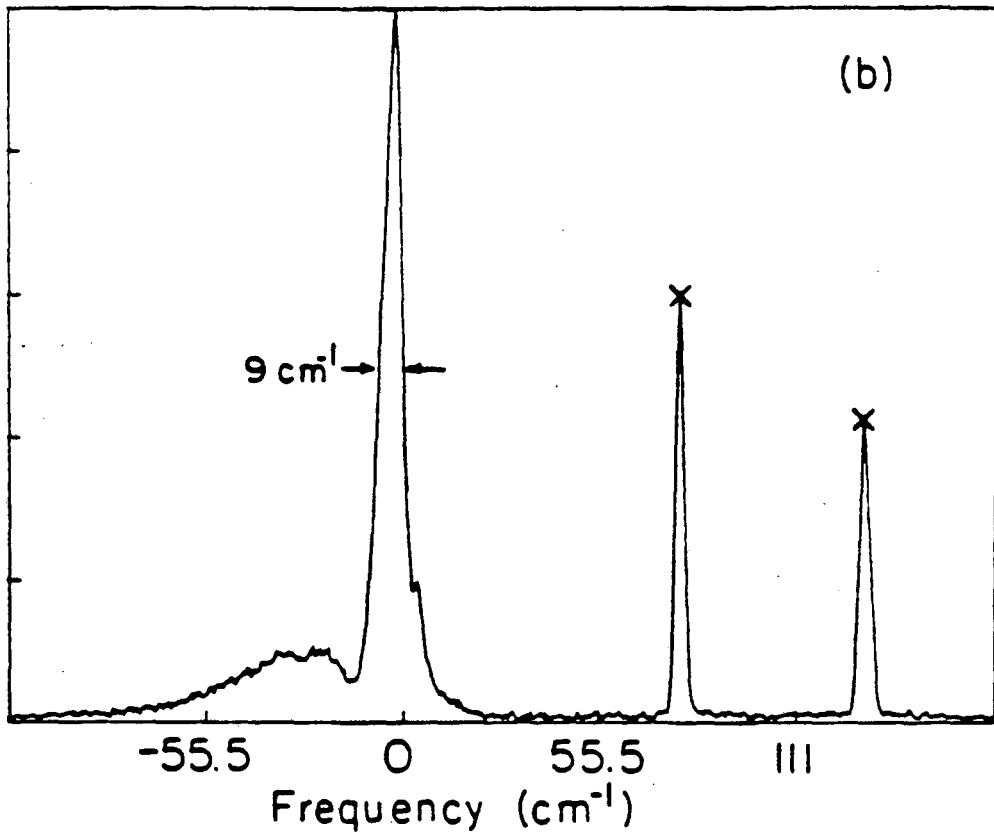
The amplified pulses had an autocorrelation width that was somewhat smaller than that of the input pulses, especially in the wings. This effect has been predicted for similar amplifier systems, because of pulse shortening in the saturable absorber dyes.<sup>5</sup> The output autocorrelation widths were 1.1 and 1.5 ps FWHM with 1-plate and 2-plate tuning filters, respectively. These represent pulse widths of 0.73 and 1.0 ps, respectively, if a  $\text{sech}^2$  pulse shape is assumed.

The best spectral performance from the laser system was obtained with a two-plate birefringent filter in the synchronously pumped dye laser. The average spectrum at the output was broadened slightly from the input, to an  $18 \text{ cm}^{-1}$  full width at half maximum (FWHM). However, part of the spectral width was due to pulse-to-pulse shifts in the wavelength maximum. The average single pulse bandwidth was  $11 \text{ cm}^{-1}$ . Assuming a 1.0-ps pulse width, this gives a bandwidth product of 0.33, which compares very well with 0.32 for a bandwidth-limited  $\text{sech}^2$  pulse shape.<sup>14</sup> In addition, the output pulse had a low intensity shoulder to

the long wavelength side of the spectrum, which only appeared in the final amplifier cell. This shoulder probably results from self phase modulation due to the high intensity reached in the final amplifier cell (Fig. 6).

The pulse-to-pulse shifts in the wavelength maximum appeared to arise in the synchronously pumped dye laser. With a two-plate tuning filter, the shifts resulted in a moderate broadening of the average spectrum which was not considered a problem for most experiments. When a 1-plate tuning filter was used, the average spectrum broadened to 40-50  $\text{cm}^{-1}$  and the spectra of single amplified pulses showed substructure which was not stable pulse-to-pulse. Since the pulse width did not shorten substantially with the 1-plate filter, the pulses were no longer bandwidth limited. In order to maintain a well-defined spectrum, the experiments described in this thesis were all carried out using a 2-plate tuning filter in the synchronously pumped dye laser. Further details of the spectral and temporal characterization of the amplified picosecond pulses may be found in Ref. 15.

FIG. 6. Spectrum of a single amplified pulse after the final amplifier stage, with a 2-plate birefringent tuning filter in the synchronously pumped dye laser. The two peaks at shorter wavelength are calibration lines from a neon lamp.



XBL 858-6565

Figure 6

## IV. CONCLUSION

The theory and performance of a high gain ( $\sim 10^7$ ) dye amplifier for picosecond pulses have been described. Multiple, optically isolated amplifier stages with increasing diameters are necessary to reduce amplified spontaneous emission and to maximize the output energy. Saturable absorber dyes provide the optical isolation and counter the pulse broadening effects of gain saturation in the later amplifier stages. A numerical simulation of longitudinally pumped amplifier cells shows that either high gain ( $\sim 10^4$ ) or stabilizing gain saturation can be attained, depending on the signal input energy. The operation of the first two cells in the amplifier approximates these two limits. An approximate calculation of energy extraction in the final cell demonstrates that most of the pump energy should be concentrated in this cell, with a pump diameter substantially larger than the early cells.

The amplified picosecond laser constructed on the principles outlined provides a stable, high energy source for transient spectroscopic measurements. With a series of amplifier dyes, the output energy is greater than 1 mJ across most of the tuning region from 565 nm to 605 nm. Short and long term energy stability are  $\pm 10\%$ . The best combination of an output pulse width of 1.5 ps and a pulse spectral width of  $11 \text{ cm}^{-1}$  provides a bandwidth product of 0.33, which is close to the theoretical product of 0.32 for a bandwidth limited  $\text{sech}^2$  pulse shape.

## Appendix A: Numerical Simulation of a Longitudinally Pumped Dye Cell

Assuming that the ASE is nearly monochromatic and consists of forward and backward travelling waves with fluxes  $\phi^+(z)$  and  $\phi^-(z)$ , the standard local rate equations for a laser-pumped dye cell are:<sup>9,10</sup>

$$\frac{\partial N_1}{\partial t} = N_0 (\sigma_p \phi_p + \sigma_a \phi) - N_1 (k + \sigma_e \phi) \quad (4)$$

$$\frac{\partial \phi_p}{\partial z} = -\sigma_a \phi_p N_0 \quad (5)$$

$$\frac{\partial \phi^\pm}{\partial z} = \pm [ (\sigma_e \phi^\pm + b) N_1 - \sigma_a \phi^\pm N_0 ] \quad (6)$$

$$N = N_0 + N_1 \quad (7)$$

$$\phi = \phi^+ + \phi^- \quad (8)$$

where  $N_0$  and  $N_1$  are the concentrations of ground and excited state molecules ( $\text{cm}^{-3}$ ).

$\phi_p$ ,  $\phi^+$ , and  $\phi^-$  are the fluxes of pump, and forward and backward ASE ( $\text{s}^{-1}\text{cm}^{-2}$ )

$\sigma_p$  is the dye absorption cross section at the pump wavelength ( $\text{cm}^2$ ).

$\sigma_a$  and  $\sigma_e$  are the absorption and emission cross sections at the ASE wavelength ( $\text{cm}^2$ )

$N_0$ ,  $N_1$ ,  $\phi_p$ ,  $\phi^+$ ,  $\phi^-$ , and  $\phi$  are functions of  $z$  and  $t$ .

172

$b(z) = \frac{g(z) E}{\tau}$  is the rate of spontaneous emission into ASE ( $1/\tau$  is the fluorescence rate,  $g(z)$  is a geometric factor, and  $E$  is the effective emission cross section into the ASE bandwidth).

At steady state,  $\partial N_1 / \partial t = 0$ , and the equations may be rewritten:

$$N_1(z) = N \left( 1 + \frac{k + \sigma_e \phi(z)}{\sigma_p \phi_p(z) + \sigma_a \phi(z)} \right)^{-1} \quad (9)$$

$$N_0(z) = N \left( 1 + \frac{\sigma_p \phi_p(z) + \sigma_a \phi(z)}{k + \sigma_e \phi(z)} \right)^{-1} \quad (10)$$

$$\frac{\partial \phi_p(z)}{\partial z} = -\sigma_p \phi_p(z) N \left( 1 + \frac{\sigma_p \phi_p(z) + \sigma_a \phi(z)}{k + \sigma_e \phi(z)} \right)^{-1} \quad (11)$$

$$\frac{\partial \phi^\pm(z)}{\partial z} = \pm \left[ (\sigma_e \phi^\pm(z) + b(z)) N_1(z) - \sigma_a \phi^\pm(z) N_0(z) \right] \quad (12)$$

where  $\phi(z) = \phi^+(z) + \phi^-(z)$

By substituting Eqs. (9) and (10) into Eq. (12), the problem reduces to finding a self-consistent set of values for  $\phi^+(z)$ ,  $\phi^-(z)$  and  $\phi_p(z)$ . The solution was obtained by iterative numerical integration of equations (11) and (12). The results are summarized in Fig. 2 and Table II. The FORTRAN computer program which numerically integrated the equations, and which provided the plots in Fig. 2, is listed in the Thesis Appendix, along with typical input data.

## REFERENCES

1. C. V. Shank, R. L. Fork, R. F. Leheny and J. Shah, *Phys. Rev. Lett.* 42, 112 (1979).
2. A. Migus, J. L. Martin, R. Astier, and A. Orszag, in Picosecond Phenomena II, edited by R. M. Hochstrasser, W. Kaiser, and C. V. Shank, Springer Series in Chemical Physics, Vol. 14 (Springer-Verlag, New York, 1980), p.59.
3. A. Migus, C. V. Shank, E. P. Ippen, and R. L. Fork, *IEEE J. Quantum Electron.* QE-18m 101 (1982).
4. T. L. Koch, L. C. Chiu, and A. Yariv, *Optics Commun.* 40, 364 (1982).
5. T. L. Koch, L. C. Chiu, and A. Yariv, *J. Applied Physics* 53, 6047 (1982).
6. see, e. g. A. Yariv, Quantum Electronics, 2nd ed. (Wiley, New York, 1975), problem 12.1.
7. E. P. Ippen, C. V. Shank, and A. Bergman, *Chem. Phys. Lett.* 38, 611 (1976).
8. V. Sundström, T. Gillbro, and H. Bergström, *Chem. Phys.* 73, 439 (1982).
9. U. Ganiel, A. Hardy, G. Neumann, D. Treves, *IEEE J. Quantum Electron.* QE-11, 881 (1975).
10. G. Dujardin and P. Flamant, *Optica Acta* 25, 273 (1978).
11. B. J. Snavely, *Proc. IEEE* 57, 1374 (1969).
12. L. M. Frantz and J. S. Nodvik, *J. Appl. Phys.* 34, 2346 (1963).
13. R. Bellman, G. Birnbaum, and W. G. Wagner, *J. Appl. Phys.* 34, 780 (1963).
14. E. P. Ippen and C. V. Shank, in Ultrashort Light Pulses, edited by S. L. Shapiro, Topics in Applied Physics, Vol. 18 (Springer-Verlag, New York, 1977), p. 88.
15. M. Berg, Ph.D. Thesis, The University of California at Berkeley, Berkeley, Ca., 1985.

## Acknowledgements

Several people have contributed immensely to the work described in this thesis. By his enthusiasm for new research directions, Professor Charles Harris has made it possible to pursue both better models for condensed phase dynamics and better techniques to investigate those models. Mark Berg has worked together with me through several years of laboratory effort to develop the picosecond laser system and to apply it to the iodine reaction system. Mark has been a source of ideas, a sounding board in countless discussions, and a stabilizing influence at difficult times. Steven George brought me from the classroom to the laboratory in my first years at Berkeley, and introduced me to the intricacies of carrying out difficult experiments with short pulse lasers. Keenan Brown has been a continuous source of good ideas and a masterful experimentalist as a coworker. Keenan also set up the computerized data collection system used in the chemical dynamics experiments.

Members of the research group working with Charles Harris have provided a stimulating atmosphere for research, and have been good friends. Dor Ben-Amotz has been a particularly enthusiastic organizer of, and participant in, discussions and experiments. Paul Alivisatos and David Waldeck have helped to keep the work in perspective with good questions and intelligent, critical comments. Other members of the research group have supported me in many ways, and several are now enthusiastically pursuing some of the questions raised in this work. Mrs. Vijaya Narasimhan has provided organization and order for the group throughout my time at Berkeley.

I am grateful for assistance from a National Science Foundation Fellowship for Graduate Study during 1979-1982. This work was also supported in part by the National Science Foundation and the Director, Office of Energy Research, Office of Basic Energy Sciences, Chemical Sciences Division of the U. S. Department of Energy, under contract No. DE-AC03-76SF00098.

Thesis Appendix

## Program DYAMP6

DYAMP6 is a FORTRAN program written for use on the Digital Equipment Corporation RT-11 operating system to numerically integrate the equations for a longitudinally pumped amplifier dye cell under steady state pumping conditions (Eqs. 9-12, Ch. 4 Appendix). The program provides the ASE intensity in the forward and backward directions, and the fraction of the molecules in the excited state, all as a function of position along the cell axis. The integrated excited state population is also provided.

The parameters of the dye molecules, and initial estimates for the forward and backward ASE, and the pump intensity must be provided to the program through an input data file DYAM.DAT to be resident on system disk "DK:". The program sequentially improves the ASE and pump estimates by holding two arrays fixed and recalculating the third. This process is not necessarily convergent, and a new array is set equal to the weighted average of the original and recalculated arrays. The weighting parameter, "ADJUST", for the recalculated array must usually be set much less than one to provide a stable solution.

The graphics are written in PLOT10 format, and are found in the two subroutines PLOTA and PLOTB at the end of the main program. Both PACLIB and TCSLIB graphics libraries must be linked with the programs.

The parameters are as follows (see Appendix of Chapter 4).

PUMP	Array of pump intensity values along cell length ( $s^{-1}cm^{-3}$ )
PLUS	Array of forward ASE intensities
MINUS	Array of backward ASE intensities
PSIG	$\sigma_p$
ABSIG	$\sigma_a$
EMSIG	$\sigma_e$
ELAM	E
RATE	$1/\tau$
DENS	Dye molecule density ( $cm^{-3}$ )
RL	Cell length (cm)
RR	Cell radius (cm)
NUM	divisions of cell (~200)

A typical data input file DYAM.DAT is listed below. DYAMP6 is listed on the following pages.

TYPE DYE: DYAM.DAT

```

200*1.35E+23
20*0.0,40*1.0E+18,40*1.0E+20,40*1.0E+22,40*1.0E+24,20*1.0E+25
20*1.0E+25,40*1.0E+24,40*1.0E+22,40*1.0E+20,40*1.0E+18,20*0.0
2.4E-17,1.46E-18,1.9E-16,0.24,1.82E+08
3.0E+18,1.0,0.02,200

```

TYPE D70:DTAMP-.FOR

DYE AMPLIFIER CELL MODEL - DYAMP6 -

DYAMP6 CALCULATES ASE FLUX AND EXCITED STATE POPULATIONS UNDER STEADY STATE PUMPING CONDITIONS WITH NO SIGNAL INPUT.

DYAMP6 CALCULATES FLUX FOR A LONGITUDINALLY PUMPED DYE AMPLIFIER CELL. PUMP, PLUS, AND MINUS FLUXES ARE CALCULATED IN ORDER FOR SPECIFIED NUMBER OF ITERATIONS. PROGRAM DESIGNED TO AVOID PROBLEMS WITH PUMP AND MINUS ADJUSTMENTS BY USING 'ADJUST', A PARAMETER WHICH CONTROLS MAGNITUDE OF PUMP OR MINUS CHANGES ON EACH ITERATION. PLUS, MINUS, AND PUMP FLUXES MAY BE PLOTTED. N1 MAY BE CALCULATED AND PLOTTED. ~~SINCE LAST ITERATION OF THE GIVEN FLUX. PLUS~~

DATA INPUT IS THROUGH DATA FILE DYAM.DAT, WHICH MUST BE FOUND ON THE SYSTEM DISK DK:.. THE READ IS LIST FORMATTED; DATA MUST APPEAR IN FOLLOWING ORDER, LIST FORMATTED:

NUM PUMP INPUT VALUES, PUMP(1) FIRST

NUM PLUS INPUT VALUES, PLUS(1) FIRST

NOTE PLUS(1) MUST BE 0.0

NUM MINUS INPUT VALUES, MINUS(1) FIRST

NOTE MINUS(NUM) MUST BE 0.0

PSIG,ABSIG,EMSIG,ELAM,RATE

DENS,RL,RR,NUM

ANY PARAMETER OF THE CALCULATION MAY BE RESET AFTER THE CALCULATION IS COMPLETED; AND THE FLUX MAY THEN BE RECALCULATED. NUM, THE NUMBER OF DIVISIONS OF THE CELL, CANNOT BE RESET: THE DIMENSIONS OF ALL ARRAYS IN THE 'REAL' STATEMENT MUST BE CHANGED, AND NUM CHANGED IN THE DATA FILE DYAM.DAT.

SET PARAMETERS AND INITIAL ARRAYS

REAL PUMP(200),MINUS(200),PLUS(200),BPLUS(200),BMINUS(200),

1 PERCEN(200),X(200),Y(200),PUMPO(200),MINO(200)

INTEGER BRANCH,RESET

COMMON DELZ, RL

DATA X,Y/400\*0.0/

OPEN (UNIT=3,NAME='DX0:DYAM.DAT',TYPE='OLD',

1 READONLY,ACCESS='SEQUENTIAL',FORM='FORMATTED',ERR=17)

READ (3,\*,ERR=171) PUMP,PLUS,MINUS,

1 PSIG,ABSIG,EMSIG,ELAM,RATE,

2 DENS,RL,RR,NUM

CLOSE (UNIT=3)

```

C
C   TYPE DATA INPUT
C
1   TYPE 1003
1003 FORMAT (' RETURN 1 TO CHECK DATA INPUT, 2 TO CONTINUE' )
ACCEPT 111, BRANCH
111  FORMAT (I5)
GOTO (5,6) BRANCH
5   TYPE 1000
1000 FORMAT (' INPUT - FIRST AND LAST POINTS: PUMP,PLUS, AND
1 MINUS' )
TYPE 1050,PUMP(1),PUMP(NUM),PLUS(1),PLUS(NUM),MINUS(1),
1 MINUS(NUM)
1050 FORMAT (' ',2E11.3)
TYPE 1001
1001 FORMAT (' PSIG,ABSIG,EMSIG,ELAM,RATE ' )
TYPE 1051, PSIG,ABSIG,EMSIG,ELAM,RATE
1051 FORMAT (' ',5E11.3)
TYPE 1002
1002 FORMAT (' DENS,RL,RR,NUM ' )
TYPE 1052, DENS,RL,RR,NUM
1052 FORMAT (' ',E11.3,2F8.3,I5)
TYPE 1004
1004 FORMAT (' ENTER 1 TO CHANGE INPUT, 2 TO CONTINUE ' )
ACCEPT 111, BRANCH
GOTO (90,6) BRANCH

C
C   SET DELZ
C
6   RNUM = NUM
DELZ = RL/RNUM
ITERAT = 0
INDEX = 0

C
C   CALCULATE GEOMETRIC FACTOR ARRAYS FOR PLUS AND MINUS ASE
C
DO 2 N=1,NUM
RN = N
Z = (RN-0.5)*DELZ
GPLUS = 0.5*(1.0 - (RL - Z)/((RL - Z)**2 + RR**2)**0.5)
BPLUS(N) = RATE*GPLUS*ELAM
BMINUS(NUM+1-N) = BPLUS(N)
CONTINUE

2
C
C   ENTER ADJUST PARAMETER
C
7   TYPE 1007
1007 FORMAT (' ENTER ADJUST, FORMAT X.XXXX ' )
ACCEPT 1057, ADJUST
1057 FORMAT (F6.4)

```



```

C
C TEST ITERATIONS, TYPE 6 PLUS POINTS IF FINISHED
C
IF (INDEX .LT. ITERAT) GOTO 30
TYPE 200, INDEX
200 FORMAT (' PLUS FLUX, 6 POINTS, ',I6,' ITERATIONS ')
TYPE 250, PLUS(1),(PLUS(N),N=40,200,40)
250 FORMAT (' ',6E11.3)
C
C CALCULATE NEW MINUS ASE FLUX
C
30 DO 35 N=NUM,2,-1
MINO(N-1) = MINUS(N-1)
ASE = PLUS(N) + MINUS(N)
STORE1 = PSIG*PUMP(N) + ABSIG*ASE
STORE2 = RATE + EMSIG*ASE
1 STORE2/ STORE1) - ABSIG*MINUS(N)/(1.0 + STORE1/STORE2))
MINUS(N-1) = MINUS(N) + DMINUS
IF(MINUS(N-1) .LT. 0.0) MINUS(N-1) = 0.0
35 CONTINUE
DO 36 N=1,NUM-1
MINUS(N) = MINO(N) + ADJUST*(MINUS(N) - MINO(N))
36 CONTINUE
C
C TEST ITERATIONS, TYPE 6 MINUS POINTS IF FINISHED,
C GO TO 10 (OR 9 IF FINISHED)
C
IF (INDEX .LT. ITERAT) GOTO 10
TYPE 300, INDEX
300 FORMAT (' MINUS FLUX, 6 POINTS, ',I6,' ITERATIONS ')
TYPE 350, MINUS(1),(MINUS(N),N=40,200,40)
350 FORMAT (' ',6E11.3)
GOTO 9
C
C CHOOSE NEXT OPERATION
C
99 PAUSE 'RETURN TO CHOOSE NEXT OPERATION'
TYPE 990
990 FORMAT (' ENTER: '//
1 ' 1: TO CARRY OUT MORE ITERATIONS '//
2 ' 2: TYPE FULL PLUS AND MINUS ARRAYS '//
3 ' 3: PLOT PLUS ASE '//
4 ' 4: PLOT MINUS ASE '//
5 ' 5: PLOT PUMP '//
6 ' 6: CALCULATE AND PLOT N1 '//
7 ' 7: RESET PARAMETERS AND RECALCULATE '//
8 ' 8: STOP ')
ACCEPT 111, BRANCH
GOTO (9,60,70,80,85,40,90,999) BRANCH
TYPE 991, BRANCH
991 FORMAT (' BRANCHING ERROR, ',I6,' IS NOT A CHOICE ')
GOTO 99

```

```

C
C
C
40  CALCULATE PERCENT N1
    TOTN1 = 0.0
    DELN = DENS*DELZ*3.1415*RR**2
    DO 45 N=1,NUM
      ASE = PLUS(N) + MINUS(N)
      STORE1 = PSIG*PUMP(N) + ABSIG*ASE
      STORE2 = RATE + EMSIG*ASE
      PERCEN(N) = 100.0/(1.0 + STORE2/STORE1)
      TOTN1 = TOTN1 + PERCEN(N)*DELN*0.01
45  CONTINUE
C
C
C    TYPE OUT PERCENT N1 AND TOTAL EXCITED MOLECULES
    TYPE 400,TOTN1
    FORMAT (' TOTAL EXCITATION NUMBER = ',E11.4)
    TYPE 450, PERCEN
    FORMAT (' ',10F7.2)
C
C    SET PARAMETERS AND ARRAYS FOR PLOT N1...CALL PLOT ROUTINE
C
    TYPE 401
    FORMAT (' ENTER 1 TO PLOT N1, 2 TO RETURN ')
    ACCEPT 111, BRANCH
    GOTO (50,99) BRANCH
50  I1 = -1.0
    I2 = 2.0
    CALL PLOTB (NUM,PERCEN,X,Y,I1,I2)
    GOTO 99
C
C
C    TYPE ASE ARRAYS
60  PAUSE 'RETURN FOR PLUS FLUX '
    TYPE 600, PLUS
    FORMAT (' ',7E10.3)
600 PAUSE ' RETURN FOR MINUS FLUX'
    TYPE 600, MINUS
    GOTO 99
C
C
C    PLOT PLUS ASE
70  I1 = INT(ALOG10(PLUS(2)))
    I2 = INT(ALOG10(PLUS(NUM))) + 1
    CALL PLOTB (NUM,PLUS,X,Y,I1,I2)
    GOTO 99
C
C
C    PLOT MINUS ASE
80  I1 = INT(ALOG10(MINUS(NUM-1)))
    I2 = INT(ALOG10(MINUS(1))) + 1
    CALL PLOTB (NUM,MINUS,X,Y,I1,I2)
    GOTO 99

```

```

C
C      PLOT PUMP
C
85      DO 86 N=2,NUM
        IF (PUMP(N) .LT. 1.0E+12) PUMP(N) = PUMP(N-1)
86      CONTINUE
        I1 = INT(ALOG10(PUMP(NUM)))
        I2 = INT(ALOG10(PUMP(1))) + 1
        CALL PLOTB (NUM,PUMP,X,Y,I1,I2)
        GOTO 99

C
C      RESET PARAMETERS AND RECALCULATE FLUX
C
90      TYPE 900,PUMP(1),DENS,RL,RR,PSIG,ABSIG,EMSIG,ELAM,RATE
900     FORMAT (' PRESENT PARAMETER VALUES ARE: '//
1       ' PUMP: ',E11.3//' DENS: ',E11.3//' RL, RR: ',2F6.3/
2       ' PSIG,ABSIG,EMSIG,ELAM,RATE: ',5E11.3//
3       ' ENTER: '// 1: TO CHANGE PUMP INTENSITY '//
4       ' 2: TO CHANGE DYE CONCENTRATION, DENS '//
5       ' 3: TO CHANGE CELL DIMENSIONS RL,RR '//
6       ' 4: TO CHANGE DYE PARAMETERS '//
7       ' 5: TO BEGIN CALCULATION OF FLUX INTENSITIES ')
        ACCEPT 111, BRANCH
        GOTO (91,92,93,94,1) BRANCH
        TYPE 909, BRANCH
909     FORMAT (' BRANCHING ERROR, ',I6,' IS NOT A CHOICE ')
        GOTO 90
91      TYPE 901
901     FORMAT (' ENTER NEW PUMP FLUX, FORMAT X.XXXE+XX ')
        ACCEPT 951, PUMP(1)
951     FORMAT (E10.3)
        DO 95 N=2,NUM
          PUMP(N) = PUMP(1)
95      CONTINUE
        GOTO 90
92      TYPE 902
902     FORMAT (' ENTER NEW DENS VALUE, FORMAT X.XXXE+XX ')
        ACCEPT 951, DENS
        GOTO 90
93      TYPE 903
903     FORMAT (' ENTER NEW RL, RR VLUES, FORMAT 2XX.XXX ')
        ACCEPT 953, RL,RR
953     FORMAT (2F6.3)
        GOTO 90
94      TYPE 904
904     FORMAT (' ENTER NEW PSIG,ABSIG,EMSIG,ELAM,RATE, '//
1       ' FORMAT 5XX.XXXE+XX ')
        ACCEPT 954, PSIG,ABSIG,EMSIG,ELAM,RATE
954     FORMAT (5E10.3)
        GOTO 90
999     STOP 'PROGRAM RUN COMPLETED'
17      STOP 'ERROR IN OPEN INPUT FILE'
171     STOP 'ERROR IN READ INPUT FILE'
        END

```

C  
C  
C

SUBROUTINE PLOTA - CALLS PACLIB AND TCSLIB ROUTINES

999

```

SUBROUTINE PLOTA(IPNTS,X,Y,XMIN,XMAX,YMIN,YMAX,N1,N2)
LOGICAL*1 FARRAY(20),GARRAY(20)
DIMENSION X(IPNTS),Y(IPNTS)
CALL SCOPY ('(F6.3)',FARRAY)
CALL SCOPY ('(F6.3)',GARRAY)
CALL INITT (480)
CALL PREP (6,6)
CALL NEWPAG
CALL DWINDO (XMIN,XMAX,YMIN,YMAX)
CALL GRAPH (IPNTS,X,Y,-1,0)
CALL HOME
PAUSE
CALL HICK (N1,N2,FARRAY,GARRAY,6,6)
CALL HOME
PAUSE
CALL HARD (IHARD)
IF (IHARD .EQ. 0) GOTO 999
RETURN
END

```

C  
C  
C  
C  
C

```

SUBROUTINE PLOTB - CALLED FROM MAIN DYAMP PROGRAM
DOES NOT CALL PACLIB OR TCSLIB; SETS PARAMETERS
FOR CALL TO PLOTA

```

5

```

SUBROUTINE PLOTB (IPNTS,SOURCE,X,Y,I1,I2)
COMMON DELZ,RL
DIMENSION X(IPNTS),Y(IPNTS),SOURCE(IPNTS)
DO 5 N=2,IPNTS-1
  RN = N
  X(N) = (RN - 0.5)*DELZ
  Y(N) = ALOG10(SOURCE(N))
CONTINUE
X(1) = 0.5*DELZ
X(IPNTS) = RL - X(1)
Y(1) = Y(2)
Y(IPNTS) = Y(IPNTS - 1)
XMIN = 0.0
XMAX = RL
YMIN = I1
YMAX = I2
N1 = I1
N2 = I2 - I1 + 1
CALL PLOTA(IPNTS,X,Y,XMIN,XMAX,YMIN,YMAX,N1,N2)
RETURN
END

```

This report was done with support from the Department of Energy. Any conclusions or opinions expressed in this report represent solely those of the author(s) and not necessarily those of The Regents of the University of California, the Lawrence Berkeley Laboratory or the Department of Energy.

Reference to a company or product name does not imply approval or recommendation of the product by the University of California or the U.S. Department of Energy to the exclusion of others that may be suitable.

*LAWRENCE BERKELEY LABORATORY  
TECHNICAL INFORMATION DEPARTMENT  
UNIVERSITY OF CALIFORNIA  
BERKELEY, CALIFORNIA 94720*